Fall 11-15-2018

Vertical Transport Study of III-V Type-II Superlattices

Zahra Taghipour
Center for High Technology Materials

Recommended Citation

Taghipour, Zahra. "Vertical Transport Study of III-V Type-II Superlattices." (2018). https://digitalrepository.unm.edu/ose_etds/64

Candidate

Department

This dissertation is approved, and it is acceptable in quality and form for publication:

Approved by the Dissertation Committee:

, Chairperson

Vertical Transport Study of III-V Type-II Superlattices

by

Zahra Taghipour

B.S., Physics, Azad University Central Tehran Branch, Iran 2008
M.S., Photonics, Shahid Beheshti University, Iran 2012
M.S., Optical Science and Engineering, University of New Mexico, 2014

DISSERTATION

Submitted in Partial Fulfillment of the
Requirements for the Degree of

Doctor of Philosophy
Optical Science and Engineering

The University of New Mexico

Albuquerque, New Mexico

December, 2018

Dedication

To my husband for his support and encouragement throughout this work

Acknowledgments

Firstly, I would like to express my gratitude to my advisor Prof. Krishna for the continuous support and motivation in my Ph.D. study and related research. My sincere thanks also go to my second advisor, Dr. Balakrishnan, who provided me with an opportunity to join his team. Without his precious support, it would not be possible to conduct this research.

I would like to thank my dissertation committee: Dr. Steenbergen, Dr. Prasankumar, and Dr. Hecht, for their time and help. Also, I'd also like to appreciate my fruitful discussion with Dr. Aifer, Dr. Maximenko, and Dr. Steenbergen, which helped widen my research from various perspectives.

I have several other people I would like to thank; my group members from past and present at UNM whom I enjoyed working with: Elena, Brianna, Ted, Stephen, Marzieh, Alireza, Vinita, Ahmad, Happy, Emma, and Lilian; my fellows at Center for High Technology Materials and Physics and Astronomy Department; and the staff and faculty who helped me on my projects anytime I reached out to them, especially Dr. Diels, Dr. Hasselback, Dr. Sheik-Bahae.

Also, I would like to thank my parents for supporting me spiritually throughout this work and my life in general.

Last but not least, I'd like to thank my husband who has always been there for me whenever I needed him.

Vertical Transport Study of III-V Type-II Superlattices

by

Zahra Taghipour

B.S., Physics, Azad University Central Tehran Branch, Iran 2008

M.S., Photonics, Shahid Beheshti University, Iran 2012

M.S., Optical Science and Engineering, University of New Mexico, 2014

Ph.D., Optical Science and Engineering, University of New Mexico, 2018

Abstract

Type-II strained layer superlattice (T2SL) semiconductors hold great promise for mid- and long-wavelength infrared photodetectors. While T2SL-based materials have advanced significantly in the last three decades, an outstanding challenge to improve the T2SLs is to understand the carrier transport and its limitations, in particular along the superlattice growth layers.

In this dissertation, an overview of the current state-of-the-art InAs/GaSb T2SLs is presented. Fundamental semiconductor device equations and transport properties, including miniband conduction and the drift-diffusion parameters, are reviewed, and the fundamental limiting factors in carrier's transport are discussed. Furthermore, the standard method of electron-beam-induced current technique to measuring these parameters is described.

The bulk of the manuscript will then explore the characterization of transport properties in an InAs/GaSb nBp photodetector through a variety of techniques. Through electron-beam-induced-current ($EBIC$) measurements, the minority carrier diffusion length along the growth direction has been measured. The $EBIC$ analysis combined with lifetime measurements using time-resolved microwave reflectance method is then used to calculate the minority electron mobility along the growth direction. Quantum efficiency modeling technique is used as an alternative approach to studying transport and quantify the complex relationships between the device performance and the underlying physics involved in it. Photocurrent-voltage measurement is also used to qualitatively investigate the drift characteristics, such as the field dependence of the drift mobility and drift velocity. Finally, the result of a recent study on the electronic band structure of a series of narrow-band superlattices is summarized.

Contents

List of Figures **xi**

List of Tables **xvii**

Glossary **xix**

1 Introduction **1**

1.1 Semiconductor Superlattices 3

1.2 Type-II Superlattices 6

1.3 Detector Architectures based on T2SLs 8

1.3.1 Single uni-polar barrier 8

1.4 Vertical Transport 10

1.4.1 Isotropic vs. Anisotropic Systems 10

1.5 Significance of the Present Work 15

1.5.1 Thesis Objective 16

1.6 Outline of the Thesis 18

2 Nonequilibrium Charge Carrier Dynamics 19

2.1 Carrier Transport Equations 22

2.1.1 Carrier Transport Properties 24

2.1.2 Miniband Conduction 26

2.2 Charge Carrier Lifetime 29

2.3 Current-Voltage Characteristics 34

2.4 Quantum Efficiency Modeling 38

2.5 Chapter Summary 43

3 Electron Beam-Induced Current Technique 44

3.1 Basic Principles 45

3.2 Theoretical Model 46

3.2.1 Bonard Model 47

3.2.2 Luke Model 52

3.3 Experimental Considerations 54

3.4 Chapter Summary 57

4 Vertical Transport Study 58

4.1 Sample and Method 59

4.2 Carrier Lifetime Measurement 61

4.3 Diffusion Characterization 69

4.3.1 EBIC 69
4.3.1.1 Experimental Results and Discussion 76
4.3.2 QE Modeling 79
4.3.2.1 Absorption Coefficient Measurement 80
4.3.2.2 Experimental Results and Discussion 81
4.4 Drift Characterization 85
4.4.1 Photocurrent-Voltage Measurement 85
4.5 Chapter Summary 92

5 Many-body Perturbation Theory Study of Superlattices 94

5.1 Theory 95
5.2 Problem Statement 96
5.2.1 Density-Functional Theory 98
5.2.2 The Kohn-Sham equations 99
5.2.3 Many-Body Perturbation Theory 101
5.3 Computational Details 103
5.4 Results and discussion 106
5.5 Chapter Summary 113

6 Conclusion and Future Work 115

6.1 Conclusions 115

- 6.1.1 Summary of Results- Vertical Transport in MWIR InAs/GaS T2SLs 116
- 6.1.2 Summary of Results- Electronic Structure Characterization . . 120

6.2 Future Efforts 121

6.3 Concluding Remarks 122

List of Figures

1.1 The evolution of infrared detectors through four stages are depicted: first generation (scanning systems), second generation (staring systems, electronically scanned), third generation (staring systems with large numbers of pixels and two-color functionality), and fourth generation (staring systems with a very large number of pixels, multicolor functionality and other on-chip functions). (Adapted from [1]) 2

1.2 Three different superlattice band line-ups. 5

1.3 Energy band alignment in 6.1°A material system. 7

1.4 Comparison of the experimental dark current density of T2SL MWIR detectors at (a) 80 and (b) 150 K. The Rule07, MCT dark current density is shown with solid black lines (Adopted form [12]). 8

1.5 Schematic of barrier structures: (a) *nBn*, (b) *pBn*, and (c) *nBp*. . . 9

1.6 Schematic of superlattice cross-section; Z axis denotes the growth-axis or vertical direction, X-Y plane denotes the in-plane or horizontal direction. The superlattice is formed by alternating layers of wide and narrow band gap materials (A and B) grown along the Z axis. The effective potential experienced by electrons is shown on the right. 12

1.7 Summarizes the factors limiting vertical transport in type-II superlattices. 13

2.1 Potential and subband energy diagrams of superlattices. 27

2.2 Carrier recombination mechanisms in semiconductors E_t is the 'trap' energy level within the band gap caused by the presence of a foreign atom or a structural defect. 30

2.3 Schematic of a *pn* junction (top), and corresponding energy-band diagram (bottom) showing the carriers diffusion and drift in the quasi-neutral *p*- and *n*- regions toward the depletion region, where they are swept across by the electric field. 40

3.1 Schematic of the experimental set-up for *EBIC* characterization. (top) normal-collector geometry (bottom) planar-collector geometry. 46

3.2 Monte carlo simulation of the sulerlattice absorber under illumination of a beam with 20 keV energy, 50 nm beam diameter, 1×10^6 electrons, and a grid of $100 \times 100 \times 100$, (left) projected on XY plane, (right) projected on XZ plane. 51

3.3 Simulated EBIC profiles based on Bonard approach for the collection efficiency: (left) with varying diffusion length L. The beam energy is set to $E_b = 5$ keV and the S/D ratio to $10^5 cm^{-1}$, (right) with varying S/D. The beam energy is set to $E_b = 5$ keV and the bulk diffusion length to $L = 1 \mu m$. 53

3.4 Schematic of the *EBIC* setup with external electrical connections to the current amplifier. 55

4.1 (Top) The *nBp* InAs/GaSb T2SL photodetector showing the relative thickness of the constituent layers (not drawn in scale). (Bottom) Band alignment of the structure calculated using NRL MULTIBAND® [73] 60

4.2 Time-resolved microwave reflectance measurement setup including the microwave apparatus, the excitation laser, and the cryostat. . . . 62

4.3 Time-resolved microwave reflectance decays of carrier recombination in the MWIR InAs/GaSb T2SL absorber. Data are shown for multiple different initial optically generated carrier densities and sample temperatures. The arrows in the two plots highlight the second decay observed for temperatures of 20 to 150K. The inset to the 20 K plot shows the fast initial decays which occur during the first few tens of nanoseconds at three excess carrier densities. 63

4.4 Measured photoluminescence spectra of the T2SL absorber, and the peak PL energy (inset-black circles) as a function of temperature. Dashed line shows the Varshni fit with parameters α=0.24 meV/K, and β=270 K. 64

4.5 Measured minority carrier lifetime as a function of excess carrier density for a representative subset of temperatures, along with the calculated SRH, radiative, and Auger lifetime components. The total lifetime, shown as the solid purple curve, is the best fit for the measured lifetime to extract different fitting parameters. The radiative lifetime component at 260 K has a negligible effect on the total lifetime and is not shown. 66

4.6 Temperature-dependent measured minority carrier lifetimes (black circles), compared to the low injection level SRH, radiative, and Auger lifetime components. The solid purple curve is the best fit for the total lifetime to extract different fitting parameters. The radiative lifetime was calculated using a photon recycling factor Φ of 1.8. 68

4.7 (Top) The structure of InAs/GaSb *nBp* T2SL and the generated electron-hole volume in the absorber region due to the *e*-beam impingement on the sample, (Bottom) The SEM and *EBIC* images of the cross-section of the device under test at *e*-beam energy of 20 KeV and T=80K. 70

4.8 Experimental *EBIC* data are shown for three representative temperatures of 80, 120 and 150 K with (top) varying beam current denoted as the percentage of the total filament current in the SEM, and (bottom) varying beam energy in keV. *EBIC* intensities are normalized by signal peak maximum at the highest current(top) and accelerating voltage(bottom). 72

4.9 Extracted minority carrier diffusion lengths (L_e) for InAs/GaSb *nBp* MWIR sample as a function of temperature. The minority carrier diffusion lengths are extracted from the *EBIC* line scan profiles for *e*-beam energies of 10, 15, and 20 keV. 76

4.10 Vertical electron mobility for InAs/GaSb *nBp* MWIR sample as a function of temperature for *e*-beam energies of 10, 15, and 20 keV. Dashed lines show the acoustic phonon scattering μ_{AS}, and the ionized scattering μ_{IS} dependence on the temperature. 77

4.11 Absorption coefficient measured for the absorber layer w.r.t to the substrate under different operating temperatures. 82

4.12 Comparison between experimental and calculated quantum efficiency spectra for the *nBp* photodetector at V=0.2V, for T=80, 120, and 150 K. The devices used for this measurement was 500 μm in size. The CO_2 absorption at 0.295 eV is visible in the experimental data. 83

4.13 Schematic of the structure used for the photocurrent-voltage measurement. 86

4.14 Schematic of the current-voltage measurement setup. 87

4.15 Peak photocurrent versus applied bias for various operating temperatures. 88

4.16 Peak photocurrent versus applied bias for various pump power. . . 89

4.17 Transient photocurrent as a function of bias and time at 77 K. . . . 89

4.18 Modeled drift velocity for a 10 ML InAs / 10 ML GaSb sample with a period of 60 A for varying (left) miniband width and assuming $\tau = 40ps$, and (right) scattering time and assuming the miniband width is 1 meV. 92

5.1 (a) Unit cell of T2SL comprises of n monolayers of InAs and m monolayers of GaSb (Shown for special case of (2,2)). Depending on the thickness of the InAs layer, a portion of strain-compensating layer of InSb is introduced in the unit cell, denoted as interfacial (IF) layer, (b) Type-II band alignment between InAs and GaSb. *Experimental band gap in eV is shown for each of InAs and GaSb. [117] 105

5.2 Comparison of the simulated zone center band gaps of (4,7), (6,7), (8,8), (10,8), and (10,10) superlattices within LDA, G_0W_0+LDA, and GW_0+LDA approximations, with experiment[112, 113, 114, 115]. The simulations have been performed using the experimental LC of the GaSb (11.52 Bohr). Absorption data was used as the first choice, and the photoluminescence (PL) results along with Varshni relation to extrapolate 0 K gaps from the experimental data. 108

5.3 The DFT+G_0W_0 band structure of (4,7), (6,7), and (10,10) superlattices at 0K, calculated with LC=11.52 Bohr. The highest valence band is set to be zero. Arrows indicate the highest occupied levels. The inset shows the Γ-to-L direction for (10,10), in which the lowest unoccupied level happens at $L = (0.5, 0.5, 0)\frac{2\pi}{a}$. 109

5.4 The DFT+G_0W_0 band structure of (8,8) superlattice at 0K, with and without IF layer, calculated with experimental LC (=11.52 Bohr). The highest valence band is set to be zero. (a/c) denotes the ratio of in-plane lattice constant over the dimension of the supercell along the growth direction. 112

List of Tables

1.1 The comparison between main advantages and disadvantages of three main infrared architectures: GaAs/AlGaAs quantum well infrared photodetectors (QWIP), mercury cadmium telluride (HgCdTe) detector, and Type-II superlattices [7, 5]. 4

1.2 A summary of the results of various minority carriers transport parameters in III-V type-II superlattices, measured with different approaches. Here, InAs/GaSb superlattices are referred to as 'Ga-containing T2SLs', and InAs/InAsSb superlattices are referred to as 'Ga-free T2SLs'. 16

2.1 List of assumptions made in the derivation of the hovel model. . . . 39

3.1 Summary of the models proposed for *EBIC*. 47

4.1 Extracted fit parameters for calculating the total minority carrier lifetime. 67

4.2 A summary of different extracted transport properties from the analytical QE model for $V_{applied} = 0.2$ V 84

5.1 Simulated and experimental band gaps in eV for the bulk materials, i.e. InAs and GaSb. The results are for experimental lattice constants of 11.52 Bohr and 11.44 Bohr for GaSb and InAs, respectively. Experimental and simulated results are for 0K. 107

5.2 Summary of the simulated band gaps in eV for (8,8) and (10,10) superlattices. The structures were relaxed along the growth directions while the in-plane lattice constants were set to be equal to that of the GaSb substrate. The theoretical LC was obtained through relaxing the GaSb bulk structure in the LDA. 110

Glossary

T2SL	Type-II superlattices
EBIC	Electron-beam-induce current
SEM	Scanning Electron Microscope
QE	Quantum Efficiency
MC	Minority Carrier
EB	Electron barrier
HB	Hole barrier
MCT	Mercury Cadmium Telluride
SRH	Shockley-Read-Hall

Chapter 1

Introduction

The demanding applications of Infrared (IR) technology in a variety of fields such as military, aeronautical/aerospace research, healthcare systems, and surveillance require increasingly sensitive photodetectors and optical emitters with greater output power. The result of this demand has been significant improvements in IR technology over the past few decades; thermocouples, bolometers, pyroelectric detectors, intrinsic and extrinsic photodetectors, and low dimensional solids such as quantum wells and quantum dot detectors, and superlattices are just a few examples of this transition in IR technology. Figure 1.1 presents the evolution of significant development for IR photodetectors, including four stages: first generation (scanning systems), second generation (staring systems-electronically scanned), third generation (staring systems with large numbers of pixels and two-color functionality), and fourth generation (staring systems with a very large number of pixels, multi-color functionality and other on-chip functions, e.g. better radiation/pixel coupling, avalanche multiplication in pixels, polarization/phase sensitivity)[1].

At present, Mercury Cadmium Telluride (HgCdTe) is at the forefront of infrared imaging, along with the GaAs/AlGaAs based Quantum Well Infrared Photodetectors

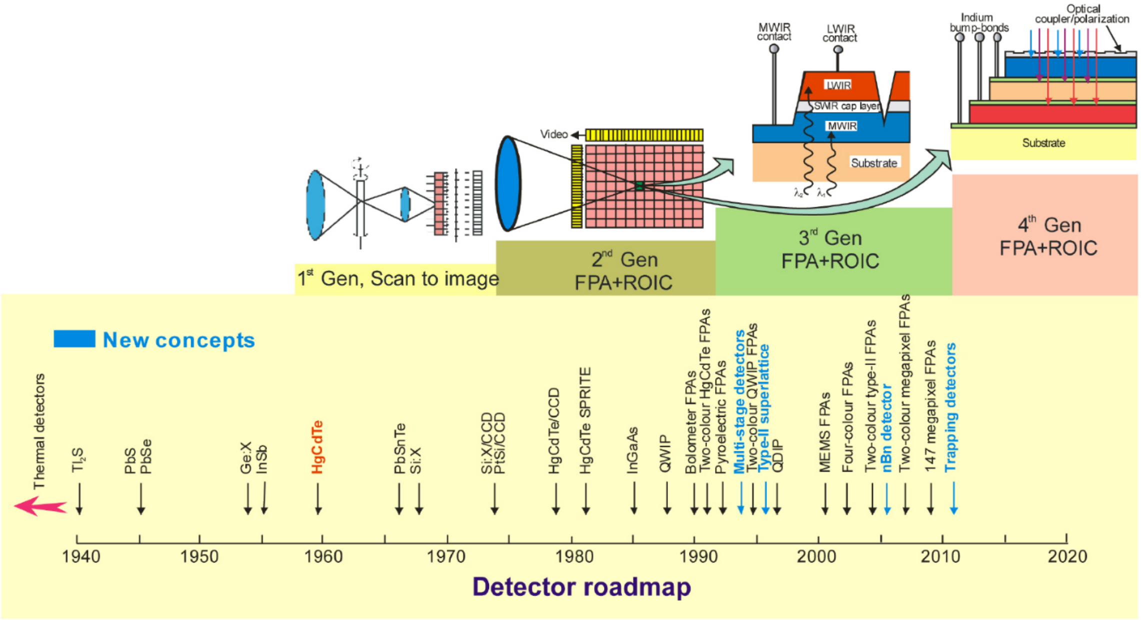

Figure 1.1: The evolution of infrared detectors through four stages are depicted: first generation (scanning systems), second generation (staring systems, electronically scanned), third generation (staring systems with large numbers of pixels and two-color functionality), and fourth generation (staring systems with a very large number of pixels, multi-color functionality and other on-chip functions). (Adapted from [1])

(QWIPs)[2]. Both of which offer wavelength tunability and multicolor capabilities. The main motivations to replace HgCdTe are technological problems of this material. One of them is a weak Hg-Te bond, which results in bulk, surface and interface instabilities. Uniformity and yield are still issues, especially in the very long wavelength IR (VLWIR) spectral range[3]. The difficulties in growing HgCdTe material and the requirement of extremely precise composition control to accurately determine the band gap encouraged the development of alternative technologies over the past sixty years[4]. With respect to HgCdTe detectors, GaAs/AlGaAs quantum well devices have a number of potential advantages, including the use of standard manufacturing techniques based on mature GaAs growth and processing technologies, highly uniform and well-controlled MBE (molecular beam epitaxy) growth on greater than six inches GaAs wafers, high yield and thus low cost, more thermal stability, and extrinsic radiation hardness[5]. However, QWIP detectors are extrinsic devices in which the dopant concentrations are limited by the epitaxial growth processes. As a result, the optical cross-sections for absorption are limited. In addition, the inter-subband lifetimes in QWIPs detectors are inherently short (about 10^{-11} s) which results in low quantum efficiency and relatively poor performance at temperatures 50 K. At these higher temperatures, thermally stimulated carriers dominate optically produced carriers, resulting in a low signal-to-noise ratio[6]. These shortcomings have opened up the field to explore new technologies like superlattice material systems. Type-II superlattices (T2SLs), based on III-V semiconductors, have emerged as a strong competitor of HgCdTe ternary alloys, and are relatively new alternative IR material systems and have great potential for LWIR/VLWIR spectral ranges with performance comparable to HgCdTe with the same cutoff wavelength. T2SL detectors utilize mature growth and fabrication technologies and favorable spatial uniformity over large areas. Table 1.1 compares above mentioned materials for the application of IR photodetectors.

In this chapter, the general overview of type-II superlattices (T2SLs) with a brief summary of different architectures for the application of infrared imaging technology is presented. Furthermore, physical properties of interest along with a brief review of previous studies are described. Lastly, the outline of the research of this dissertation and its significance for the development of the IR technology based on T2SLs is presented.

1.1 Semiconductor Superlattices

The introduction of the semiconductor superlattice by L. Esaki and R. Tsu at the IBM research laboratories In the 1970s[8] opened a new chapter in the physics of

Table 1.1: The comparison between main advantages and disadvantages of three main infrared architectures: GaAs/AlGaAs quantum well infrared photodetectors (QWIP), mercury cadmium telluride (HgCdTe) detector, and Type-II superlattices [7, 5].

	GaAs/AlGaAs QWIP	**HgCdTe**	**Type-II Superlattices**
Pros	• Mature GaAs growth	• Low Dark Current	• Mature Sb-based growth
	• High yield and thus low cost	• High Spectral Detectivity	• Improved yield
	• High thermal stability	• High QE	• Better uniformity
	• Fast response time	• Low NEDT and NEI (for FPAs)	• Higher stability
	• High material quality at low temperatures	• Well developed theory and technology	• Reduced tunneling current due to large effective electron mass
Cons	• Fundamental limitations associated with intersubband transitions	• Low yield (for large FPAs)	• Low minority lifetime
	• Low optical conversion efficiency	• Low uniformity	• Low absorption coefficient
	• High dark current	• Surface and interface instability	• High dark current
		• Large tunneling currents due to low electron effective mass	• Passivation challenges
		• Difficulties in growing HgCdTe material	

semiconductors. Upon their original proposal and pioneering experiments, a wide spectrum of experimental and theoretical investigations on superlattices and quantum wells over the last two decades have been started. A variety of engineered structures now exhibit extraordinary transport and optical properties which do not exist in any natural crystal. This new degree of freedom offered in semiconductor research through advanced materials engineering has inspired many experiments, resulting in observations of not only predicted effects but also totally unknown phenomena [9].

Manufacturing of these artificial superlattices by means of epitaxial growth of heterostructures has opened up a new field of research, which is still advancing. Innovations and improvements in epitaxial techniques such as MBE and MOCVD (metalorganic chemical vapor deposition) have made it possible to prepare high-quality heterostructures with predesigned potential profiles and impurity distributions having dimensional control close to interatomic spacing[10]. The epitaxial growth of a superlattice consists of the interchangeable deposition of two types of atoms, which continue the crystal structure of a substrate and form the heterostructure. The substrate is chosen with the appropriate crystal symmetry and a close lattice constant to that of the growing layer. The relative positions of the energy gaps of the two materials constitute the band offset of the superlattice. It is customary to classify these structures according to the confinement energy schemes of their electrons and holes. Figure 1.2 shows the three possible types of heterostructures with respect to the band offset. In type-I superlattices, the electrons and holes are both confined within the same layers (forming the well). One example of type-I superlattices is GaAs/AlGaAs heterostructure, in which the conduction band edge in GaAs lies at a lower energy than the conduction band edge in AlGaAs and the valence band edge in GaAs lies at a higher energy than the valence band edge in AlGaAs. Thus the GaAs acts as a quantum well and the AlGaAs as a potential barrier both for electrons and for holes[11]. Type-II staggered superlattices can be called ‘spatially indirect band

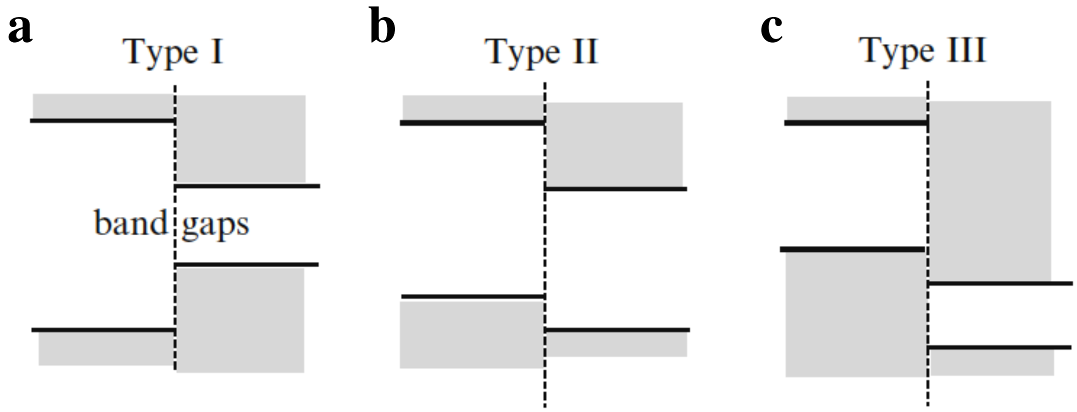

Figure 1.2: Three different superlattice band line-ups.

gap' semiconductor: While the electrons are confined in one layer, the holes are confined in a different layer. Superlattices comprised of InAs/AlSb are examples of this type. On the other hand, type-II broken gap (also known as type-III) superlattices behaves like zero-gap or small-gap semiconductors since there is either only a very small energy gap between the electrons in one layer and the holes in another layer or none at all, like InAs/GaSb superlattices. Designs utilizing the latter material are still in development and are the concern of many studies including this dissertation.

1.2 Type-II Superlattices

A special class of superlattices is known as the group 6.1°A materials with type-II band alignment. The band gap and band-offset can be tailored in type-II superlattices to design the heterostructure for mid-wave infrared (MWIR) and long-wave infrared (LWIR) applications. InAs/Ga(In)Sb superlattices, InAs/AlSb superlattices, GaSb/AlSb superlattices or any combination of these compounds are examples of this class.

As shown in Fig. 1.3, in InAs/AlSb superlattices, the conduction band of InAs is slightly above the valence band of AlSb, which is known as staggered band alignment, and in InAs/GaSb superlattices, the conduction band of InAs is lower than the valence band of GaSb, which is known as broken-gap alignment. Figure 1.3 also shows that there is a type-I nested alignment between GaSb and AlSb. Furthermore, InSb with a lattice constant of 6.479°A is included since it is usually used in the growth process for the strain compensation and the interface control. Among these, InAs/GaSb T2SLs based detectors have been investigated as an attractive technology for realizing IR sensors operating at higher temperatures[4]. In this system, the effective band gap can be adjusted by varying the thickness of constituent layers; the tunneling current is lower because of larger effective masses of electron and

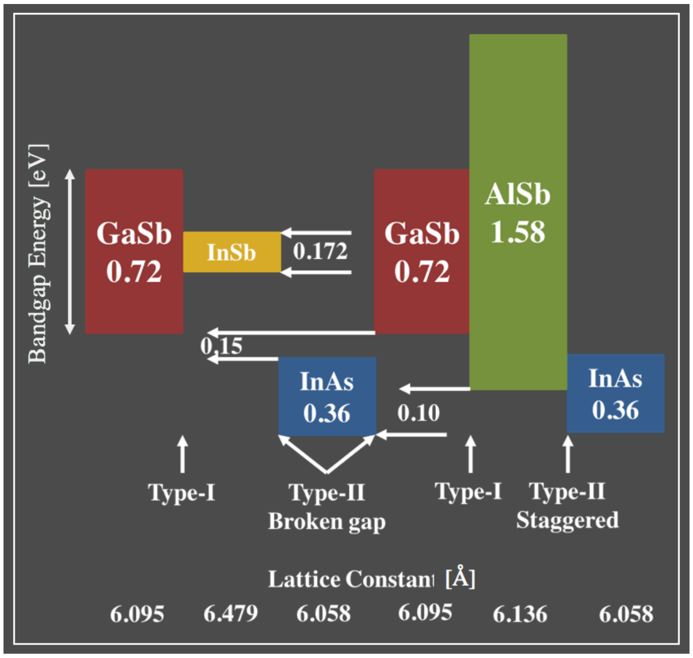

Figure 1.3: Energy band alignment in 6.1°A material system.

holes; and the strain reduces the Auger recombination rate due to the splitting of the heavy-hole (HH) and light-hole (LH) bands and the larger electron effective mass[7]. All these properties make InAs/GaSb superlattices an important material system for infrared detection. However, they have not yet exceeded the performance of HgCdTe detectors because of a high level of dark current. Figure 1.4 shows the comparison of the dark current in photodetectors with various absorber materials. The high dark-current exhibited by InAs/GaSb T2SLs is attributed to short carrier lifetimes limited by Shockley-Read-Hall (SRH) centers. It has been hypothesized that native defects associated with GaSb are responsible for the SRH-limited minority carrier lifetimes observed in InAs/GaSb T2SLs [13]. The InAs/InAsSb superlattices, on the other hand, has shown to be a potential type-II alternative to the InAs/GaSb system for infrared photodetectors due to their much longer recombination lifetimes [14, 15]. The minority carrier lifetime is an essential parameter for the IR detector performance which reflects the quality of the IR absorbing material and improves the performance

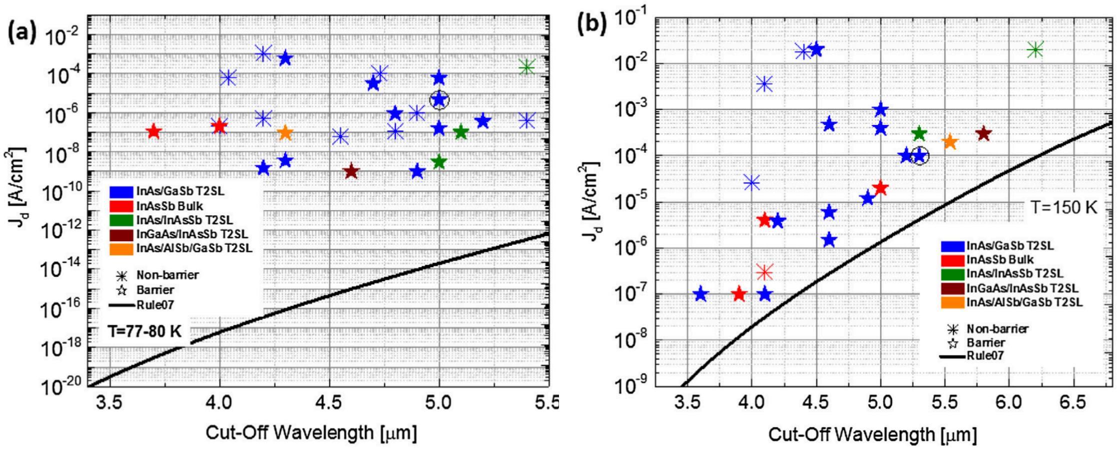

Figure 1.4: Comparison of the experimental dark current density of T2SL MWIR detectors at (a) 80 and (b) 150 K. The Rule07, MCT dark current density is shown with solid black lines (Adopted form [12]).

of the device such as the quantum efficiency and detector responsivity. Therefore, an understanding of the link between material properties, device properties, and device performance offer potential avenues for improving T2SL performance.

1.3 Detector Architectures based on T2SLs

1.3.1 Single uni-polar barrier

Single uni-polar barrier detectors consist of an absorber layer and a contact layer that sandwich a barrier layer that blocks one carrier type and allows unobstructed flow of the other. Such structures offer advantages in their material growth in that they do not require both *p*- and *n*-type doped material, they reduce dark current generation-recombination mechanisms, they reduce surface leakage current by incorporating a shallow etch processing scheme, and can remove Auger recombination currents due to *p*-type material by not having a narrow band gap *p*-type layer as in the case of the *nBn* detector. Variations of the single uni-polar barrier detectors include the *nBn*, *pBn*, and *pBn*, are shown in Fig. 1.5 The blocked carriers in question can either be electrons or holes depending on the properties of the material being used in the different material layers. The band-offset tunability is crucial for the realization of barrier devices. Barrier layers are selected such that the hole barrier (HB) layer offers an unimpeded flow of electrons while blocking holes and the electron barrier (EB) layer blocks off electrons while allowing unimpeded flow of holes. Hence, one requires EB and HB layers to have zero valence band offset (VBO) and conduction band-offset (CBO) with the absorber layer, respectively[16].

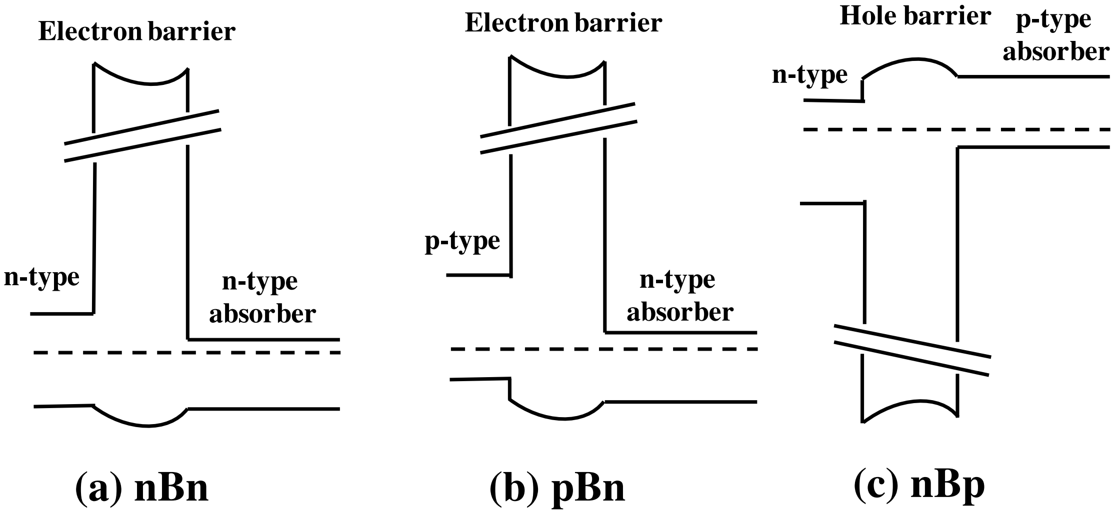

Figure 1.5: Schematic of barrier structures: (a) *nBn*, (b) *pBn*, and (c) *nBp*.

The motivation for such a structure was to achieve the advantages of conventional device technologies of photoconductors and *pn* photodiodes, without some of the disadvantages associated with them. It was first proposed by Anthony White in a patent in 1983 to be used with HgCdTe material system [17]. In 2006, Gary Wicks and Shimon Maimon[18] published a paper proposing a barrier heterostructure in which they coined the term '*nBn*'. Their structure consisted of an InAs absorber and contact region and an AlAsSb barrier layer. The motivation for their structure is the reduction of Shockley-Read-Hall generation-recombination current and surface leakage current. This, in turn, allows the detector to operate with similar performance as a traditional photodiode at a higher operating temperature, or with better performance at a similar operating temperature.

In the *pBn* variant of this design (or *nBp* also), an actual photovoltaic device with a built-in bias between the p and n region that falls across the barrier layer [19, 20]. The *pBn* device does not operate like the two other variations, *nBn* and *pBp*, in which the operation is similar to a photoconductor that requires an applied bias. A *pBn* structure is an actual photodiode with a built-in potential that can operate with zero applied bias. In the *pBn* structure, as shown schematically in Fig.1.5(b), a wide band gap EB layer is inserted between p^+ contact layer and lightly doped n-type absorber region. This facilitates a drop of electric filed mostly across the EB layer, rather than across the narrow-gap absorber region, and hence reducing SRH dark currents and tunneling currents. The barrier layer also prevents the diffusion of minority carrier electrons from p^+ contact layer into the absorber region and hence further reducing the dark current.

1.4 Vertical Transport

1.4.1 Isotropic vs. Anisotropic Systems

The isotropic material, such as bulk semiconductors, is the one in which all three directions are equivalent to the motion of the carriers. Whereas in an anisotropic material, such as a quantum well, this isotropy is broken due to the multiple repeats of alternating materials in one direction (growth-direction). The latter leads to a quantum-confined structure in which the motion of the carriers is confined in one (quantum wells) or more directions (quantum wires, quantum dots) by periodic potential. Quantum size effects become important when the thickness of the layer becomes comparable with the de Broglie wavelength of the electrons or holes. This behavior is seen for multiple quantum wells (MQWs) with large barrier thickness, in which the motion of the electrons and holes will be quantized in the growth (z) direction. This quantum confinement leads to the discrete energy bands with localized wave functions within the walls. The motion in the other two directions (i.e., the xy plane) is still free, and so we have quasi-two-dimensional behavior. Superlattice materials are an extension of such an anisotropic system in which the barrier thickness is reduced; hence, the wave functions of neighboring wells begin to overlap, leading to the formation of the delocalized miniband. The wave functions in the minibands are delocalized throughout the whole SL. The width of the miniband depends on the cross-well coupling, which is determined by the barrier thickness and the decay constant.

Transport in superlattices has much in common with bulk transport as well as many significant differences. The carrier dynamics perpendicular to the interfaces, where confinement occurs, gives rise to the quantization of the motion in the z-direction[21]. There are three main consequences due to the reduced dimensionality. Firstly, the quantization energy shifts the effective band edge to higher energy, which provides an extra degree of freedom in the art of bandgap engineering. Secondly, the confinement keeps the electrons and holes closer together and hence increases the radiative recombination probability. Finally, the density of states becomes independent of energy, in contrast to 3-D materials, where the density of states is proportional to $E^{1/2}$. The 2-D density of states alters the effect of the scattering mechanisms with respect to the 3-D case[22].

Highly anisotropic conduction properties of superlattices imply different transport characteristics along the horizontal and vertical directions. As shown in Fig. 1.6, along with the vertical direction, defined as orthogonal to the layer interfaces, charge carriers transport through minibands created by the series of potential wells/barriers. On the other hand, in the horizontal or in-plane direction, defined as parallel to the interfaces, they are free to move in the typical parabolic bands.

The vertical transport is of immense scientific and technological interest since most T2SL devices use a vertical architecture. Therefore, the transport of carriers along the vertical direction has paramount importance and must be understood to optimize T2SL device performance. Hence, to realize the anticipated potential of T2SLs, understanding vertical carrier transport characteristics such as mobility, effective masses, diffusion length and carrier lifetimes is required. Figure 1.7 illustrates

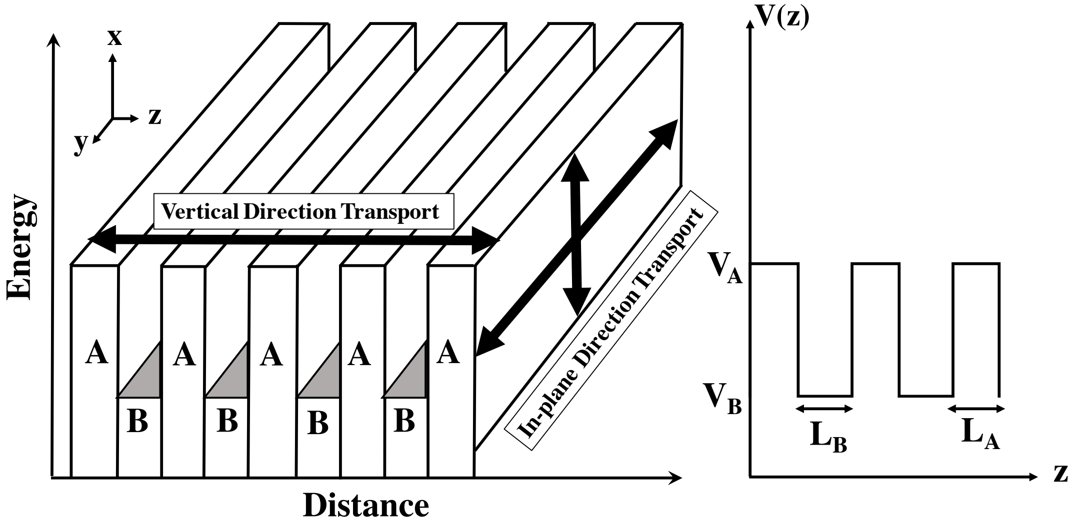

Figure 1.6: Schematic of superlattice cross-section; Z axis denotes the growth-axis or vertical direction, X-Y plane denotes the in-plane or horizontal direction. The superlattice is formed by alternating layers of wide and narrow band gap materials (A and B) grown along the Z axis. The effective potential experienced by electrons is shown on the right.

some of the main limiting factors of vertical transport, most of which are most of which are originated of such an anisotropy in superlattices. These factors lead to degraded transport in the superlattices, especially along the vertical direction.

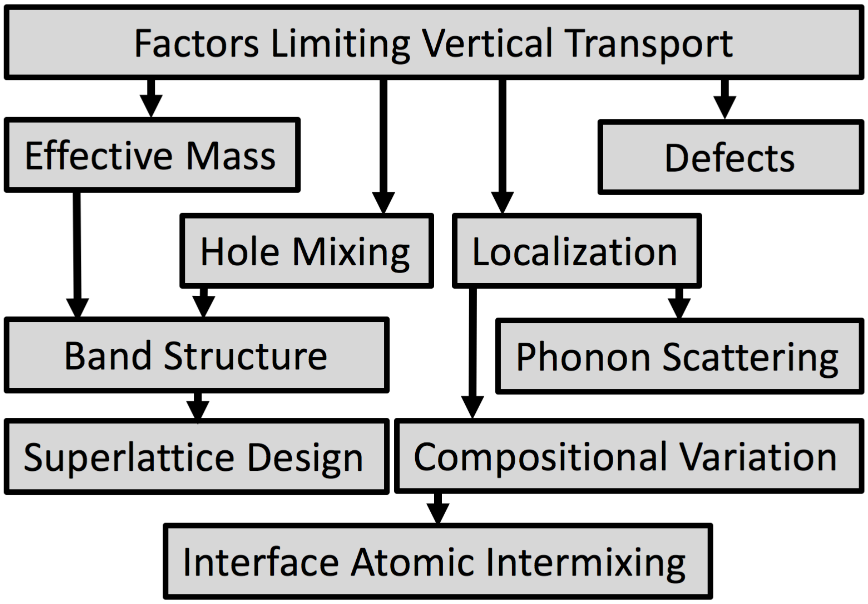

Figure 1.7: Summarizes the factors limiting vertical transport in type-II superlattices.

Localization is one of the main influential factors on transport and degrades the carrier vertical transport, and its role should be considered in the evaluation of type-II superlattice photodetectors. In the semi-classical study of transport in superlattices, disorders such as structural and phonon-induced disorders are responsible in destroying the long-range coherence of the electron states, and as a result lead to localization through different scattering mechanisms, such as ionized impurity scattering, and interface roughness scattering (IRS).

Phonons-induced random fluctuations of atomic positions can change the transport mechanism from miniband transport to phonon-assisted tunneling, called 'hopping', by disturbing the strict periodicity of the lattice. The induced phonon-scattering enhances hopping while inhibiting band conduction. Phonon emission and absorption processes are temperature-dependent. In addition, scattering is proportional to the tunneling probability, defined by phonon scattering time, τ, which has a strong temperature dependency. As a result, the transport mechanism can change from miniband conduction to hopping conduction between disorder localized states with temperatures[23], which affect the mobility substantially. A typical localization length can be given by

$$\delta l = \frac{d\Delta}{\delta E} \tag{1.1}$$

where δE is the inhomogeneous energy broadening, d is the superlattice period, and Δ is the miniband half-width. Miniband conduction occurs when the miniband width is greater than the collision broadening $\delta E < \Delta$. This also implies the condition $\delta l < d$,[24] to have superlattice Bloch states and to avoid localization along the superlattice growth axis. Therefore, superlattice miniband conduction is related to the superlattice structural quality, in particular, the interface perfection in superlattices with narrow minibands. So, microscopic fluctuation of the composition of constituent layers, as well as interface roughness, can lead to spatially dependent structural disorders, and electron mobility degradation[9].

The quality of the superlattices is determined basically by the quality of the interfaces. Surface roughness destroys the coherence of electron tunneling and measurement of roughness parameters is very important technologically. The effect of IRS has been studied both theoretically and experimentally [25, 26, 27]. Roughness fluctuation along the interface is usually represented as a Gaussian distribution of the in-plane position ($r_{||}$) and determined by roughness height Δ, and a correlation length Λ, as [25]

$$< \Delta(r_{||})\Delta(r'_{||}) >= \Delta^2 \exp - \frac{|r_{||} - r'_{||}|^2}{\Lambda^2} \tag{1.2}$$

Vertical mobility has found to be strictly dependent on the interface characteristics and decreases with increasing Δ and Λ [25].

From above descriptions, it is obvious that compositional variation plays an important role in carrier localization and degradation of transport in superlattices.

Effective mass is another influential parameters in transport. Electrons have lighter effective mass relative to holes and hence are faster, thus contribute more to the mean velocity. Lighter effective mass leads to the electron mobility becoming an order of magnitude larger than that of the hole typically. So, holes play the dominant role in determining the ambipolar diffusion coefficient since the ambipolar diffusion is highly dependent on the slower carrier species. Effective mass is related to the electronic band structure of the material, which in turn is a function of material design and composition.

1.5 Significance of the Present Work

The focus of research on transport study in T2SLs is relatively new. Table. 1.2 summarizes the recent results on the transport in T2SLs, which indicate the deficiency of information on this material system, and that little is known about the role of carrier transport. The effect of factors such as the structural and superlattice design, growth techniques, scattering mechanisms/interfacial roughness, and carriers effective masses on transport in T2SLs, and consequently on the performance of the T2SL-based device, is still unknown.

This work seeks to be among the continuing efforts to improve type-II superlattices IR detectors performance by gaining physical insight into these materials and improve this technology. For this purpose, various techniques including electron-beam-induced-current ($EBIC$) measurement, quantum efficiency modeling, and photocurrent-voltage measurement are used to probe the spatial and temporal dynamics of the charge carriers, and to quantify the drift/diffusion characteristics in T2SLs.

Table 1.2: A summary of the results of various minority carriers transport parameters in III-V type-II superlattices, measured with different approaches. Here, InAs/GaSb superlattices are referred to as 'Ga-containing T2SLs', and InAs/InAsSb superlattices are referred to as 'Ga-free T2SLs'.

	Material	**Mobility** ($\frac{cm^2}{Vs}$)	**Diffusion Length** (nm)	**Diffusivity** ($\frac{cm^2}{s}$)	**Year & Ref.**
Ga-Containing T2SLs	InAs/GaSb SL, MWIR		L_e: 275 at 5.3 K L_e: 355 at 100 K		2004[28]
	InAs/In$_{0.25}$GaSb		L_h: 200		2015[29]
	InAs/GaSb	μ_h: 5000 at 80K	L_h: 3500		2009[30]
	InAs/GaSb	μ_h: 8000			2010[31]
	InAs/GaSb , pin		L_h: 520	D_h: 0.664	2016[32]
	InAs/GaSb , MWIR			p-type: D_e: 4.7±0.5 undoped: D_h: 0.0±0.03	2013[33]
	InAs/GaSb , MWIR	μ_e: 1100, μ_h: 100		S/D_e: 400 cm^{-1}, S/D_h: 1000 cm^{-1}	2013[34]
	InGaAs/InAsSb (Ga=5%), MWIR	μ_h: increases from 10 to 40 for 80K to 200K	L_h: increases from 600 to 1000 for 80K to 200K		2017[35]
	InGaAs/InAsSb (Ga=20%), MWIR	μ_h: increases from 30 to 100 for 80K to 200K	L_h: increases from 900 to 1500 for 80K to 200K		2017[35]
Ga-Free T2SLs	InAs/InAsSb , MWIR, In-plane at 293 K	μ_h: 2380±120, 2220±120, 2420±120 for three different SL period thicknesses		D_h: 56±3, 60±3, 61±3 for three different SL period thicknesses	2016[36]
	InAs/InAsSb SL, MWIR, at 6K	μ_h:60	L_h: 750	D_h: 3×10^{-2}, S/D_h: $10^6 cm^{-1}$	2015[37]
	InAs/InAsSb , MWIR, Various temperatures	μ_h:360 at 129K 2 @ 30K	L_h: decreases from 2550 to 280 for 110K to 20K	D_h: decreases from 3.28 to 0.0036 for 110K to 20K	2017[38]
	bulk InAsSb	μ_h: 800	L_h: 9000		2014[39]

1.5.1 Thesis Objective

The initial motivation for this work stems from the need to assess the material quality of T2SL and performance of the photodetectors based on this material system.

Carrier transport properties are in fact among the quantities that bridge between the fundamental material quality and the device characteristics. Therefore, they can be used to manifest the material quality so as to enable the improvement and optimization of T2SL growth and T2SL technologies as well as post-growth processing steps for device fabrication.

Among different T2SLs, InAs/GaSb have distinct advantages compared to other available materials with type-II band alignment such as InAs/InAsSb T2SLs. Although InAs/InAsSb superlattices offer the ease of growth and higher minority carrier lifetime, the InAs/GaSb superlattice has a wider cutoff wavelength adjustability that covers short-wavelength infrared (SWIR) as well in addition to MWIR to VLWIR. Also, it can achieve the same LWIR cutoff wavelengths as the InAs/InAsSb superlattices but with shorter periods, which leads to stronger oscillator strengths and larger absorption coefficients [40]. On the other hand, *p*-type absorber offer better vertical transport due to the lighter effective mass of the minority carrier electrons, However, InAs/InAsSb superlattice materials are not suitable for *p*-type absorber, due to the surface issues [40], while InAs/GaSb superlattice infrared detectors are most commonly implemented using *p*-type absorbers. For this purpose, we chose to study the InAs/GaSb superlattice photodetector with *p*-type absorber.

So, the principal driver for the work undertaken in this dissertation is to be able to characterize the minority carrier transport in *p*-type InAs/GaSb T2SL and have confidence in the results obtained. The end goal of the investigations is to: (1) establish a platform for repetitive and reliable measurement of transport properties in T2SLs;
(2) measure the minority transport properties such as diffusion length, diffusion coefficient, and mobility along the vertical (growth) direction in the InAs/GaSb T2SL;
(3) compare the results of the minority carrier mobility and its accuracy calculated using different techniques, and with our expectations based on the dominant scat-

tering mechanism at various temperatures.

1.6 Outline of the Thesis

This dissertation is divided into six chapters, the first being the introduction. Chapter two establishes the main theoretical platform used throughout this work, including the main optoelectronic equations such as transport, and also quantum efficiency, dark current and carrier dynamics in semiconductors. Chapter three describes the theoretical and experimental considerations in EBIC technique. Chapter four presents work on the drift and diffusion on a selected sample with results and discussion on each characterization performed. Chapter five will present the recent results of a study on the electronic properties of a series of superlattices within the density-functional theory and many-body perturbative formalism. Finally, chapter six summarizes the work of this dissertation and provides an outlook for future endeavors.

In this chapter, a review of semiconductor theory is presented. The review begins with a description of nonequilibrium charge carrier dynamics with the underlying physical equations including continuity equations and current density equations in Section 2.1. This section is followed by the derivation of the standard mathematical model for carrier charge transport in Section 2.2, including a summary of transport properties, and a discussion on the miniband transport. The mathematical model for the charge carrier lifetime is discussed in Section 2.3. Extended discussions on the current-voltage characteristics including the dark current and quantum efficiency models are presented in Sections 2.4 and 2.5, respectively. The chapter finishes with a summary in Section 2.6.

Chapter 2

Nonequilibrium Charge Carrier Dynamics

There are several ways that can be utilized to raise a semiconductor from thermal equilibrium to an excited state. Such excitation process may be known as generation processes if they generate free electrons or free holes, for example through an absorption of a photon. For each generation or excitation process, there is a converse recombination or de-excitation process, in which electrons undergo transitions to lower energy states and liberate the energy difference in some form. The maintenance of free and trapped carrier densities in thermal equilibrium is determined by a dynamics balance of generation and recombination processes, known as the principle of detailed balance. This principle is a statistical concept stating that for a system in thermal equilibrium, the rates of a process and its inverse are equal and balance in detail [41].

The action of an external stimulus of some kind will change the carrier densities to be functions of space and time. The rate of change of each can be expressed through a continuity equation. A density $n(x, y, z, t)$ of conduction band electron in a specified volume, for example, tends to change as a net result of (a) generation processes; (b) recombination processes; and (c) carrier diffusion and drift. The term 'generation processes' includes all the mechanisms by which electrons may be thermally excited to the conduction band from the valence band and from the impurity states. In addition to the generation and recombination, the passage of current can tend to change the local electron density. As a result of all these processes, the rate of change of local free electron density can be summarized in the continuity equation

Continuity Equations

Starting from Ampere's law in Maxwell's equation as follows

$$\nabla \times \mathbf{H} = \mathbf{J_p} + \mathbf{J_n} + \frac{\partial}{\partial t}\mathbf{D}, \tag{2.1}$$

where $\mathbf{H}$ is the magnetic field $[A/m]$, and $\mathbf{D}$ is the electric displacement flux density (C/m^2), and $\mathbf{J_n}$ and $\mathbf{J_p}$ are the electron and hole current densities, respectively, one can take the divergence of the sides as

$$0 = \nabla.(\nabla \times \mathbf{H}) = \nabla.(\mathbf{J_p} + \mathbf{J_n}) + \frac{\partial}{\partial t}\nabla.\mathbf{D}. \tag{2.2}$$

Now, using the Poisson equation, with $\rho = n - p + N_D^+ - N_A^-$, where N_D^+ is the ionized donor concentration, and N_A^- is the ionized acceptor concentration, we have

$$\nabla.(\mathbf{J_p} + \mathbf{J_n}) + \frac{\partial}{\partial t}\rho = 0. \tag{2.3}$$

Assuming $N_D^+ - N_A^-$ are independent of time, the current continuity equations for electrons and holes are obtained separately as [42]

$$\frac{\partial n}{\partial t} = G_n - U_n + \frac{1}{q}\nabla.\mathbf{J_n}, \tag{2.4}$$

$$\frac{\partial p}{\partial t} = G_p - U_p + \frac{1}{q}\nabla.\mathbf{J_p}. \tag{2.5}$$

Here, G_n and G_p are the electron and hole generation rates $[cm^{-3}sec^{-1}]$, respectively, due to external influence such as optical excitation with high energy photons or impact ionization under large electric fields. And U_n and U_p are the electron and hole recombination rates, respectively, and it is assumed $G_n - U_n = U_p - G_p$.

Upon any excitation, the general tendency of the non-equilibrium carriers is to try and restore themselves towards the equilibrium condition. The strength of this tendency can be approximated to be proportional to the excess density ($\delta n = n - n_0$). For this reason, the recombination terms (U_n and U_p) in the above equations, can be expressed as $-\delta n/\tau_n$, where τ_n is the electron bulk lifetime and will either be completely independent of δn or will depend on it. Analogous with the phenomena of the conduction band, a bulk lifetime τ_p can be defined to characterize the dynamics of a situation involving a uniform excess hole density $\delta p = (p - p_0)$ in the valence band. Under the charge neutrality condition, the excess minority and the excess majority carriers have an equal concentration ($\delta n = \delta p$).

Current Density Equations

In a *1-D* system, the drift and diffusion components can be combined to give the currents

$$\mathbf{J_n} = q\mu_p p\mathbf{E} + qD_p\nabla p, \tag{2.6}$$

$$\mathbf{J_p} = q\mu_n n\mathbf{E} + qD_n\nabla n, \tag{2.7}$$

where $\mathbf{J_n}$ and $\mathbf{J_p}$ consist of the drift component due to the field, E, and the diffusion component due to the carrier concentration gradient. The electron and hole mobilities (μ_n and μ_p) are related to the carrier diffusion constants (D_n and D_p), for a non-degenerate semiconductor, by Einstein relationship ($D = (\frac{kT}{q})\mu$).

For one-dimensional case, we can write current densities as

$$j_n = n\mu_n\mathbf{E} - D_n\frac{\partial(\delta n)}{\partial t}. \tag{2.8}$$

and

$$j_p = p\mu_p\mathbf{E} - D_p\frac{\partial(\delta p)}{\partial t}. \tag{2.9}$$

2.1 Carrier Transport Equations

Continuity equations for a one-dimensional case under a low-injection condition, using the carrier density equations, reduce to the time-dependent diffusion equations as following

$$\frac{\partial n_p}{\partial t} = G_n - \frac{n_p - n_{p0}}{\tau_n} + n_p\mu_n\frac{\partial E}{\partial x} + \mu_n E\frac{\partial n_p}{\partial x} + D_n\frac{\partial^2 n_p}{\partial x^2} \quad \text{for p-type} \tag{2.10}$$

$$\frac{\partial p_n}{\partial t} = G_p - \frac{p_n - p_{n0}}{\tau_n} + p_n\mu_p\frac{\partial E}{\partial x} + \mu_p E\frac{\partial p_n}{\partial x} + D_p\frac{\partial^2 p_n}{\partial x^2} \quad \text{for n-type} \tag{2.11}$$

Eliminating the term $\partial E/\partial x$ in the continuity equations under steady-state condition, with the condition that $(p_n - p_{n0})/\tau_p$ equals $(n_p - n_{p0})/\tau_n$, one can write

$$\begin{aligned} &-\frac{p_n - p_{n0}}{\tau_p} + \mu_a E(p_n\frac{\partial n_n}{\partial x} - n_n\frac{\partial p_n}{\partial x})/(p_n - n_n)+ \\ &\qquad D_a(p_n\frac{\partial^2 n_n}{\partial x^2} + n_n\frac{\partial x^2}{\partial^2 p_n})/(p_n + n_n) = 0, \end{aligned} \tag{2.12}$$

where, D_a and μ_a are the ambipolar diffusion coefficient, and ambipolar mobility, respectively.

Ambipolar transport refers to the movement of charge carriers in semiconductors, including drift and diffusion of excess electrons and holes with a single effective mobility or diffusion coefficient, and is used to demonstrate the transport behavior of excess carriers generated in a semiconductor material. At thermal equilibrium, the net concentration of electrons and holes are identical and independent of time or position. However, when the excess electrons and holes are created at a particular point in space in a semiconductor with an applied electric field, the induced internal electric field will create an attracting force that keeps the electrons and holes moving together, called drift. The rate of drift is governed by the carriers mobility, μ_a, as

$$\mu_a = \mu_n \mu_p (p_n - n_n)/(n_n \mu_n + p_n \mu_p). \tag{2.13}$$

On the other hand, the excess carrier concentration gradient,$\frac{\delta n}{dx}$, will result in diffusion of the carriers, which is a result of the spatial inhomogeneity of carrier concentration and is described by a diffusion coefficient, D_a, expressed as

$$D_a = D_n D_p (p_n + n_n)/(n_n D_n + p_n D_p). \tag{2.14}$$

It is not always known what extent both diffusion and drift are involved in charge movements, and sometimes the term drift/diffusion is used, unless it is known that only one of these mechanisms prevails.

Equation 2.12 is a nonlinear differential equation in which the coefficients are not constant, in general. However, under the assumption of low-level injection, when the concentration of excess minority carrier is below the concentration of majority carrier at thermal-equilibrium in the material (e.g., $p_n << n_n = n_{n0}$ in the n-type semiconductor), Eq. 2.12 can be simplified and linearized as [43]

$$-\frac{p_n - p_{n0}}{\tau_p} + \mu_p E \frac{\partial p_n}{\partial x} + D_p \frac{\partial^2 p_n}{\partial x^2} = 0, \tag{2.15}$$

and

$$-\frac{n_p - n_{p0}}{\tau_n} + \mu_n E \frac{\partial n_p}{\partial x} + D_n \frac{\partial^2 n_n}{\partial x^2} = 0, \tag{2.16}$$

for p-type and n-type materials, respectively. Here, τ_n and τ_p are the electron and hole recombination lifetimes. Under the low-level injection condition, the transport and recombination parameters are governed by the minority carrier parameters, which are constants.

Most of the modeling tools accompanying the experimental measurements to investigate transport are based on an analytical solution of Eqs. (2.15,2.16) considering boundary conditions, which are chosen based on the geometry and structure of the sample. The analytical solution is possible only if parameters, such as lifetime, mobility, and doping level in the structure, are assumed to be constant. Otherwise, the transport equation should be solved without linearization on the external perturbation such as an applied electric field or optical illumination with the help of the numerical techniques.

2.1.1 Carrier Transport Properties

As mentioned earlier, mobility is used to describe drift in a semiconductor and is defined as the ratio between the mean velocity, <v>, and the electric field **E**, if **E** is uniform and constant, as [9]

$$\mu = \frac{<\mathbf{v}>}{\mathbf{E}}. \tag{2.17}$$

Assuming that carriers are subject to several collisions described by a relaxation time, τ, that is the mean time elapsed after each collision in linear-response conditions (the field is so weak that the carriers gain insignificant energy during the free flight) one can show that [9]

$$< \mathbf{v} >= \frac{q\mathbf{E}}{m}\tau \tag{2.18}$$

which yields the mobility as

$$\mu_n = \frac{-e < \tau >_n}{m_n^*}, \tag{2.19}$$

$$\mu_p = \frac{-e < \tau >_p}{m_p^*}, \tag{2.20}$$

for the minority carriers in the p-type and n-type materials with m_n^* and m_p^* as effective masses, respectively. If mobility was to be described more accurately, one needs to consider using the weighted relaxation time with the carrier's energy. From the above, different scattering mechanisms such as ionized impurity and electron-hole scattering can significantly affect the mobility through changing the relaxation time.

Mobility can also be expressed based on the conductivity, which is described as the ratio between the current density, $j = qn < v >$, and the applied electric field, $\mathbf{E}$. For the case of the n-type material,

$$\mu_n = \frac{\sigma}{qn} = \frac{1}{qn\rho}, \tag{2.21}$$

where n is the majority carrier density, and ρ is the resistivity. these two mobility definitions are referred to as the drift mobility and the conductivity mobility. There is a different mobility, the Hall mobility, which is determined by the Hall Effect and is related to the conductivity mobility by the Hall scattering factor [44].

The carrier drift mobility and diffusion coefficient, D, are related through the Einstein relations as [43]

$$D_n = \frac{k_B T \mu_n}{q}, \tag{2.22}$$

$$D_p = \frac{k_B T \mu_p}{q}, \tag{2.23}$$

written for electrons and holes, respectively, where k_B is the Planck's constant, T is the temperature, q is the fundamental charge of an electron. It is worth mentioning that the Einstein relation is only valid for equilibrium conditions, but it is widely used as an approximation.

Transport in semiconductors can be expressed with the average distance that the relevant charge moves in the semiconductor before their recombination/extraction from it. This is usually referred to as the diffusion length and is related to the diffusion coefficient and lifetime as

$$L_n = \sqrt{D_n \tau_n}, \tag{2.24}$$

and

$$L_p = \sqrt{D_p \tau_p}, \tag{2.25}$$

for minority electron and hole, respectively. Carrier mobility, diffusion coefficient, and diffusion length are usually refereed to as transport properties.

Next section briefly explains the concept of miniband transport in superlattices semiconductors.

2.1.2 Miniband Conduction

Superlattices have consisted of multiple coupled quantum wells in which the barrier width is sufficiently decreased such that the electron wave functions overlap in adjacent barriers and the envelope wavefunction of the superlattice is spread over all the wells due to tunneling through the thin barriers. In this case, all the single-well levels are at the resonance and their coupling produces superlattice states that are completely delocalized over the whole superlattice. This leads to the formation of a continuum of energies called miniband with a width of 2Δ. The miniband width along the z-direction depends on the inter-well coupling and therefore on the period, and can be tailored to values as low as 1 meV up to a few 100 meV by the variations of the barrier and well layer thicknesses as well as the band offset. Figure 2.1 depicts the potential and subband diagram of superlattices, with the miniband shown along the superlattices axis.

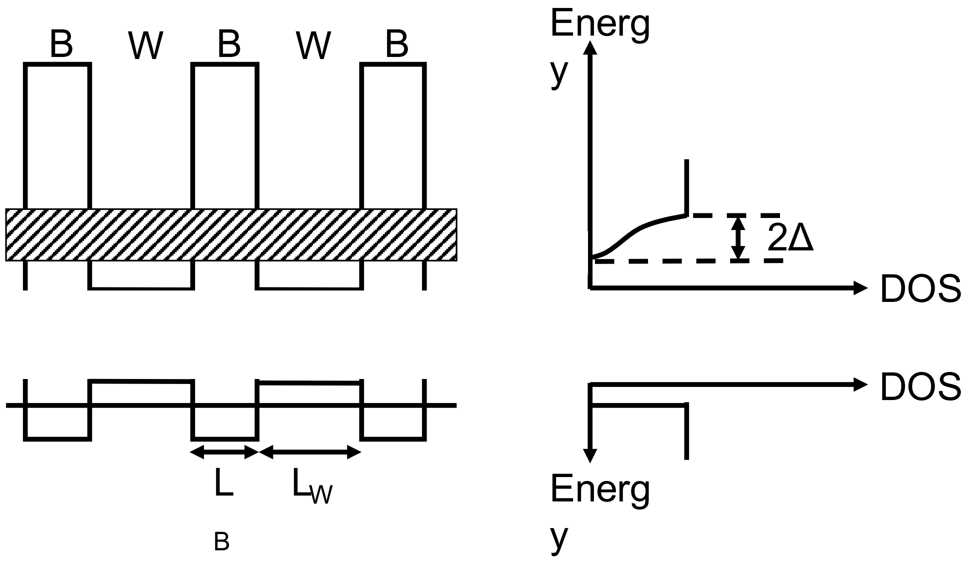

Figure 2.1: Potential and subband energy diagrams of superlattices.

The extent of the wave functions is limited to a typical coherence length, which in turn is determined by deviations from the ideal periodicity. Furthermore, the basic phenomenon at the origin of the very existence of the miniband is tunneling. Because of the exponential decay of the electron and hole wave functions with distance, tunneling requires extremely thin semiconductor layer in order to obtain appreciable miniband width. So, the criteria for carriers to have the miniband conduction is that the broadening due to different mechanisms such as a scattering or potential fluctuations be smaller than the miniband width, which can be written as [45]

$$\delta E < \Delta, \tag{2.26}$$

where δE is the inhomogeneous energy broadening, and Δ is the miniband half-width. This condition for the miniband conduction can be met when the low-field mean free path exceeds the superlattice period along the superlattice axis. Otherwise, the electrons do not feel the miniband dispersion and are confined in the z-direction. A typical localization length can be given by [24]

$$\delta l = \frac{d\Delta}{\delta E}, \tag{2.27}$$

where d is the superlattice period. This also implies the condition $\delta l < d$,[24] to have superlattice Bloch states and to avoid localization along the superlattice growth axis.

Superlattices can show different characteristics along growth and in-plane directions and behave as anisotropic 3-D semiconductor in the case of the miniband conduction. This anisotropy originates from different effective masses in the two directions. Along the superlattice axis, the carrier mobility as a function of the miniband width and superlattice period is expressed as [45]

$$\mu_z = \frac{e\Delta d^2}{\hbar^2}\tau, \tag{2.28}$$

where τ is the relaxation time for the momentum $p_{||} = \hbar k_{||}$. Using the energy dispersion relation, $E(k) = \Delta(1 - cos(k_{||}d))$, for a one-dimentional model, the band-edge effective mass along the superlattice growth axis can be expressed as [45]

$$m_z = (\frac{\hbar^2}{\frac{d^2E}{dk_z^2}})_{k_z=0} = \frac{\hbar^2}{\Delta d^2}, \tag{2.29}$$

Equations (2.28, 2.29) show the dependency of mobility and the carrier effective mass on the miniband width. The tunneling probability depends on the effective mass as well, so lighter carriers (electrons) can move much faster than the heavier carriers (holes), which can lead to hole localization.

The condition for observing single miniband transport is the absence of any interminiband transfer by any process. In particular, the energy gap between two subsequent minibands must be much larger than $k_B T$, even in the presence of the applied field. A small enough minigap or a high electric field along the superlattice growth direction can lead to an interesting phenomenon, known as the Wannier-Stark (WS) ladder, in which the miniband is split into discrete, equidistant energy levels, which are localized around one period of the superlattice. WS states originated from two different minibands can line up and hence interminiband tunneling can happen. This means in the time domain that electrons can traverse the entire mini-Brillouin-zone without being scattered and thus perform Bloch oscillations. Both the Wannier-Stark ladder and Bloch oscillations can be considered as different aspects of the electric field-induced localization of electrons in a periodic potential [46]. These phenomena can be especially important in high electric field regions, such as depletion regions. However, in the case of low electric fields, the coherence length is determined by the superlattice disorder or, in a perfect superlattice, by the interface roughness, impurities, phonons, alloying or any other factor that limits the coherence length in the bulk material.

2.2 Charge Carrier Lifetime

When an electron drops from the conduction band into an empty state of the valence band, or to a localized state whose energy is indicated by a position within the intrinsic gap, the recombination energy is transformed into some other kind of energy such as electromagnetic radiation, lattice vibration or kinetic energy of another free particle. These processes can be classified into radiative and nonradiative. The term radiative recombination is applied when a photon is released as a carrier pair annihilates itself. For a direct radiative transition, all the energy is given to the photon. For an indirect transition, a phonon is either emitted or absorbed at the same time. The same principles hold for the transition of an electron from a localized state to an empty state in the valence band. The nonradiative transitions do not involve photons; they may involve the interaction with phonons or the exchange of energy and momentum with another electron or hole.

Figure 2.2 shows the schematic of the radiative and nonradiative (Auger, SRH) recombination processes in a semiconductor. The bulk recombination lifetime can be determined by theses recombination mechanism as

$$\tau^{-1} = \tau_{srh}^{-1} + \tau_{rad}^{-1} + \tau_{auger}^{-1}. \tag{2.30}$$

In the following, we discuss the theory to model each of these radiative and nonradiative recombination rates.

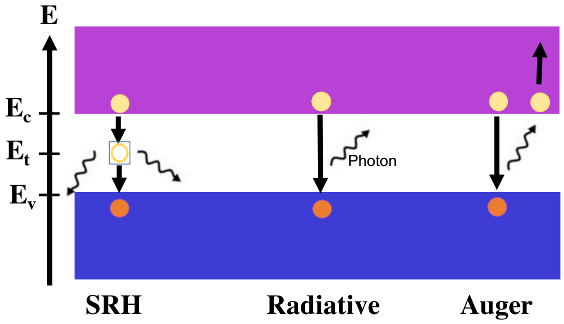

Figure 2.2: Carrier recombination mechanisms in semiconductors E_t is the 'trap' energy level within the band gap caused by the presence of a foreign atom or a structural defect.

Theoretical Model

Assuming a p-type material, i.e., $p_0 \gg n_0$, in the theory we discuss, we summarize the expressions used to calculate lifetime for the p-type absorber. The common parameters used throughout this analysis are equilibrium electron (n_0) and hole(p_0)

carrier concentrations, the energy gap (E_g), Boltzmann's constant (k_B), the temperature (T), and the effective electron (m_e), and hole (m_h) masses. Similar relations can be obtained for n-type materials.

Shockley-Read-Hall Recombination

SRH lifetime is due to the electron-hole-pair recombination through deep-level impurities or traps. The energy liberated during the recombination event is dissipated by lattice vibrations or phonons. The SRH lifetime can be characterized by the defect density N_t, SRH defect energy levels E_t, and the electron and hole defect capture cross-sections, σ_n and σ_p, respectively, as [47]

$$\tau_{srh}^{-1} = \frac{n_0 + p_0 + \Delta n}{\tau_{p_0}(n + n_1) + \tau_{n_0}(p + p_1)}, \tag{2.31}$$

where n_1, p_1, τ_{n_0}, and τ_{p_0} are defined as

$$n_1 = N_c exp(\frac{E_t - E_c}{k_B T}); \qquad p_1 = N_v exp(\frac{E_v - E_t}{k_B T}), \qquad \text{and} \tag{2.32}$$

$$\tau_{n_0} = \frac{1}{\sigma_n v_{th} N_T}; \qquad \tau_{p_0} = \frac{1}{\sigma_p v_{th} N_T}, \tag{2.33}$$

where v_n and v_p are the electron and hole thermal velocities, and σ_p and σ_n are assumed to be equal (=σ).

Equation 2.31 describes the density dependence of SRH recombination, and for a p-type material, can be further simplified for both low-level injection(ll), when the excess minority carrier density is low compared to the equilibrium majority carrier density, $\Delta n << p_0$, and high-level (hl) injection, when $\Delta n >> p_0$.

$$\tau_{srh}(ll) = \frac{n_1}{p_0}\tau_p + (1 + \frac{p_1}{p_0})\tau_n = \tau_n|_{\text{for } n_1, p_1 << p_0}, \text{and} \tag{2.34}$$

$$\tau_{srh}(hl) = \tau_p + \tau_n \tag{2.35}$$

The SRH process is therefore limited by the electron recombination lifetime, τ_n, in the minority carrier recombination regime for p-type material.

Radiative Recombination

The radiative lifetime is due to the recombination of electron-hole pair directly from band to band with energy carried away by photons and is given by [47]

$$\tau_{rad}^{-1} = B(n_0 + p_0 + \Delta p), \tag{2.36}$$

where B is the radiative recombination coefficient determined by the superlattice band structure and is related to the microscopic radiative coefficient (B_r) using Photon recycling factor ($B_r = B\Phi$). Photon recycling trends to unity for thin samples, however, as the active layer thickness increases, the contribution of the self-absorption followed by electron-hole generation and radiative recombination must be taken into account, which leads to $\Phi > 1$. [48]

Under ll and hl conditions, Eq. 2.36, for a p-type material, can be written as

$$\tau_{rad}^{-1}(ll) = \frac{1}{Bp_0}; \qquad \tau_{rad}^{-1}(ll) = \frac{1}{B\Delta n}. \tag{2.37}$$

Auger Recombination

Auger lifetime is a three-carrier process in which an electron-hole-pair recombine and a third carrier absorbs their recombination energy. This process is strongly dependent on the material's electronic structure, and in the case of the superlattices with highly nonparabolic energy bands requires significant computational resources, which has limited the accurate comparison between the experiment and the theoretical calculation. Precise determination of the Auger rate in out of the scope of the present work, and it will suffice to use the analytical expressions by Beattie, Landsberg, and Blakemore (BLB)[49] to have a rough estimation of the temperature dependent Auger lifetime. Based on these expressions, Auger lifetime can be calculated as [50]

$$\tau_{auger}^{-1} = C_n n(n_0 + p_0 + \Delta p) + C_p p(n_0 + p_0 + \Delta p), \tag{2.38}$$

where C_p and C_n are the Auger recombination coefficient for holes and electrons, respectively, which are also denoted as Auger-7 and Auger-1 processes [50]. Equation 2.38 under ll and hl condition can be reduced to

$$\tau_{auger}^{-1}(ll) = C_p p_0^2; \quad \tau_{auger}^{-1}(hl) = (C_n + C_p)\Delta n^2. \tag{2.39}$$

Generally, the Auger process involving two electrons and a hole, also known as Auger-1, is the dominant Auger recombination mechanism in n-type materials. While for the p-type materials, hole-dominated Auger processes involving two holes and an electron should also be considered in addition to the Auger-1 process[50]. There are nine hole-dominated Auger transitions labeled Auger-2 through Auger-10, among which the Auger-7 transition, where the light-hole band is involved, is the most important one[49]. So, the temperature-dependent Auger lifetime for a p-type material can be written as[51]

$$\tau_{auger}^{-1} = \frac{\tau_{auger-1}^{-1} + \tau_{auger-7}^{-1}}{\tau_{auger-1}^{-1} \cdot \tau_{auger-7}^{-1}}, \tag{2.40}$$

where, the expressions for $\tau_{auger-1}^{-1}$ is

$$\tau_{auger-1}^{-1} = \frac{(n_0 + p_0)n_0}{2n_i^2}(\tau_{auger-1}^{i})^{-1}, \tag{2.41}$$

with $\tau_{auger-1}^{i}$ calculated from

$$\tau_{auger-1}^{i} = \frac{h^3(4\pi\epsilon_0\epsilon_\infty)^2}{8(2\pi)^{5/2}q^4 m_0} \frac{(1+\mu)^{1/2}(1+2\mu)}{(m_e/m_o)|F_1F_2|^2}(\frac{E_g}{k_BT})^{3/2} \times exp[(\frac{1+2\mu}{1+\mu})(\frac{E_g}{k_BT})]. \tag{2.42}$$

Here, ϵ_∞ as the high frequency dielectric constant, $\mu = m_e/m_h$, and $|F_1F_2|$ is the Bloch's function overlap integral parameter, which was considered temperature-independent here.

The corresponding relation for the Auger-7 is then given by

$$\tau_{auger-7}^{-1} = \frac{(n_0 + p_0)p_0}{2n_i^2}(\tau_{auger-7}^i)^{-1}. \tag{2.43}$$

Here, $\tau_{auger-7}^i$ can be calculated using the ratio $\gamma = \tau_{auger-7}^i/\tau_{auger-1}^i$. γ has been previously calculated for the $HgCdTe$, and has shown to be in range of [0.5-6][51].

2.3 Current-Voltage Characteristics

In the neutral region where there is no electric field, Eq.(2.15) further reduces to

$$\frac{\partial^2 p_n}{\partial x^2} - \frac{p_n - p_{n0}}{D_p\tau_p} = 0. \tag{2.44}$$

The solution of above equation can be obtained using following boundary condition

$$p_n(\text{at depletion-region edge}) = p_{n0}e^{\frac{qV}{KT}}, \qquad p_n(x=\infty) = p_{n0}, \tag{2.45}$$

which gives

$$p_n - p_{n0} = p_{n0}(e^{qV/KT} - 1)e^{-(x-x_n)/L_p}, \tag{2.46}$$

where $L_p = \sqrt{D_p\tau_p}$, and at $x = x_n$. From the relation for the excess carrier densities, the total current is calculated as the sum of the terms

$$J_p = -qD_p\frac{\partial p_n}{\partial x}|_{x_n} = \frac{qD_p p_{n0}}{L_p}(e^{qV/KT} - 1) \tag{2.47}$$

and

$$J_n = -qD_n\frac{\partial n_p}{\partial x}|_{-x_p} = \frac{qD_n n_{p0}}{L_n}(e^{qV/KT} - 1), \tag{2.48}$$

to be equal to

$$J = J_n + J_p = (\frac{qD_p p_{n0}}{L_p} + \frac{qD_n n_{p0}}{L_n})(e^{qV/KT} - 1). \tag{2.49}$$

This is the ideal current-voltage characteristics derived based on assumptions, such as the low-injection condition and negligible generation-recombination current in the depletion layer. So it can only give a qualitative agreement. The departure from the ideal is mainly due to various reasons, including the surface effect, the generation and recombination of carriers in the depletion layer, the tunneling of carriers between states in the band gap, the high-injection condition, which may occur even at relatively small forward bias, and the series resistance effect. Each of these factors contributes to the total dark current in the device[52].

Dark current is an important figure of merit because it is typically the parameter that ultimately limits the performance of an infrared detector. The dark current mechanisms can be classified as fundamental mechanisms (depending only on material properties and device design), and defect-related mechanisms. The lattermost includes (1) generation-recombination and trap-assisted tunneling currents associated with the Shockley-Read-Hall (SRH) centers in the depletion region of detector; (2) a surface current associated with the surface states in the junction; and (3) diffusion current associated with Auger or radiative process in both the n- and p- extrinsic regions of the diode.

In the following, we discuss the theoretical modeling of the total dark current based on these mechanisms.

Theoretical Model

Assuming a neutral center and a constant electric field across the depletion region, and a triangular barrier, the simulated dark current is expressed as the sum of the diffusion current (I_{diff}), generation-recombination current (I_{gr}), tunneling current (including the trap-assisted (I_{TAT}) and band-to-band component (I_{BTB})) as [53, 54]

$$I_{tot} = I_{diff} + I_{gr} + I_{TAT} + I_{BTB}. \tag{2.50}$$

The first term in the right-hand-side of Eq. 2.50 is the diffusion current which can be written as

$$I_{diff} = A\sqrt{qk_BT}[\frac{n_i^2}{N_A}\sqrt{\frac{\mu_e}{\tau_e}}tanh(\frac{x_p}{L_p})](exp(\frac{qV_i}{k_BT}) - 1) \tag{2.51}$$

The second term, generation-recombination current, is a major current source in diodes with a high density of defects in the depletion region [53, 54].

$$I_{gr} = \frac{2An_iWk_BT}{(V_{bi} - V_i)\tau_{gr}}sinh(\frac{-qV_i}{2k_BT})f(b), \tag{2.52}$$

with

$$f(b) = \begin{cases} \frac{1}{2\sqrt{b^2-1}}ln\big(2b^2 + 2b\sqrt{b^2-1} - 1\big), & b > 1 \\ 1, & b = 1 \\ \frac{1}{\sqrt{1-b^2}}tan^{-1}(\frac{\sqrt{1-b^2}}{b}), & b < 1 \end{cases} \tag{2.53}$$

where $b = e^{\frac{-qV_i}{2k_BT}}$.

The third term, trap-assisted tunneling current, is due to carriers that occupy the trap states in the depletion region and tunnel across the junction. The transition occurs from an initially occupied energy band site to a trapping state with energy E_t, followed by tunneling from trap to the final energy band [53, 54].

$$I_{TAT} = \frac{Aq^2m_tM^2N_tV_i}{8\pi\hbar^3(E_g - E_t)}exp(\frac{-4\sqrt{2m_t(E_g - E_t)^3}}{3qE\hbar}) \tag{2.54}$$

The last term, band-to-band tunneling current, is from carriers that tunnel directly from the valence band on one side of the heterojunction to the conduction band located on the other side of the heterojunction. Generally, this type of current is apparent at large reverse bias because of the higher probability of band alignment [53, 54].

$$I_{BTB} = \frac{Aq^3 E V_i \sqrt{2m_{red}}}{4\pi^2 \hbar^2 \sqrt{E_g}} exp(\frac{-4\sqrt{2m_{red}E_g^3}}{3qE\hbar}) \tag{2.55}$$

In above expressions, A is the device area, q is the electron charge, k_B is the Boltzmann constant, T is the temperature, n_i is the intrinsic carrier concentration, N_A and N_D are the p- and n-regions doping concentrations, respectively, is the electron mobility, is the electron lifetime, V_i is the bias voltage, V_{bi} is the built-in potential, W is the depletion width, and is the generation-combination lifetime, is the Planck constant, m_t is the effective tunneling mass, N_t is the trap density, E_t is the trap energy location, measured from the valence band edge, and M^2 is a matrix element associated with the trap potential, assumed to be $eVcm^3$, Eg is the absorber's band gap, E is the electric field, m_{red} is the reduced effective mass and [53]

The total voltage (V_{app}) applied to the structure can be expressed as the sum of the voltage drops on an ohmic series resistance and the effective applied bias on the depletion region

$$V_{app} = V_i + R_s I, \tag{2.56}$$

for which R_s can be extracted from the forward bias voltage region of the differential resistance-voltage characteristic. Also, the depletion widths in the n- and p-regions and the electric field at the heterojunction can be defined as [54]

$$W_n^2 = \frac{2\epsilon_n \epsilon_p N_A (V_{bi} - V_i)}{qN_A(\epsilon_n N_D + \epsilon_p N_A)}, \tag{2.57}$$

$$W_p^2 = \frac{2\epsilon_n \epsilon_p N_D (V_{bi} - V_i)}{qN_D(\epsilon_n N_D + \epsilon_p N_A)}, \tag{2.58}$$

$$E = \frac{\epsilon_n + \epsilon_p}{2} \sqrt{\frac{2q(V_{bi} - V_i) N_A N_D}{\epsilon_n \epsilon_p (\epsilon_p N_A + \epsilon_n N_D)}}, \tag{2.59}$$

where ϵ_n and ϵ_p are the dielectric constants in the n- and p-regions, respectively.

2.4 Quantum Efficiency Modeling

External Quantum Efficiency (EQE) measurement is one of the figures of merits of IR detectors used to appraise the applicability and relative performance of a given detector and can be used for interrogating the material transport properties. External quantum efficiency (EQE) can be determined as a product of the absorption efficiency and Internal quantum efficiency (IQE). IQE represents the ability to convert absorbed radiation into the useful signal output and can be determined as the number of electron-hole pairs generated per photon.

To determine EQE values, the relative spectral response of the device under test is measured relative to a reference detector with a constant quantum efficiency versus wavelength. Ultimately, the result is calibrated using a blackbody and narrow-band filter. The results, when used with semi-parametric modeling techniques, can be used to extract the parameters associated with the minority carriers.

The quantum efficiency of a detector is a function of the diffusion length, absorption coefficient, and surface recombination velocity. If these factors can be measured or calculated in prior, the QE can be predicted through the use of numerical/analytical calculations. Here, we use an analytical approach to estimate the minority carrier diffusion length using the calculated detector's QE [55].

Theoretical Model

Hovel derived an analytical model for calculating the quantum efficiency of a *pn* homojunction under optical illumination. This model is based on assumptions that if fulfilled can be used as a first principle approximation for estimating the device's performance. These assumptions are not strict, and one can benefit from low computational calculations even if they are violated to a degree in actual devices. A summary of these assumptions is presented in Table 2.1[55, 56].

Table 2.1: List of assumptions made in the derivation of the hovel model.

	Assumptions	**Remarks**
1	The low-level injection assumption $n_{p0} << p_{p0}$ (p-type), or $n_{n0} >> p_{n0}$ (n-type)	(i)D and μ are reduced to those of the minority carrier (ii)Electric field term in continuity equation is eliminated due to an essentially field-free, quasi-neutral region
2	Uniform material	N, μ, τ, L and D are spatially invariant and can be treated as constant coefficients in the continuity equation
3	The minority carrier concentration is equal to its equilibrium value at the depletion region edge	not valid when then diffusion length is short.
4	The absorption coefficient, α, retains its uniformity throughout each region in the material	α is a function of wavelength only
5	One electron-hole pair created for every photon absorbed	Internal absorption quantum efficiency, $\eta_\lambda = 1$
6	No generation or recombination in the depletion region	(i)Collection probability is equal to unity (ii) This is invalid in the case of defects and damaged top surface
7	Majority carriers do not contribute to the current	(i)The total current is assumed to be equal to the minority carrier current

We shall discuss the operation of *pn* photodiode in some detail with the help of

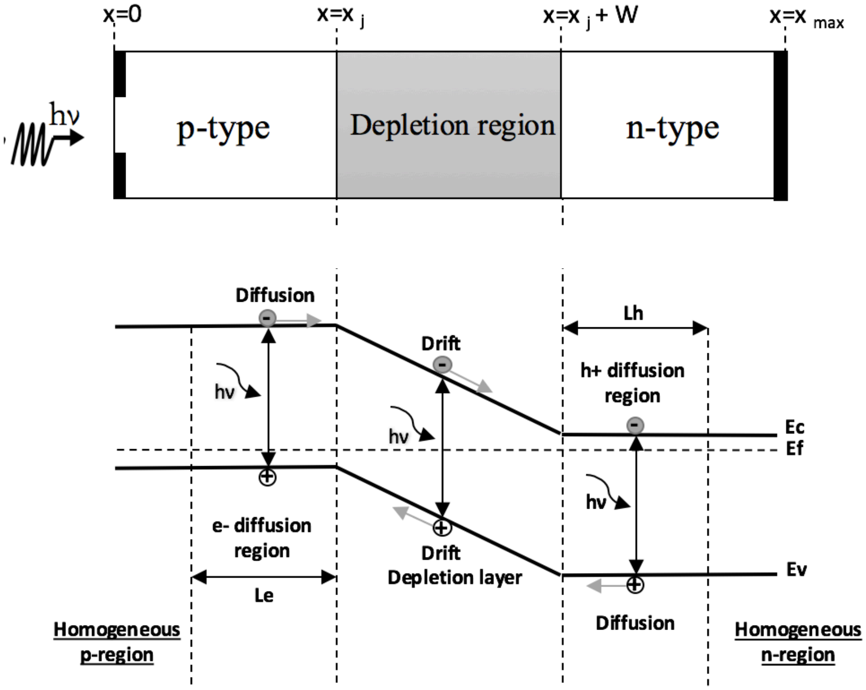

Figure 2.3: Schematic of a *pn* junction (top), and corresponding energy-band diagram (bottom) showing the carriers diffusion and drift in the quasi-neutral *p*- and *n*- regions toward the depletion region, where they are swept across by the electric field.

Fig. 2.4, which shows a schematic representation of a *pn* diode and its energy band diagram. Light absorption in the semiconductor produces electron-hole pairs, those in the depletion region or within a diffusion length of it will drift across the depletion region because of the electric field and lead to the current in the external circuit.

Under steady state conditions, Hovel presents the solution to the transport equation under optical illumination. The generation function associated with incident photons on the top surface is given by [55]

$$g(\lambda) = \alpha(\lambda)\Phi(\lambda)[1 - R(\lambda)]exp(-\alpha(\lambda)x) \tag{2.60}$$

where $\alpha(\lambda)$ is the absorption coefficient of the material, $\Phi(\lambda)$ is the number of the incident photons per unit of area per second per unit bandwidth, and the $R(\lambda)$ is the power reflectivity.

For the quasi-neutral p-region,and the quasi-neutral n-region, the transport equation can be written as

$$D_p\frac{\partial^2(\delta n)}{\partial x^2}+\alpha_p\Phi(1-R)\exp(-\alpha_p x)-\frac{\delta n}{\tau_n}=0, \tag{2.61}$$

and

$$D_p\frac{\partial^2(\delta p)}{\partial x^2}+\alpha_n\Phi(1-R)\exp(-\alpha_p x_j- \alpha_d W-\alpha_n(x-x_j-W))-\frac{\delta p}{\tau_p}=0, \tag{2.62}$$

respectively. Here, α_n is the absorption coefficients of the n-region and α_p is the absorption coefficients of the p-region. The general solution for these equations is

$$\partial n(\partial p)=Acosh(\frac{x}{L_{n(p)}})+Bsinh(\frac{x}{L_{n(p)}})- \frac{\alpha\Phi(1-R)\tau_{n(p)}}{(\alpha^2L_{n(p)}^2-1)}\exp(-\alpha x). \tag{2.63}$$

Where L_n and L_p are the diffusion length of minority carriers in p- and n-regions, respectively, and $L=\sqrt{D\tau}$. There are two boundary conditions for each region that can be written as

$$\begin{cases} D_p\frac{\delta(p_n-p_{n0})}{\delta x}=S_p(p_n-p_{n0}),[x=0] \\ p_n-p_{n0}=0,[x=x_j] \end{cases} \tag{2.64}$$

and

$$\begin{cases} D_n\frac{\delta(n_p-n_{p0})}{\delta x}=S_n(n_p-n_{p0}),[x=0] \\ n_p-n_{p0}=0,[x=x_j+W] \end{cases} \tag{2.65}$$

Based on these two boundary conditions, the hole and electron density can be obtained and used to calculate the diffusion photocurrent densities in the quasi-neutral n- and p-regions. These diffusion current densities in addition to the drift current density generated within the depletion region give the total EQE

$$QE = \frac{1}{q\Phi}(J_{ph-n} + J_{ph-SCR} + J_{ph-p}) = QE_n + QE_{SCR} + QE_p. \quad (2.66)$$

The total QE includes the effect of three regions of the space charge region (QE_{SCR}), the quasi-neutral n-region (QE_n), and the quasi-neutral p-region (QE_p) [57]. The QE for each region is obtained from the following expressions. First, for the depletion region, in case of p/n diode,

$$QE_{SCR} = (1-R)\exp \alpha_p x_j [1 - \exp -\alpha_d W] \quad (2.67)$$

where R is the reflectivity at the air/surface interface, and W is the depletion region width. In the case of n/p diode, α_p will be replaced with α_n. The electric field is assumed to be high enough in the depletion region so that the photo-excited carriers are extracted before they can recombine. As a result, the internal QE is assumed to be equal to the number of photons absorbed per second. The EQE for the n- and p-regions can be obtained as

$$QE_n = (1-R)\frac{\alpha_n L_p}{\alpha_n^2 L_p^2 - 1}$$
$$[\frac{\alpha_n L_p + L_p \frac{S_p}{D_p} - \exp(-\alpha_n x_j)[L_p \frac{S_p}{D_p} cosh(\frac{x_j}{L_p}) + sinh(\frac{x_j}{L_p})]}{[L_p \frac{S_p}{D_p} sinh(\frac{x_j}{L_p}) + cohs(\frac{x_j}{L_p})]} - \alpha_n L_p \exp(-\alpha_n x_j)], \quad (2.68)$$

and,

$$QE_p = (1-R)\frac{\alpha_p L_n}{\alpha_p^2 L_n^2 - 1}\exp(-\alpha_n x_j + \alpha_p W)$$
$$[-\frac{L_n \frac{S_n}{D_n}[cosh(\frac{x'}{L_n})] + \alpha_p L_n \exp(-\alpha_p x') + sinh(\frac{x'}{L_n})]}{[L_n \frac{S_n}{D_n} sinh(\frac{x'}{L_n}) + cohs(\frac{x'}{L_n})]} + \alpha_n L_p], \quad (2.69)$$

where x_j is the thickness of p-region, x' is the thickness of the n-region, and $\gamma(= SL/D)$ is the surface recombination velocity coefficients.

In the Hovel expressions, Eqs. (2.67,2.68,2.69), the important factors in determining the QE are the absorption coefficient, the background concentration, and the minority-carrier diffusion length. So, by fitting the experimentally measured QE data to this analytical model, the minority diffusion length can be extracted if the absorption coefficients and the background doping levels are known in prior[57, 30, 32]. Usually, surface recombination velocity (S) is assumed to be zero since it does not change the shape of the curve. However, it can affect the absolute magnitudes when the junction depth of the diode and the effective minority carrier diffusion length become comparable [57]. With this assumption, the results should be considered as a lower bound on diffusion length [30]. Other methods, such as Electron-Beam Induced-Current ($EBIC$) can be used to extract surface recombination velocity and diffusion length simultaneously, and to verify the results of this model.

2.5 Chapter Summary

In this chapter, a summary of the non-equilibrium carrier dynamics in semiconductors is presented. The basic principles of carrier transport, transport characteristics, and the miniband conduction are discussed. Furthermore, we have reviewed the current-voltage characteristics including the dark current mechanism, and finally, the quantum efficiency modeling as effective ways to extract the diffusion length from the experimental external quantum efficiency have been discussed. The analytical expressions presented in this chapter for the calculation of the carrier lifetime, dark current and the QE have been used in this work to extract various unknown properties as the fitting parameters from the experimental data.

Chapter 3

Electron Beam-Induced Current Technique

Transport in T2SLs has been investigated theoretically and experimentally using various optical and electrical techniques. The techniques employed to study transport in superlattices can be categorized further to drift and diffusion methods, including, but not limited to, magneto-transport, electron-beam-induced current($EBIC$), ultrafast optical technique, and spectral quantum efficiency measurement. Among these methods, the scanning electron microscope (SEM) in the electron-beam-induced-current ($EBIC$) mode has proven to be a valuable tool for characterizing the transport properties of semiconductor materials. One of the main advantages of $EBIC$ is to use the extremely small electron-beam spot size in SEM to spatially resolve information of material parameters in the active device.

In this dissertation, $EBIC$ was successfully used to investigate the vertical electron diffusion in MWIR InAs/GaSb T2SLs. In this chapter, the basic principle of $EBIC$ and theoretical and experimental considerations to apply it to semiconductor superlattices are reviewed.

3.1 Basic Principles

One of the earliest reports on $EBIC$ is by Everhart et al. who also coined the term $EBIC$,[58] in which the application of $EBIC$ for estimating the minority diffusion length has been demonstrated. In $EBIC$, a beam of high-energy electrons is scanned across a sample containing a *pn* junction or a Schottky junction and the resultant current is collected. The beam generates charge carriers through inelastic collisions with the crystal's lattice. The electron-hole pairs diffuse to the junction where are then swept across the depletion region and collected externally through the contacts and measured by a sensitive current amplifier [59]. Only the minority carriers contribute to this current. The result is a spatially resolved map of the sample's current, and when accompanied by analytical models,[59, 60, 61] it can be used to determine various transport properties.

General aspects of $EBIC$ and its application in defect analysis, grain boundary recombination and material characterization have been described and reviewed by various groups such as Honoka et al.,[62] and will only be summarized here. In the section, the theoretical and experimental background of $EBIC$ and its application in type-II superlattices have been discussed.

There are two configurations to perform $EBIC$ characterization (Fig.3.1): 'Normal collector geometry' shown in Fig. 3.1(a), in which the plane of the collecting Schottky or *pn* junction is perpendicular to the irradiated surface; and "planar-collector geometry" shown in Fig. 3.1(b), in which the collecting junction lies in the plane of the irradiated surface itself. Different analytical models have been proposed for either of these configurations to extract properties from experimental $EBIC$ data, including the minority carrier diffusion lengths, lifetimes, and surface recombination velocities. Since we are interested in the vertical transport characteristics of type-II superlattices, we will focus on the normal collector geometry, hereafter.

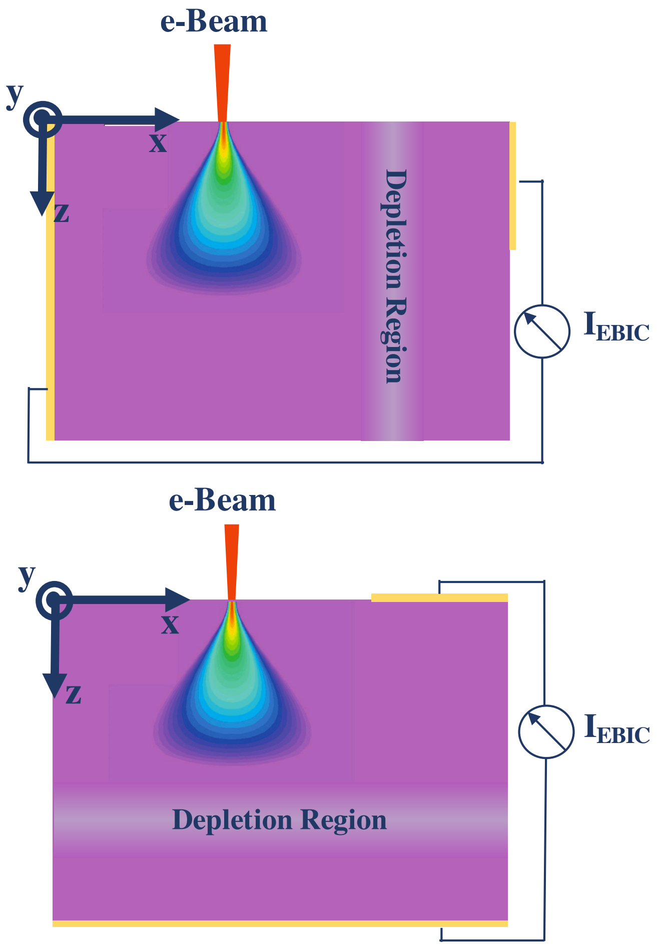

Figure 3.1: Schematic of the experimental set-up for *EBIC* characterization. (top) normal-collector geometry (bottom) planar-collector geometry.

3.2 Theoretical Model

The theoretical analysis can be performed by numerical simulation[67] or analytically solving the diffusion equation under simplifying assumptions [65, 60, 61, 59]. Various models have been presented which provide an acceptable first-order prediction of

Table 3.1: Summary of the models proposed for $EBIC$.

Model	Method	Assumptions	e-beam Source
Roosbroeck[63]	Green's formalism	(i)e-beam should be further than 2× Diffusion length (L) from both the rear contact and the junction region (ii)Semi-infinite semiconductor Surface Recombination Velocity (S): arbitrary	Point source at the surface
Berz & Kuiken[64]	Bessel function expressions Method of mirror sources	Same as Roosbroeck's model [63] S at ohmic rear surface: infinity S: Arbitrary Spherical Generation volume	Point source
Donolato[65, 60]	Green's reciprocity theorem and Fourier transforms	(i)e-beam's distance from the junction should be greater than the extension of generation volume (ii)Ohmic rear surface Includes extended generation volumes (iii)S: finite Spherical /pear-shaped Generation Volume	Gaussian source
Luke & von Roos[66]	Following Donolato[65]	(i)Inclusion of estimates for back-surface recombination velocities (ii)S: arbitrary	Gaussian source
Bonard & Ganire[59]	Following Donolato[60]	(i)Includes the generation within the SCR (Space Charge Region) and on both sides of the junction (ii)Neglects carrier recombination in backside interfaces, (iii)Includes S at the top(cleaved) surface (iv)It assumes SCR is perfect which is not in the case of the variation of charge collection due to the surface recombination, SRH,...	Gaussian source

$EBIC$ data and are shown in Table 3.1. These simplified models are for the case of simple pn junction and need to be modified to be adequate for devices with more complicated structures. Here, we review the most widely-used model proposed by Bonard and Ganire [59].

3.2.1 Bonard Model

Bonard and Ganire's model, which will be referred to as Bonard's model in this text, can be considered as the generalization form of an earlier model by Donolato [60]. Bonard's model accounts for the contribution of all three regions of a pn junction,

i.e., the n-type region, the depletion region, and the p-type region, for the case of the extended source. There are several assumptions in Bonard model:
(i) all generated charge in the depletion region is collected before recombining;
(ii) the transport properties are spatially invariant over the region of interest; and
(iii) low-level injection conditions are met.

Furthermore, Bonard's model does not account for carrier recombination at any surface other than where the electron beam impinges. The listed assumptions represent an ideal scenario that is not always realized. All charge is collected from the depletion region is only valid if the recombination lifetime is larger than or equal to the transit time of the carriers. Also, in realistic circumstances, the physical parameters do change spatially and lead to non-uniform charge collection resulting in contrast in the $EBIC$ image. Lastly, the low-level condition does not always apply. The value of the diffusion length L which is derived from the variation of the current with distance from the space-charge region is different at low and high injection. [64] Also, the carriers generated by the beam screen each other, and the reciprocity theorem solution to the diffusion equation,[60] which is the basis of the analytical solution for the drift-diffusion equation as implemented by Donolato,[60] is no longer valid. Thus, careful sample design, and measurement conditions, in terms of beam current and voltage, and observation of the experimental variations of diffusion length or lifetime with beam current and voltage are required. These assumptions and the requirements to fulfill them are not limited to the application of Bonard's model and may apply as well on the other models proposed to interpret the $EBIC$ data.

Under low-level injection, carriers will undergo diffusion-based motion. The distribution of non-equilibrium minority carriers, in the absence of an external electric field, assuming p-type material and steady-state condition, can be expressed in 3-D as

$$D_n \nabla^2 \delta n(x, y, z) + g(x, y, z) - \frac{\delta n}{\tau_{n0}} = 0, \tag{3.1}$$

where $g(x, y, z)$ is the generation rate. A solution to Eq. (3.1) can be deduced using appropriate boundary conditions. The two important boundary conditions are defined by:
(i) a perfect collector condition at a junction edge ($\delta n(x, y, z) = 0$ at $x = 0$), and
(ii) the surface recombination velocity S (with the dimension of $cm - s^{-1}$) at the material-vacuum interface ($\frac{\partial}{\partial z}\delta n(x, y, z)|_{z=0} = \frac{S}{D}\delta n(x, y, z)|_{z=0}$).

The electron-beam-induced current, $I_{EBIC}(x)$, can then obtained by solving Eq. (3.1) using the Green's reciprocity theorem, as implemented by Donolato [60].

The translational symmetry along y-direction reduces the problem to a *2-D* configuration on xz plane (see Fig. 3.1). The charge collection efficiency ($\eta(x)$), defined as the electron-beam induced-signal based on the electron beam position, $I_{EBIC}(x)$, normalized to the total number of generated electron-hole pairs, G_0, which can be obtained via the convolution of two terms: the generation function $h(x, z)$, and the probability of collection $\Phi(x, z)$, as follows

$$\eta(x) = \int_{-\infty}^{+\infty} dx' \int_{0}^{+\infty} h(x' - x, z')\Phi(x', z')dz', \tag{3.2}$$

where the integral is over the generation volume, and z is the normal distance from the junction. Several relations have been developed to calculate $h(x, z)$, which depend on the knowledge of the electron distribution values and structural design of the device, and the SEM's settings, such as beam energy and beam spot size [68].

The generation function determines the number of the beam-induced electron-hole pairs per unit time relative to the beam incident point on the sample, projected onto the xz plane. The resultant spatial distribution of the minority carriers is dependent on the sample's composition, the beam energy, E_b, and the beam spot size. And can be defined as[59]

$$h(x, z) = \frac{1}{a}\exp(-\frac{x^2}{\sigma_x^2})z^2\exp(-\frac{z}{\sigma_z})dxdz, \tag{3.3}$$

where σ_x is the lateral electron range and σ_z is the depth electron range, which is dependent on the material and the beam parameters and have the unit of the micrometer. They are related to the electron beam energy as $\sigma_x = (0.05 + 0.0001 E_b^{2.78})^{0.5}$ and $\sigma_z = 0.02 + 0.003 E_b^{1.5}$.
Bonard's model capability to predict different parameters from $EBIC$ data is highly dependent on the accuracy of the spatial distribution of the generated carriers, and it does not account for the beam spot size. To simulate the motion of the carriers in the generation volume and evaluation of the distribution of generated carriers, a more reliable method based on the 'Monte Carlo' method has been utilized. The Monte Carlo SEM interaction simulator CASINO [69] has been the most widely used simulator to calculate the spatial distribution of electron-hole carriers generated due to the incidence of the electron beam on the material. Within the framework of the Monte Carlo technique, the exact trajectories of the randomly distributed particles are simulated by a series of scattering events that change the electron's direction of movement, and it might lead to producing the secondary electrons through inelastic collisions. After each incidence, the electrons with energies larger than the semiconductor's energy gap will create electron-hole pairs, which in turn generate new electron-hole pairs. Except for the part that goes for the ionizing the electron-hole pairs, the rest of the energy will be divided randomly between the primary charge carrier, the hole, and the electron. These steps are repeated until either the electron leaves the sample's boundaries or its energy is less than a predefined value (50 eV) and hence, is trapped inside. By assuming that the generation of electron-hole pairs is relative to the energy lost,[68] the results can be used to estimate the normalized distribution of the electron-hole pair. Unlike the proposed distribution function by Bonard, CASINO accounts for the electron beam spot size which leads to more realistic distribution and has been used widely along Bonard model for $EBIC$ simulation.

Once the normalized distribution of the electron-hole pairs is known, one can use the numerical results to extract the depth and lateral distribution lengths of the

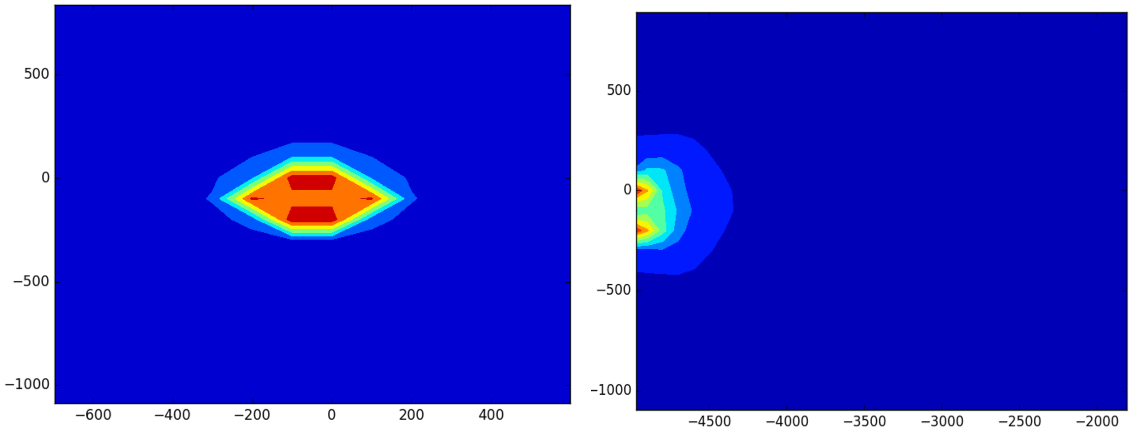

Figure 3.2: Monte carlo simulation of the sulerlattice absorber under illumination of a beam with 20 keV energy, 50 nm beam diameter, 1×10^6 electrons, and a grid of $100 \times 100 \times 100$, (left) projected on XY plane, (right) projected on XZ plane.

generation volume by fitting to Eq. (3.3). By applying separation of variables on $h(x, z)$, different components can be fitted to the Monte Carlo data along x- and z-directions ($h(x, z) = k(x).j(z)$) and σ_x and σ_z are evaluated as a function of beam spot size and beam energy[68].

Figure 3.2 shows the result of Monte Carlo simulation for a sample consisting of 5 μm region of InAs/GaSb type-II superlattice. The electron beam of 20 keV and the beam spot size of 50 nm have been used in this simulation.

The probability of collection is defined as the likelihood of a carrier being collected and contributes to the $EBIC$ current after diffusion. The charge collection probability can be found by solving the *2-D* reciprocal problem

$$\frac{\partial^2 \Phi}{\partial x^2} + \frac{\partial^2 \Phi}{\partial z^2} - L^{-2}\Phi = 0, \tag{3.4}$$

$$\Phi(x, z)|_{x=0} = 0, \tag{3.5}$$

$$\frac{\partial \Phi}{\partial z}|_{z=0} = \frac{S}{D}\Phi(x, 0). \tag{3.6}$$

By using the method of Eigen-function expansion, the solution for $\Phi(x,z)$ for an ideal collector ($\Phi = 1$ at the charge collecting surface or the depletion layer edge) can be found to be[59]

$$\Phi(x,z) = \frac{2S}{\pi D}\int_0^{\infty} \exp(-\mu(k,L)x)\frac{[cos(kz) + (S/kD)sin(kz)]}{k^2 + (S/D)^2}dk, \quad (3.7)$$

where $\mu(kL)$ is defined by

$$\mu(k,L) = \sqrt{k^2 + \frac{1}{L^2}} \quad (3.8)$$

And S is the surface recombination velocity, D is the diffusion constant, and k is a positive root of a transcendental equation,[60]

$$tan(kd) = \frac{s_0}{k}, \quad (3.9)$$

for which d is the sample thickness, and k becomes a vector of evenly spaced values for large d with spacing $\frac{\pi}{d}$ (to be replaced by dk in the final integral representation).

The charge collection efficiency $\eta(x)$ obtained from Eqs. (3.2, 3.3, and 3.7) have been simulated and shown in Fig. 3.3.

Bonard model considers the problem of a *2-D* case, assuming a Gaussian profile source. As mentioned before, this model's accuracy is highly dependent on the accurate shape of the distribution of electrons; besides, it does not account for the recombination at surfaces other than the top surface where *e*-beam impinges on the surface. An alternative and simpler approach has been proposed by Luke [61].

3.2.2 Luke Model

If the information about current collected in the depletion region is negligible, a more straightforward *1-D* approach proposed by Luke[61] for evaluation of the diffusion length is more favorable since it requires fewer input parameters, doesn't need extra

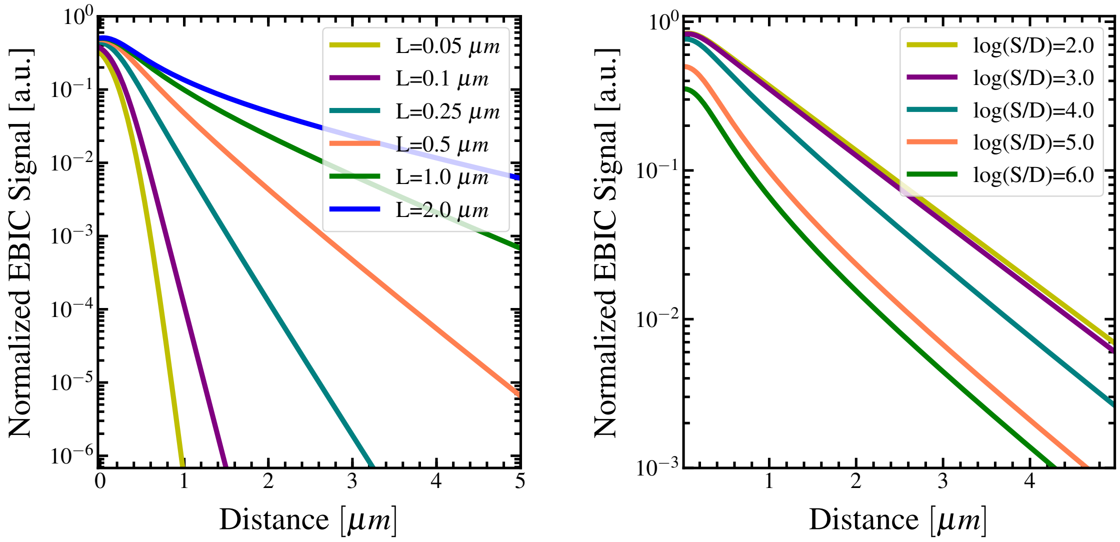

Figure 3.3: Simulated EBIC profiles based on Bonard approach for the collection efficiency: (left) with varying diffusion length L. The beam energy is set to $E_b = 5$ keV and the S/D ratio to $10^5 cm^{-1}$, (right) with varying S/D. The beam energy is set to $E_b = 5$ keV and the bulk diffusion length to $L = 1 \mu m$.

simulation steps in the assessment of distribution of electrons, and it accounts for the effect of backside surface recombination, as well. The latter is especially important for when L is larger than the layer's thickness.

Based on Luke's model, the normalized $EBIC$ current for the normal configuration can be calculated by the analytical relation of the form

$$I_N = \frac{cosh[\frac{d_1-x_1}{L}] + (\frac{LS_B}{D})sinh[\frac{d_1-x_1}{L}]}{cosh(\frac{d_1}{L}) + (\frac{LS_B}{D})sinh(\frac{d_1}{L})} - 2\eta_T \sum_{n=0}^{\infty} \frac{\delta_n}{\gamma_n^2(\gamma_n + \eta_T)}(1 - \frac{sin(2\delta_n)}{\delta_n})^{-1} \times \exp(-\frac{\gamma_n z_1}{d_1}) sin(\frac{\delta_n x_1}{d_1}), \quad (3.10)$$

where, δ_n are the roots of the equation $\delta_n + \eta_B tan\delta_n = 0$, $\gamma_n = [\delta_n^2 + (\frac{d_1}{L})^2]^{0.5}$, and $\eta_B = \frac{d_1 s_B}{D}$. z_1 represents the diffusion depth of the carrier in the sample and is related to the maximum range parameter.

Various models have described the maximum range of the generated charge distribution, among which the Kanaya and Okayama model has most closely recreated results from comprehensive Monte Carlo simulations, as expressed by[70]

$$R_{max} = (2.75 \times 10^{-2}) \frac{AE_b^{\frac{5}{3}}}{\rho Z^{\frac{8}{9}}} [\frac{1 + \frac{E_b}{2m_0c^2}}{1 + \frac{E_b}{m_0c^2}}]^{\frac{5}{3}} \tag{3.11}$$

where A is the atomic weight, ρ is the density in gcm^{-3}, E_b is in keV, and m_0c^2 is the rest mass of the electron ($511keV$). The diffusion depth can then be calculated from $\frac{Z_d}{R_{max}} = \frac{1}{1+\gamma}$, where $\gamma = 0.187Z^{3/2}$, with Z being the atomic number of the material.

The main disadvantage of above models is that they do not consider the relative changes of the $EBIC$ amplitude the electron-beam energy/current, and rely on normalizing the experimental and modeled data to perform analytical fitting. Most recently, Narae et al. have recently proposed an approach, based on a modification to Bonard's model, to improve the spatial resolution and retain information about the relative magnitude of the $EBIC$ signal as a function of incident beam energies and current, hence improving the uncertainty about extracted parameters [35]. In their approach, the generation volume is calculated using the Monte Carlo method, as implemented in CASINO code, and its result in addition to the analytical expressions for calculating the collection probability is used to obtain the collection efficiency at various electron-beam energies. The $EBIC$ signal then is scaled according to the electron-beam current at various beam energies, hence modeling both the changes in the $EBIC$ profile and its amplitude as well.

3.3 Experimental Considerations

A schematic of the experimental setup for $EBIC$ is shown in Fig.3.4. To operate an SEM in the $EBIC$ mode, a low input impedance current amplifier of adequate bandwidth and a means of collecting the beam induced-current are required. Care

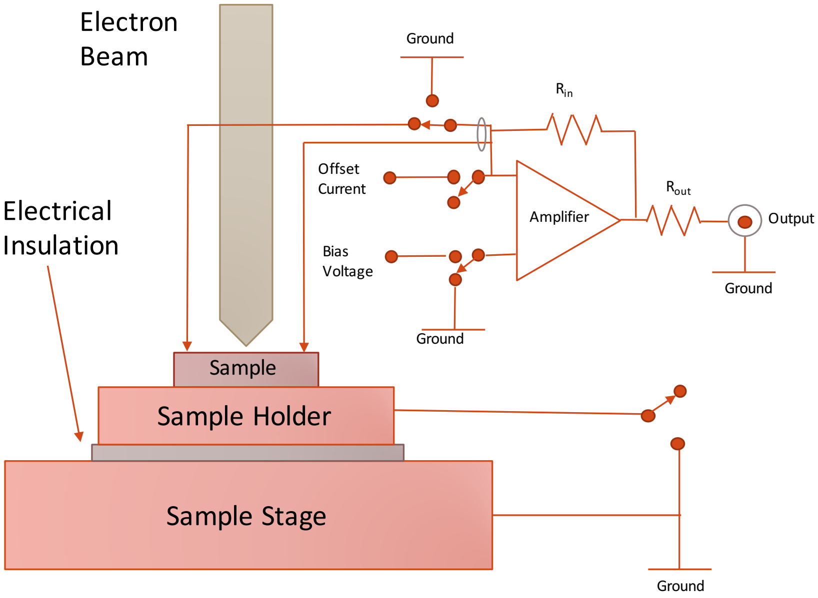

Figure 3.4: Schematic of the *EBIC* setup with external electrical connections to the current amplifier.

should be taken to eliminate the extraneous noise. Also, a junction of some sort, such as a *pn* junction, or a Schottky barrier is to be fabricated with thin, heavily doped contact regions for current collection. After the device fabrication, the sample needs to be cleaved to expose the sidewalls of one or more devices. This step might be facilitated by reducing the substrate's thickness before the cleaving. Using the diamond saw and polishing methods such as SiC sandpaper and an alumina colloidal solution have also been reported to expose the side wall of the devices [71].

The preparation of the sample for cross-sectional measurement alters the surface quality, which can influence the result by altering the *EBIC*'s contrast and invalidating the translational symmetry along y-axis [71]. The in-plane measurement of diffusion length, on the other hand, has shown to be larger than the cross-sectional method due to the absence of cleaved surface and the presence of the passivation in the former.

As mentioned in the previous section, in $EBIC$, the electron beam impinges on the sample and the current induced in the junction is collected for further processing. The minimum energy required to generate an electron-hole pair in a semiconductor is its band gap energy. However, the energy of the electrons in the beam typically is orders of magnitude larger than this minimum. For example, for MWIR type-II superlattices with a band gap of about $0.25eV$, the electron beam with an energy of $1KeV$ can produce approximately 4000 electron-hole pairs. As a result, a single high energy electron incident on the semiconductor generates a sufficient current with nearly three orders of magnitude amplification. Care must be taken to keep the excitation level below the background doping of the material to remain in the low-injection level regime.

In general, images of $I_{EBIC}(x, z, E_b)$ contain crucial information about the material and can be used for quantitative evaluation of diffusion length and surface velocity recombination ratio. If one measures the current as a function of distance (x, z) from the junction, the diffusion length can be extracted by fitting the experiment to the numerical model by iterative alteration of the assumed diffusion length. Since the results also depend on the magnitude of the ratio of surface recombination velocity to diffusion coefficient, which acts as a sink for the generated carriers at the cleaved surface, multiple $EBIC$ measurements with different beam energies (E_b) are required to extract both quantities. Higher beam energies not only give broader carrier generation distribution but also significantly higher carrier concentration generated due to the more in-depth the generation volume; so, more carriers are collected hence surface recombination velocity effect reduces [72]. If the result of independent lifetime characterization is used along with $EBIC$, diffusion coefficient and the carrier mobility can also be determined. The same way, an independent determination of D can be used with L to estimate the lifetime from $EBIC$ data, as well.

It should be mentioned that although $EBIC$ can use the extreme small electron-beam spot size in SEM to especially resolve information of material parameters in the active device, like any other electrical measurement, it requires the sample fabrication; and in the case of the normal incident geometry, the device needs to be cleaved and mounted vertically to expose the side-wall to the electron beam, which all can affect the material properties and the results that are being deduced from the measurement.

3.4 Chapter Summary

In this chapter, the general theoretical and experimental considerations for the Electron-Beam Induced Current ($EBIC$) technique for determining minority carrier diffusion length were summarized. Two $EBIC$ techniques to extract the diffusion length from line-scan data were reviewed; the model proposed Boanrd and Ganiers takes into account the current in each region of the pn junction, including the n-region, the p-region and the depletion region. However, it ignores the surface effect on the surfaces of the device except for the top surface where the electron beam impinges on the sample. On the other hand, the model proposed by Luke considers all the surfaces of the device and their associated surface recombination but only takes into account the current generated in the absorber region. The advantage of Luke's model is that it does not require an additional simulation to extract the generation volume extension, and it is relatively simpler to apply. Both methods involved fitting the line-scan data to an equation that contains a number of fitting parameters, one of which is diffusion length.

Chapter 4

Vertical Transport Study

As was mentioned in the proceeding chapters, drift and diffusion of excess electrons and holes, defined with ambipolar mobility (μ) or diffusion coefficient (D), are used to demonstrate the transport behavior of excess carriers generated in a semiconductor material. The carrier drifts mobility and diffusion coefficient are related through the Einstein relations as $D = (k_B T \mu)/q$, where k_B is Planck's constant, T is the temperature, q is the fundamental charge of an electron. This relation is valid under thermal equilibrium condition,[43] nevertheless it can be used as an approximation to extract the drift mobility. Diffusion is further dependent on an average distance that the relevant charge moves in the semiconductor before its recombination/extraction from it, hence is related to the minority carrier diffusion length (L_{mc}) and minority carrier lifetime (τ_{mc}). So, if one performs an independent lifetime characterization along with the diffusion length measurement, the diffusion coefficient and subsequently, the carrier mobility can be determined.

In this chapter, the outline of this approach for extracting the critical transport parameters in *nBp* MWIR detectors with a *p*-type 10 ML InAs/10 ML GaSb type-II superlattice is presented.

This chapter is organized as follows: Section 4.1 reviews the sample design used for this work. Section 4.2 presents the experimental approach used for measuring the minority carrier lifetime and the analytical modeling to study the limiting mechanism in the carrier recombination as a function of temperature and excess density. Section 4.3 focuses on the diffusion characteristics of the sample, using two different approaches. The experimental details of EBIC measurement and the semi-parametric modeling technique used for extracting the diffusion length are explained in subsection 4.3.1. The results of transport properties using QE modeling approach is discussed in subsection 4.3.2. Finally, section 4.4 summarizes critical observations and discusses the result of the time-of-flight technique to investigate the minority carrier drift mobility and drift velocity as a function of temperature.

4.1 Sample and Method

The *nBp* MWIR T2SL structure is grown by solid source molecular beam epitaxy on a tellurium-doped GaSb (001) epi-ready substrate. The epi-structure consists of a 250-nm non-intentionally doped GaSb buffer layer, followed by 1.5-μm thick *p*-doped ($5 \times 10^{17} cm^{-3}$) bottom contact layer and a 4-μm thick *p*-doped ($5 \times 10^{16} cm^{-3}$) absorber region, both composed of a 10 M InAs /10 ML GaSb T2SL with a band gap of 0.250 eV. A 250-nm thick lightly *n*-doped ($5 \times 10^{15} cm^{-3}$) hole-barrier with a band gap of 0.650 eV composed of a 12 ML InAs/ 6 ML AlSb T2SL was then grown, followed by a 200-nm thick *n*-doped ($5 \times 10^{17} cm^{-3}$) top contact layer with a band gap of 0.360 eV composed of a 5 ML InAs/ 4 ML GaSb T2SL. The grown structure with the band edge energy diagram is illustrated in Fig. 4.1. The epi-layer is then processed into variable area single-pixel devices using standard fabrication techniques. The shallow-etch scheme is incorporated during device fabrication such that the pixel mesas are defined down to the wide band gap material and not the

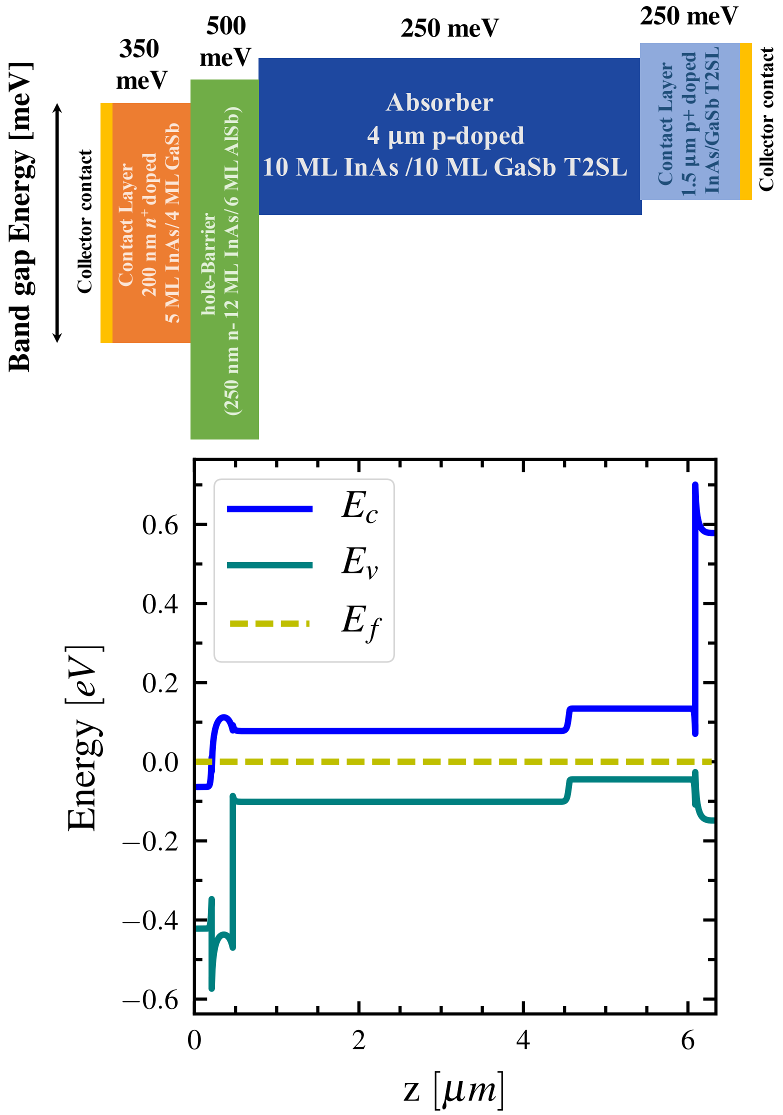

Figure 4.1: (Top) The *nBp* InAs/GaSb T2SL photodetector showing the relative thickness of the constituent layers (not drawn in scale). (Bottom) Band alignment of the structure calculated using NRL MULTIBAND® [73]

.

bottom contact layer. These pixels are then metalized, wire-bonded, and packaged for further electrical characterizations.

In order to estimate the transport along the growth direction, two approaches are used: the electron-beam-induced current ($EBIC$) method, and QE modeling technique. Each of these approaches helps measure the minority carrier diffusion length on the processed T2SL photodetector sample. Furthermore, the temperature and excess density dependence of the minority carrier lifetime is studied using sensitive time-resolved microwave reflectance measurement (TMR). Lastly, the minority carrier mobility in the growth direction is calculated using our results for L_{mc} and τ_{mc} and the Einstein relation, as a function of temperature.

The following sections present the theoretical and experimental details for each of these steps.

4.2 Carrier Lifetime Measurement

For the lifetime characterization, the unprocessed portion of the T2SL photodetector wafer was etched down to the absorber layer, to measure more accurate nonequilibrium carrier dynamics without the effect of the proceeding layers in the photodetector. The sample is mounted in a cryostat coupled with a temperature controller, while a 1535 nm pulsed laser with about 5 ns full-width-at-half-maximum pulse width, 2.5 kHz repetition rate, and beam spot size diameter of 0.1 cm is used to inject the excess carriers. The penetration depth at this wavelength in a similar T2SL (14 ML InAs/ 7 ML GaSb) is reported to be 3500 nm[74], which is used to extract the absorption coefficient to estimate the injected carrier density in the sample.

A MEMs-based modulator is used to attenuate the pulse power. At each excitation fluence, a packet of excess carriers is generated in the sample which alters the conductivity of the sample, and hence the microwave reflection from its front side. By probing the microwave signal that has been reflected from the surface as a function of time, we obtain the change in conductivity and consequently, the variation in the excited carrier density. The TMR decays are then amplified using a

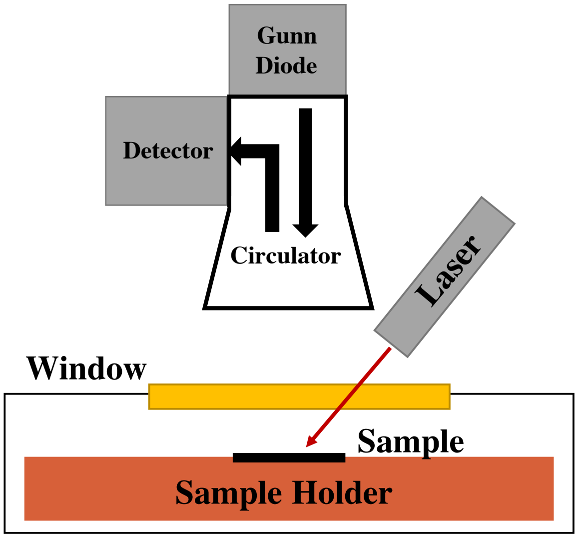

Figure 4.2: Time-resolved microwave reflectance measurement setup including the microwave apparatus, the excitation laser, and the cryostat.

preamplifier with 200 MHz bandwidth and detected using a high-resolution (12-bit) and high-speed digitizer. Schematic of the TMR setup is shown in Fig 4.2

TMR is then repeated at various laser fluences from 0.5 to 74 $\mu J cm^{-2}$, for temperatures between 20 K and room temperature. For brevity, we show the obtained results for a subset of injected carrier densities and temperatures in Fig.4.3. Results indicate an initial decay during the first two hundred nanoseconds following the generation of excess carriers. In addition, a secondary decay is observed for the temperature up to 200 K for the excitation level above $1.0 \times 10^{17} cm^{-3}$, and 150 K for the lower excitation levels, which is less distinctive as the incident pump fluence or the initial excess carrier is decreased. The former is associated with the recombination of carriers upon generation. Whereas the latter is not usually observed, and its origin is unknown to us. While further investigation is currently underway regarding this observation, it is hypothesized that this secondary decay might be due to the presence of defects, and is originated through the band-to-band to deep-level state recombination during this period.

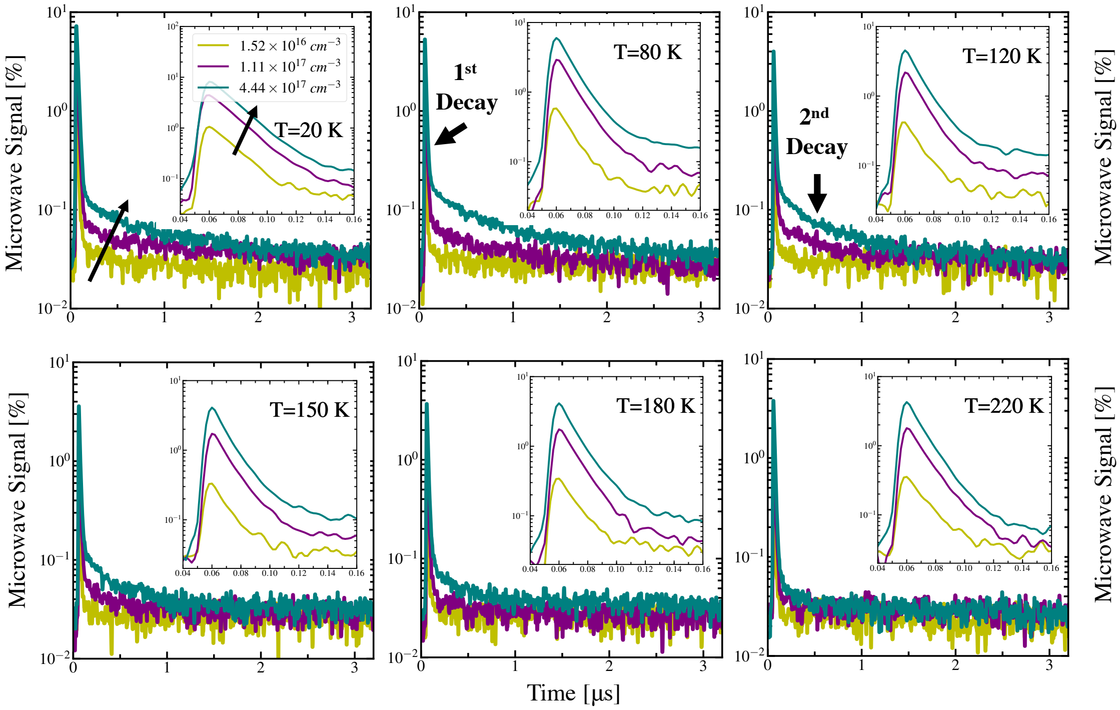

Figure 4.3: Time-resolved microwave reflectance decays of carrier recombination in the MWIR InAs/GaSb T2SL absorber. Data are shown for multiple different initial optically generated carrier densities and sample temperatures. The arrows in the two plots highlight the second decay observed for temperatures of 20 to 150K. The inset to the 20 K plot shows the fast initial decays which occur during the first few tens of nanoseconds at three excess carrier densities.

For the purpose of this work, we focus on the first decay to extract the minority carrier lifetime. Analytical modeling is then used to determine the experimental recombination lifetime. The intensity-dependent time-resolved microwave measurements results (Fig.4.3) are used to calculate the recombination rate per electron-hole pair as in [75]

$$R(n) = \frac{1}{n}\frac{dn}{dt} = \frac{1}{n}\frac{dn}{dS}\frac{dS}{dt}, \tag{4.1}$$

where S is the microwave signal in the TMR measurement. The results of $= 1/R(n)$ give the instantaneous lifetime as a function of excess carrier density at each tem-

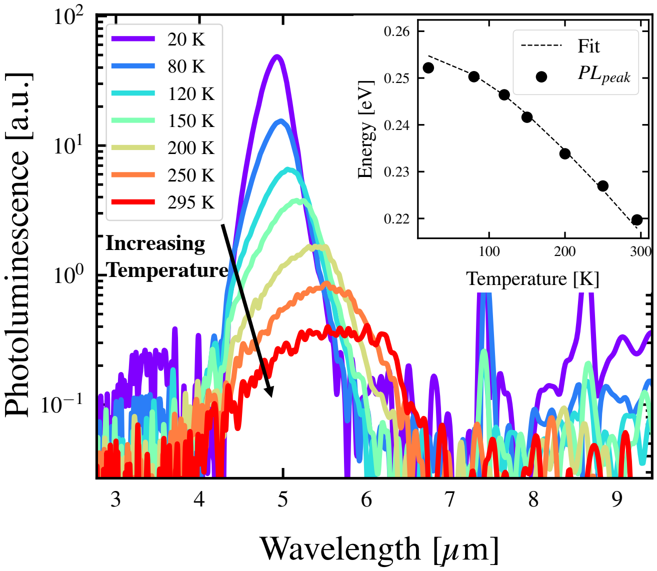

Figure 4.4: Measured photoluminescence spectra of the T2SL absorber, and the peak PL energy (inset-black circles) as a function of temperature. Dashed line shows the Varshni fit with parameters α=0.24 meV/K, and β=270 K.

perature, and when it is fit to the theoretical lifetime model, the minority carrier lifetime can be extracted as a fitting parameter for each temperature.

In this approach, the contribution of various recombination mechanisms, i.e., Shockley-Read-Hall (SRH), radiative, and Auger recombination, in the total lifetime is considered separately as a function of temperature and carrier density [76, 77].

The bulk recombination lifetime is determined by the Auger, radiative and SRH recombination mechanism as

$$\tau^{-1} = \tau_{srh}^{-1} + \tau_{rad}^{-1} + \tau_{auger}^{-1}. \tag{4.2}$$

Assuming a p-type material, i.e., $p_0 \gg n_0$, in the theory, a summary of the expressions used to calculate lifetime for the p-type absorber is presented. The common parameters used throughout this analysis are equilibrium electron (n_0) and hole(p_0) carrier concentrations, the energy gap (E_g), Boltzmann's constant (k_B), the temperature (T), and the effective electron (m_e), and hole (m_h) masses.

The photoluminescence (PL) spectra of the T2SL absorber was used to determine the energy gap as a function of temperature. Figure 4.4 shows measured PL spectra of the T2SL absorber for temperatures between 20 K to 300 K. The temperature dependence of the band gap, along with the Varshni fitting, is presented in the inset.

Experimental recombination lifetime ($= 1/R(n)$) data as a function of carrier density determined from the intensity-dependent time-resolved microwave measurements are fitted to the total lifetime using Eqs. (2.31, 2.36, 2.38, 4.2) as

$$\tau^{-1} = \frac{p_0 + \Delta n}{\tau_{p_0}(\Delta n) + \tau_{n_0}(p_0 + \Delta n)} + B(p_0 + \Delta n) + C_p(p_0 + \Delta n)^2 \quad (4.3)$$

Figure 4.5 shows the data (circles) for representative temperatures, compared with the overall fit (solid curve). We use the fitting parameters: τ_p, τ_n, B and C_p, for each of the contributing recombination process. The best fits are obtained for C_p as low as $1.0 \times 10^{-28} cm^6/s$ at 20 K, and as high as $4.0 \times 10^{-28} cm^6/s$ at 300 K. Previous studies have reported Auger coefficient equal to $1.0 \times 10^{-28} cm^6/s$ at 60 K[78], $1.3 \times 10^{-27} cm^6/s$ at 77 K [79] and $1.1 \times 10^{-27} cm^6/s$ at 77 K[80] in Ga-containing superlattices. Also, the radiative coefficient B is found to be $5.5 \times 10^{-10} cm^3/s$ and $1.6 \times 10^{-11} cm^3/s$ at 20 K and 300 K, respectively, which is close to previously obtained value of $1.4 \times 10^{-10} cm^3/s$ at 60 K for LWIR InAs/GaSb[78]. Furthermore, the fitting results indicate that τ_p is lower than τ_n for the temperatures above 50 K, both of which decrease gradually with temperature.

Based on Fig. 4.5, the low-injection portion of τ_{total} is mainly due to SRH recombination, while at higher injection regime ($> 1.0 \times 10^{17}\ cm^{-3}$), Auger and radiative recombination contributions are most significant, with radiative recombination being dominant below 50 K, and Auger recombination leading above 50 K.

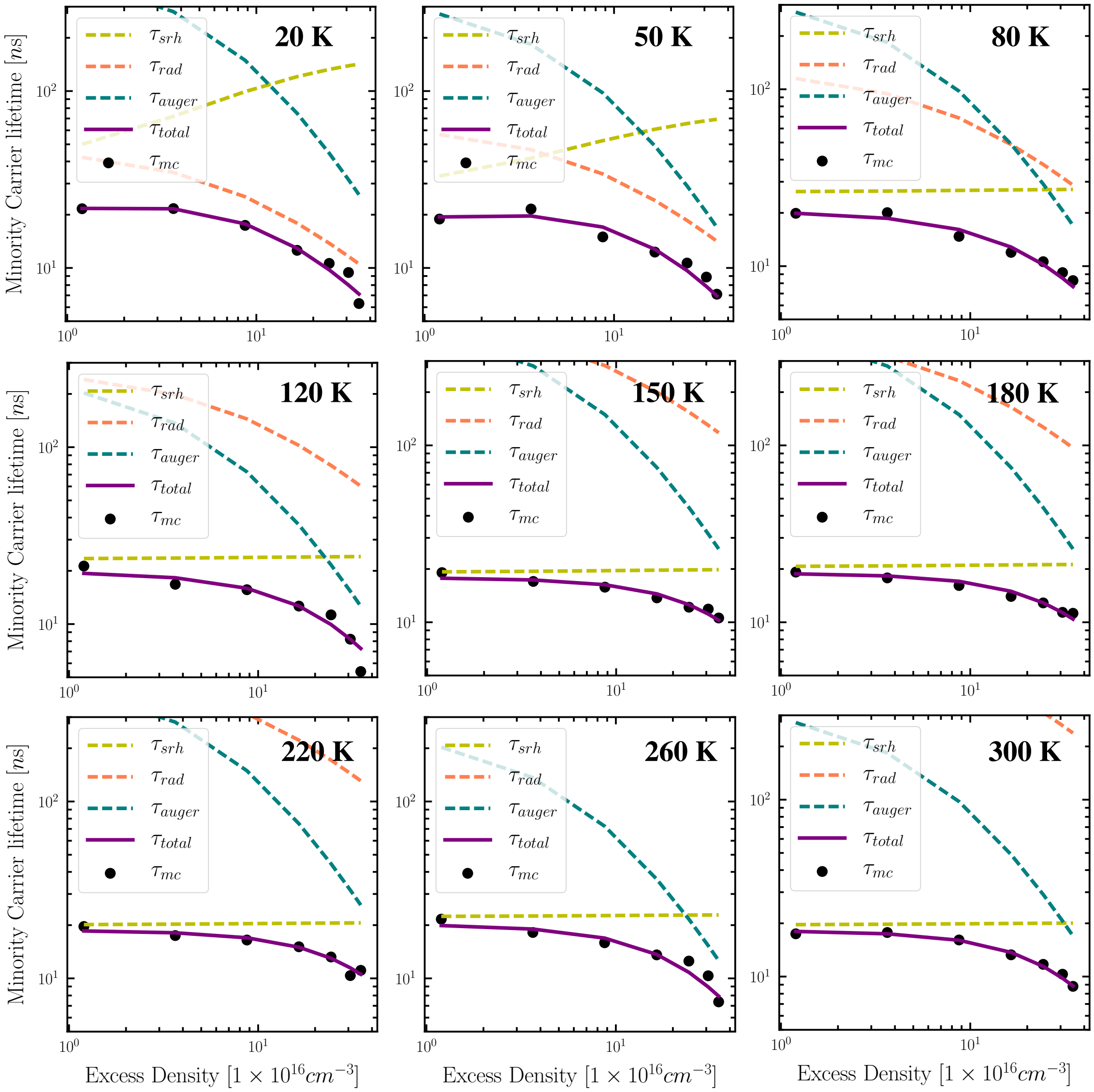

Figure 4.5: Measured minority carrier lifetime as a function of excess carrier density for a representative subset of temperatures, along with the calculated SRH, radiative, and Auger lifetime components. The total lifetime, shown as the solid purple curve, is the best fit for the measured lifetime to extract different fitting parameters. The radiative lifetime component at 260 K has a negligible effect on the total lifetime and is not shown.

For the analysis of the temperature-dependent lifetime, the extracted fitting parameters τ_{n0}, B, and C_p from above at each temperature are used to measure the minority carrier lifetime, under the assumption of ll-injection condition using Eqs. (2.34, 2.37, 2.39, 4.4)

$$\tau_{mc}^{-1} = \tau_{n0}^{-1} + Bp_0 + C_p p_0^2. \tag{4.4}$$

Having τ_{mc} values at each measured temperature, we fit the experimental data for temperatures ranging from 20 K to 300 K to the theory based on Eqs. (2.31, 2.36, 2.40, 4.2), using E_t, $\sigma_n N_t$, p_0, $|F_1F_2|$ and γ as fitting parameters. For simplicity, we assume σ_p and σ_n to be equal $(=\sigma)$, and use the effective masses that we obtained using NRL MULTIBAND® software:[73] $m_e = 0.034m_0$, and $m_h = 0.132m_0$.

The best fitting parameters are found to be E_t=34 meV, σN_t=1.25 cm^{-1}, p_0=$1\times 10^{17} cm^{-3}$, $|F_1F_2|$=0.18, and γ=4.3. The resultant doping concentration from the fitting is found to be 2× higher than the doping concentration used in the growth procedure for the absorber layer, which is $5\times 10^{16} cm^{-3}$. $|F_1F_2|$ is in the range that is previously reported for narrow-band gap materials[81].

Table 4.1: Extracted fit parameters for calculating the total minority carrier lifetime.

$E_t[meV]^1$	$\sigma N_t[cm^{-1}]$	$p_0[cm^{-3}]$	$\lvert F_1F_2\rvert$	γ
34	1.25	1×10^{17}	0.18	4.3

1. Defect levels are expressed relative to the valence band-edge.

Figure 4.6 shows the minority carrier lifetime as a function of temperature. The results indicate that lifetime is SRH-limited for the temperature range of 80 K to 150 K, while radiative recombination becomes more important and comparable to SRH contribution at temperatures from 20 K to 50 K, and the auger recombination is dominant above 200 K.

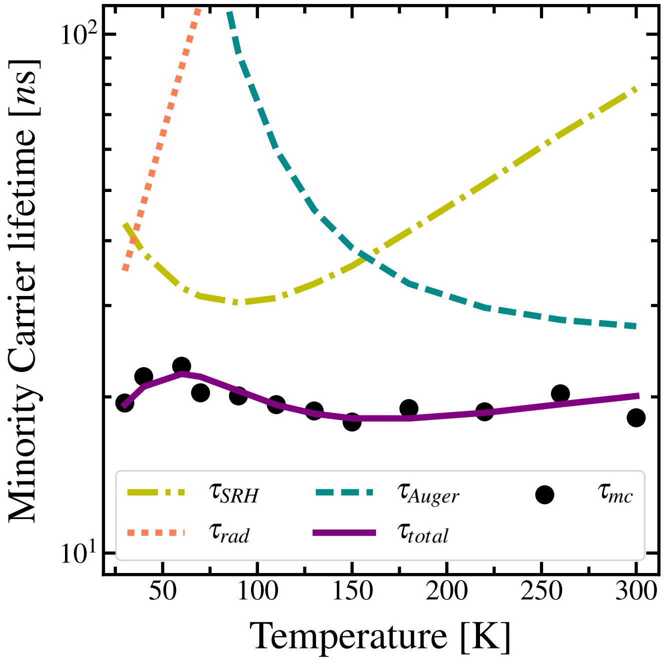

Figure 4.6: Temperature-dependent measured minority carrier lifetimes (black circles), compared to the low injection level SRH, radiative, and Auger lifetime components. The solid purple curve is the best fit for the total lifetime to extract different fitting parameters. The radiative lifetime was calculated using a photon recycling factor Φ of 1.8.

It is helpful to summarize the anticipated sources of error in our measurement which might pose some uncertainty on the estimated carrier density, and hence extracted lifetime: (i) There is a lateral gradient in the Gaussian beam profile of the laser illuminated on the sample, which may cause non-uniform injection, (ii) there are possible losses in the measurement system, for example, due to the cryostat windows, etc, and (iii) the effect of oxidation due to the air exposure needs to be investigated.

One needs to carefully consider these effects in determining the excess carrier density, in addition to the uncertainty in the fitting procedure of the TMR curves, in the analysis of the lifetime results. Nevertheless, the lifetime and the extracted fitting parameters in this work are in close agreement with the previously reported results[82, 83, 74].

Having the minority carrier lifetime as a function of temperature, minority carrier mobility versus temperature can be calculated, provided that the minority carrier diffusion length is known. For this purpose, in the following, two methods of the electron-beam induced-current or EBIC and QE modeling are utilized to estimate L_e, and consequently, we calculate the mobility.

4.3 Diffusion Characterization

4.3.1 EBIC

To study the transport characteristics along the growth direction with EBIC, 'Normal collector geometry' configuration was used, in which the plane of the collecting *pn* junction is perpendicular to the irradiated surface. For this purpose, the processed sample was cleaved to expose the sidewalls of one or more devices. This step was facilitated by reducing the substrate's thickness before the cleaving to achieve a smooth sidewall. The prepared devices were wire-bonded and mounted on a variable-temperature cold-stage cooled by liquid Nitrogen inside a JSM-IT100 SEM, such that the cross-section of the devices are exposed to the *e*-beam incidence.

As a result of the *e*-beam incidence on the device's side-wall at any distance away from the *pn* junction, a volume of electron-hole pairs is generated in the sample. Under low-level injection, carriers will undergo diffusion-based motion across the illuminated region toward the *pn* junction and contribute to the total current induced in the junction. The diffusion of minority electrons will dominate the current since the wide band gap hole-barrier layer is engineered to block the flow of majority holes

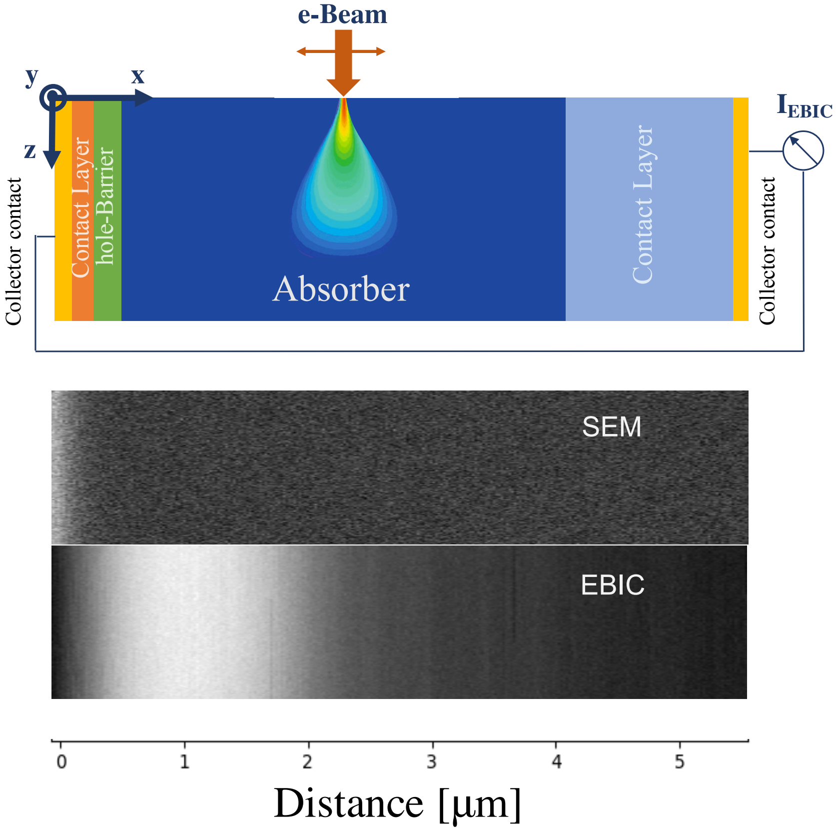

Figure 4.7: (Top) The structure of InAs/GaSb nBp T2SL and the generated electron-hole volume in the absorber region due to the e-beam impingement on the sample, (Bottom) The SEM and $EBIC$ images of the cross-section of the device under test at e-beam energy of 20 KeV and T=80K.

and let electrons flow unimpeded. The electron-induced current at various e-beam positions with respect to the junction ($I_{EBIC}(x)$) was collected using SR570 current-amplifier by repeating the measurement for points across the sidewall, at zero bias.

Figure 4.7(Top) illustrates the geometry of the sample in the EBIC setup, including the generation volume due to the e-beam incidence on the sample's absorber region. Figure 4.7(Bottom) shows the cross-sectional SEM and EBIC images from the side-wall of the device for 80 K.

Due to the high energy of the electrons in the beam, a single high energy electron incident on the semiconductor generates a sufficient current with several orders of magnitude amplification. Therefore, a careful design of experiment and measurement setup is required to consider the effect of the excitation level on the transport. Moreover, one should note the effect of the surface in the analysis of the EBIC data. The cleaved surface at the top, where the beam impinges on the sample, and the absorber-bottom contact interface (back surface) can contribute to the recombination. Surface recombination velocity acts as a sink for the generated carriers at these surfaces, and its effect, in addition to the influence of various external perturbations (for example, temperature) has to be taken into consideration in the analysis of EBIC results.

For this purpose, we investigate the dependence of EBIC on the surface recombination, by studying EBIC at varying e-beam energy and current. The images were collected at temperatures ranging from 80 K to 150 K, for e-beam energies of 10, 15, and 20 keV, and and the beam current of 1.5, 3.5, 8.5, and 35 pA. The e-beam current incident on the sample was measured using the Faraday cup. Figure 4.8 shows the resultant line-scan profile $I_{EBIC}(x)$ obtained for three temperatures for representative beam currents, denoted as 10%, 20%, 30% and 40% of the filament current in the SEM (Fig. 4.8[a-c]), and e-beam energies of 10, 15, and 20 keV (Fig. 4.8[d-f]), respectively.

As can be seen, the collected EBIC signal first rises steeply as the beam moves towards the depletion region, and reaches to its maximum in the depletion region due to the built-in field, then decays slowly as the e-beam moves further towards the substrate. The roll-offs on either side of the depletion region is relative to the diffusion and recombination characteristics of the minority carriers in each region. We found the n-region wholly depleted, and the depletion region extended to the p-region (absorber layer), changing with temperature and e-beam energies.

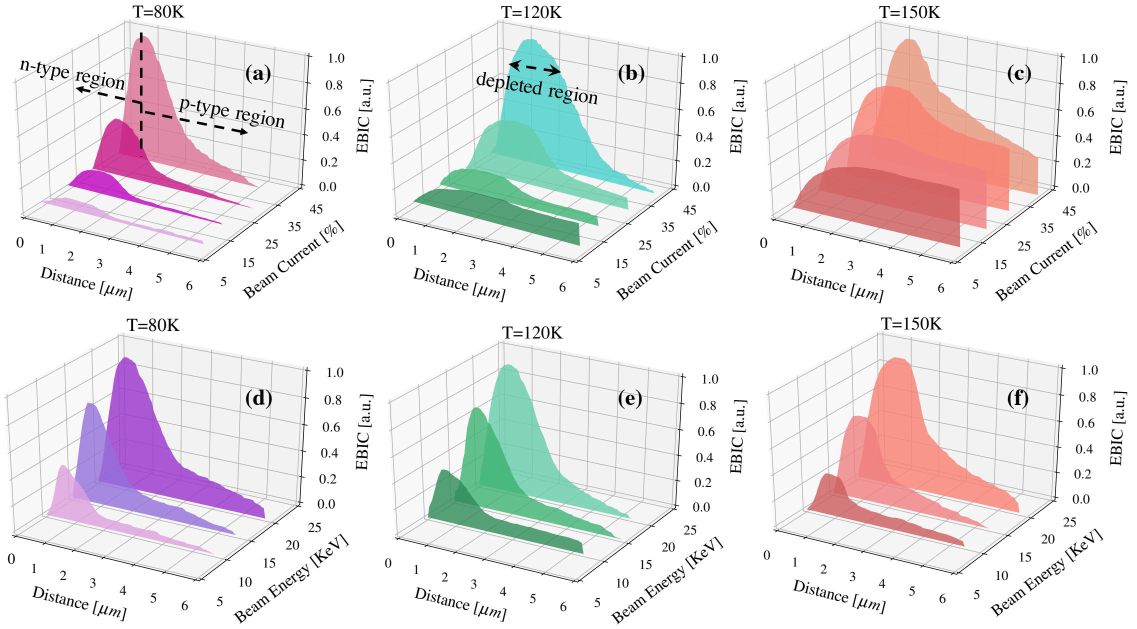

Figure 4.8: Experimental $EBIC$ data are shown for three representative temperatures of 80, 120 and 150 K with (top) varying beam current denoted as the percentage of the total filament current in the SEM, and (bottom) varying beam energy in keV. $EBIC$ intensities are normalized by signal peak maximum at the highest current(top) and accelerating voltage(bottom).

We note in Fig. 4.8[a-c], with increasing temperatures, the EBIC signal decays slower. Also, as the e-beam current increases at a fixed temperature the EBIC signal rises and the falling edge, associated with the absorber region becomes steeper. This observation is due to the characteristic of the surface at the top. Unlike bulk recombination, surface recombination depends not only on the density of surface states or interface traps but also on the charge state of surface states, i.e., depletion or accumulation [84]. We believe the cleaved sidewall of the device exposes the narrow band gap absorber region to oxide formation, and hence acts as an attracting potential for the generated excess carriers. By increasing the injection current, the enhanced density of excess carriers results in the saturation of the surface states; hence, the surface-induced attractive potential for minority carriers vanishes and surface recombination diminishes, and consequently, the signal due to the diffusion of the carriers rises. In contrast, the interface of the absorber and the bottom-contact (back surface) is accompanied with low surface recombination velocity in the case of our structure due to the higher doped bottom contact with respect to the absorber. The band offset at this interface builds a repulsive potential to minority carriers which inhibits further recombination.

To shed more light on the surface recombination current, we also investigate the effect of the beam energy in the SEM. At higher e-beam energies, minority carriers are generated deeper, and hence, are less likely to diffuse to the surface and recombine there. While at lower e-beam energies, the collection process is controlled by the collection probability at the surface of the sample, and the surface recombination velocity influences the current profile. As can be seen in Fig. 4.8[d-f], higher beam energies give not only broader carrier generation distribution but also significantly higher carrier concentrations, so more carriers are collected, and consequently, the signal increases.

We determine the minority carrier diffusion length for the electron current of 40% (35 pA) and the beam energies of 10, 15, and 20 keV. The value of the diffusion length can be derived from the variation of the current with distance from the space-charge region, for which we fit the semi-parametric model to the experimental results by iterative alteration of the assumed diffusion length and the ratio of surface recombination velocity to diffusion coefficient.

The basics of theoretical modeling required for EBIC has been reviewed in Chapter 3. Here, the Bonard's model was used for the nBp structure. The charge collection efficiency ($\eta(x)$) is $I_{EBIC}(x)$ which is normalized to the total number of generated electron-hole pairs, G_0, and can be calculated from the convolution of two terms: the probability of collection $\phi(x, z)$, defined as the likelihood of a carrier being collected and contributes to the $EBIC$ current after diffusion, and the generation function

$h(x, z)$ as[59]

$$\eta(x) = \int_{-\infty}^{+\infty} dx' \int_{0}^{+\infty} h(x' - x, z')\Phi(x', z')dz', \tag{4.5}$$

Due to the translational symmetry along the y-direction, the integral is calculated over the generation volume on the xz plane, where z is the normal distance from the junction.

The spatial distribution of the minority carriers can be defined as[59]

$$h(x, z) = \frac{1}{a}\exp(-\frac{x^2}{\sigma_x^2})Z^2\exp(-\frac{z}{\sigma_z})dxdz, \tag{4.6}$$

where σ_x is the lateral electron range and σ_z is the depth electron range, and are dependent on the material and the beam parameters.

For more accurate calculation of the generation distribution, we used the Monte Carlo SEM interaction simulator CASINO[85]. For this purpose, the normalized distribution of the electron-hole pairs from Monte Carlo simulation is used to extract σ_x and σ_z by fitting the numerical results to Eq. (4.6), as a function of beam spot size and beam energy [68].

As mentioned in Chapter 3, Bonard's model takes into account the current from all regions of a *pn* junction, i.e. *n*-region, *p*-region, and the depletion region. For the *nBp* structure: there are three main regions that contribute to the current: the *n*-type top contact, the *n*-type barrier layer, and the *p*-type absorber. Assuming the interface of the barrier-absorber coincides with the reference point of zero, we can summarize the relation for the probability of collection for each of these regions:

•**n^+-doped top contact**:

$$\Phi(x,z) = \frac{2S_h}{\pi D_h}\int_0^\infty e^{(d_j+x)\sqrt{k^2+\frac{1}{L_h^2}}}\frac{cos(kz)+\frac{1}{k}\frac{S_h}{D_h}sin(kz)}{k^2+(\frac{S_h}{D_h})^2}dk \qquad \text{for } x<-d_j \quad (4.7)$$

•n-doped barrier:

$$\Phi(x,z) = 1 \qquad \text{for } -d_j < x < 0 \quad (4.8)$$

•p-doped absorber:

$$\Phi(x,z) = \frac{2S_e}{\pi D_e}\int_0^\infty e^{-x\sqrt{k^2+\frac{1}{L_e^2}}}\frac{cos(kz)+\frac{1}{k}\frac{S_e}{D_e}sin(kz)}{k^2+(\frac{S_e}{D_e})^2}dk \qquad \text{for } 0<x \quad (4.9)$$

The resultant $\eta(x)$ then read as

$$\eta(x) = \frac{1}{\pi}\int_0^\infty [\frac{S_e}{D_e}v_e(k,x)+\frac{S_h}{D_h}v_h(k,-(x+d_j))]dk+0.5[erf(\frac{x+d_j}{\sigma_x}-erf(\frac{x}{\sigma_x}))] \quad (4.10)$$

with $v_{e,h}(k,x)$ defined as

$$\begin{aligned} v_{e,h}(k,x) &= \frac{1}{k^2+(\frac{S_{e,h}}{D_{e,h}})^2}\,\text{erfc}[\frac{\sigma_x}{2}(\mu(k,L_{e,h})-\frac{2x}{\sigma_1^2})] \\ &\times \exp[\frac{\sigma_x\mu(k,L_{e,h})}{2}]^2 \times \exp[-\mu(k,L_{e,h})x]\frac{1}{(1+k^2\sigma_z^2)^3} \\ &\times [1+3\frac{S_{e,h}\sigma_z}{D_{e,h}}-k^2(\frac{S_{e,h}\sigma_z^3}{D_{e,h}}+3\sigma_z^2)] \end{aligned} \quad (4.11)$$

The experimental *EBIC* data are fit to analytical expressions for the carrier collection efficiency (Eqs. 4.10, 4.11) to extract vertical minority carrier diffusion length, with diffusion length (L_e) and the ratio of surface recombination velocity to diffusion coefficient (S_e/D_e) used as fitting parameters.

Caution should be exercised in fitting theoretical curves to the experimental data since equally good agreement can often be obtained for several combinations of materials parameters. Here, we repeated our measurements several times for each e-beam

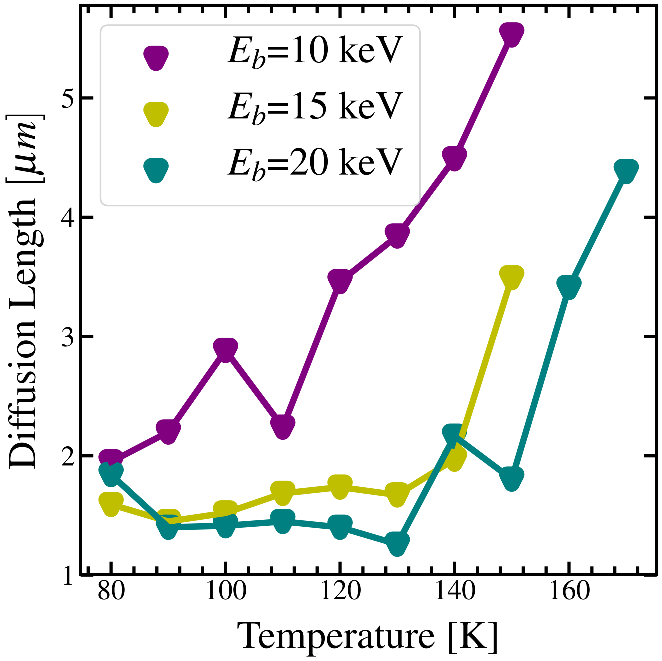

Figure 4.9: Extracted minority carrier diffusion lengths (L_e) for InAs/GaSb *nBp* MWIR sample as a function of temperature. The minority carrier diffusion lengths are extracted from the *EBIC* line scan profiles for *e*-beam energies of 10, 15, and 20 keV.

current and voltage. The results of L_e for variable *e*-beam current values at the accelerating voltage of 10, 15 and 20 keV are presented in Fig. 4.9.

4.3.1.1 Experimental Results and Discussion

Figure 4.9 shows the extracted minority carrier diffusion length for three *e*-beam energies of 10, 15, 20 keV at the beam current of 35.5 *pA*. Results for E_b=15 and 20 keV show similar trend with temperature, while 10 keV data is different and shows higher values for L_e. As mentioned above, the *e*-beam energy defines the depth of the generation volume in EBIC, and minority carriers generated closer to the surface at lower E_b, are more likely to contribute to the surface current rather than diffuse and be collected through the depletion region. From this perspective, we believe the behavior at 10 keV is due to the surface effect.

On the other hand, we see the values for diffusion length at 15 and 20 keV are very low, and have low-temperature dependency up to 140 K, after which they start to increase. For the temperature range of 80-140 K in this work, the diffusion length was found to be about 1.5μm, for the absorber thickness of 4 μm. It should be noted that the depleted region in the absorber is extended about 0.7 μm in this range of temperature, which makes the required travel distance less for the carrier. This might explain the high quantum efficiency reported previously on similar structure [12].

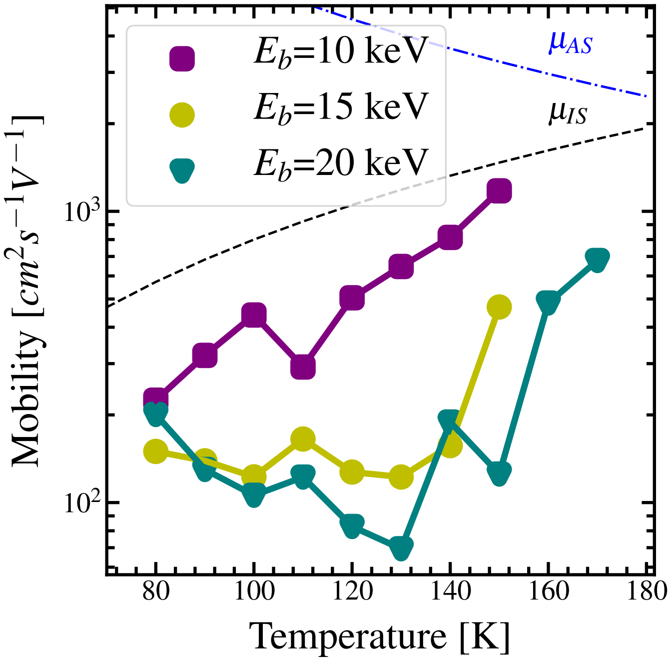

Figure 4.10: Vertical electron mobility for InAs/GaSb nBp MWIR sample as a function of temperature for e-beam energies of 10, 15, and 20 keV. Dashed lines show the acoustic phonon scattering μ_{AS}, and the ionized scattering μ_{IS} dependence on the temperature.

Having the minority diffusion length and the lifetime at each temperature, μ_e was calculated at various operating temperatures using the Einstein relation. Figure 4.10 shows the results of the minority mobility against temperature for three e-beam energies. Since the lifetime was found to have minor dependency on the temperature range of 80 K to 150 K, the general trend of μ_e follows the pattern of the extracted L_e with temperature, which was found to be independent of the temperature up to 140 K, for e-beam energies of 15 and 20 keV, and increasing linearly beyond that.

In order to understand the observed mobility trend, one needs to consider different limiting factors. In the semi-classical study of transport in superlattices, disorders such as structural and phonon-induced disorders are responsible in destroying the long-range coherence of the electron states, and as a result lead to localization through different scattering mechanisms, such as phonons-induced scattering, ionized impurity scattering, and interface roughness scattering (IRS).

Each of these scattering mechanisms has different temperature-dependency[43]: The impurity scattering is most effective at lower temperatures with $\sim T^{3/2}$ dependency on temperature, while at higher temperatures, phonon scattering dominates as a function of $\sim T^{-3/2}$. However, none of these scattering mechanisms can be accountable for the observed trend in the electron mobility data as shown in fig. 4.10. On the other hand, localization as a result of IRS can happen due to growth imperfections. Microscopic fluctuation of the composition of constituent layers, as well as interface roughness, can lead to spatially dependent structural disorders, and electron mobility degradation.[9] However, the effect of IRS tends to weakly increase with decreasing temperature [86].

The trend in the mobility can be explained separately for two temperature regions of 80-140 K (region 1), and 140 K above (region 2). For region 1, we believe the transport is limited by trap-assisted transport rather than miniband conduction, due to the presence of the deep-level states. In a perfectly periodic crystal, the charge density spreads uniformly throughout the crystal, and the only states are those described by Bloch waves[87]. While in the presence of localized imperfections, energy states appear within the forbidden gaps, the wave functions of which are localized in the vicinity of the impurity. The carriers that are bound to the impurity are not free to move anywhere in the crystal. The minority electron mobility is controlled by the extent to which they can be released from these bound impurity states[41]. In region 2, the increase in the mobility with the temperature can be associated with the carriers being set free from the impurity states, with an activation energy of 115 meV. A similar observation has been reported previously in n-type InAs/InAsSb T2SL structures[88], in which results show that above 120 K, the minority carrier hole transport occurs through minibands, while for lower temperatures, the holes are localized and transport is only due to phonon-assisted tunneling.

4.3.2 QE Modeling

Spectral external quantum efficiency (EQE) modeling can be used as an alternative method to extract the minority carrier diffusion length L_e of the same structure used above. By fitting the experimentally measured EQE data to the theoretically calculated QE based on the solution of the drift-diffusion equation, the diffusion length in the absorber layer can be estimated. With the result of this model and the lifetime measurement from TMR that described above, the diffusion coefficient and the mobility were calculated in the T2SL detector at various temperatures.

In the following, we first summarize our results of the absorption coefficient measurement, which we used to calculate the QE theoretically based on the procedure described in section 2.4. Then we present the experimental and simulated QE. Finally, we compare the obtained transport properties with the results of the EBIC measurements.

4.3.2.1 Absorption Coefficient Measurement

The knowledge of the wavelength dependence of the absorption coefficient ($\alpha(\lambda)$) is required to extract diffusion length from the spectral quantum efficiency model. In this work, the absorption coefficient was determined through IR transmission measurements using a Fourier transform infrared (FTIR) spectrometer. The T2SL epi-layers were etched off to different thicknesses on three separate pieces, in which the top contact, the hole-barrier, and the absorber were removed, respectively, to measure the transmission spectra of each layer separately. The samples were mounted side-by-side in the cryostat with ZnS windows and transmission spectra at 80K, 120K, and 150K were measured using reflective optics. The same sized apertures on each sample were used in the measurement to ensure the identical radiant flux for each sample. The result of the transmission at each layer was compared directly to the transmission of its underlying layers. The absorption coefficient for the absorber was then calculated using the model described in Reference [89], based on the measured transmission for the epi-layer (T) and the substrate (T_s). The same procedure was repeated for the top-contact, the hole-barrier.

For this purpose, the T2SL structures used for this work are treated as two-layer structures consisting of an epitaxial film (T2SL absorber) on top of a bulk substrate (GaSb). The incident light intensity is considered to be 1. In general, the reflection coefficient at an interface for normal incidence is given by[89]

$$R = \frac{(n_2 - n_1)^2}{(n_2 + n_1)^2}, \tag{4.12}$$

where n_1 and n_2 are the refractive indexes of the two media. Assuming the refractive index of T2SLs is close to that of GaSb substrate and has negligible wavelength dependence, the reflection coefficients at film/substrate are zero, and reflection at air/film, and substrate/air interfaces are equal to the same R. With these assumptions, the total transmission through the structure after multiple passes, T, can be found by adding the transmission components in each pass and expressed as[89]

$$T = \frac{(1-R)^2 e^{-\alpha t} e^{-\alpha_s d}}{1 - R^2 e^{-2\alpha t} e^{-2\alpha_s d}}, \tag{4.13}$$

where α, α_s, t, and d are the absorption coefficients and the thicknesses of the film and the substrate, respectively.

The calculation of T2SL absorption coefficient is a two-step process: First, the absorption coefficient of the substrate (α_s) is calculated using the experimentally measured transmission for the substrate (T_s) and Eq. 4.13 with t = 0.

$$X = \frac{(1-R)^2 - \sqrt{(1-R)^4 + (4T_s^2 R^2)}}{-2T_s R^2}, \tag{4.14}$$

where, $X = e^{-\alpha_s d}$.

Then, the absorption coefficient of the T2SL material (α) is calculated using the experimental transmission for the T2SL sample (T) and Eq. 4.13 with the known value of α_s

$$Y = \frac{(1-R)^2 X - \sqrt{(1-R)^4 X^2 + (4T^2 R^2 X^2)}}{-2T R^2 X^2}, \tag{4.15}$$

and $\alpha = -ln(Y)/t$. The values used for this calculations are R=0.32 and T=4 μm.

Figure 4.11 shows the result of the measured absorption coefficient of the absorber layer with the thickness of 4 m at 80K, 120K, and 150K, which increases slightly with temperature.

4.3.2.2 Experimental Results and Discussion

For quantum efficiency measurements, a standard setup consisting of a calibrated blackbody, narrow band filters (centered at 3.4 and 4.5 μm), a current pre-amplifier,

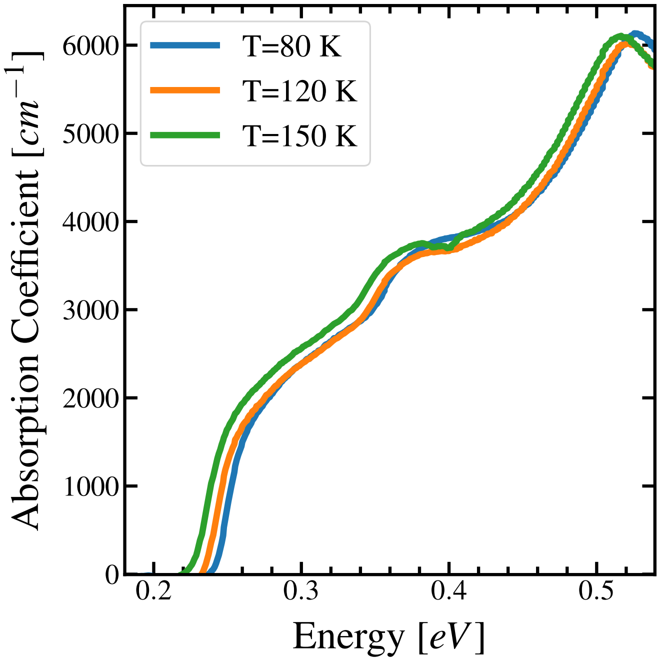

Figure 4.11: Absorption coefficient measured for the absorber layer w.r.t to the substrate under different operating temperatures.

and a lock-in amplifier is used. Measurements are performed using front-side illumination geometry with no anti-reflection coating. The results of quantum efficiency at 3.4 and 4.5 μm are used to calibrate the spectral photoresponse, which is obtained using a Fourier transform infrared (FTIR) spectrometer and is normalized to a reference detector's response.

Figure 4.12 shows the results of the quantum efficiency at 80K, 120K, and 150K under 200 mV applied bias, which is the turn-on bias at these temperatures. The inclusion of bias affects the simulated quantum efficiency only through changing the depletion region width which was taken into account in the simulation.

The fitting of the simulated and measured spectral quantum efficiency at various temperatures was done using the diffusion length as the fitting parameter. For this

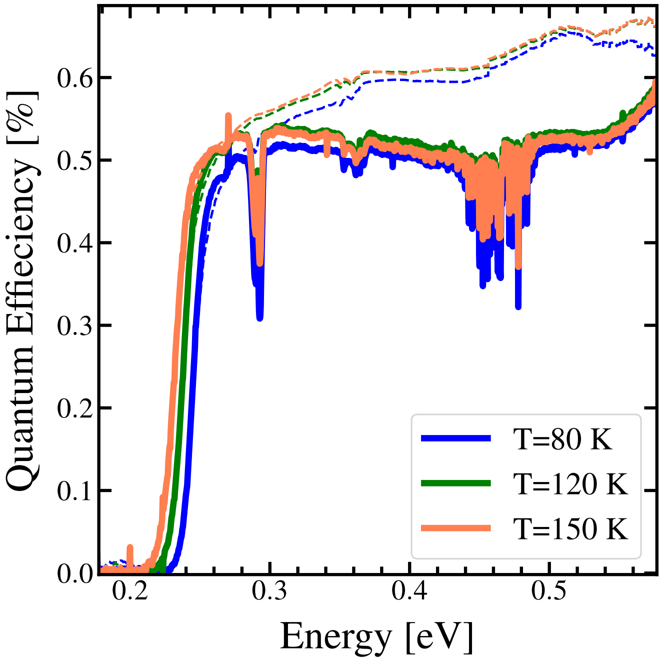

Figure 4.12: Comparison between experimental and calculated quantum efficiency spectra for the nBp photodetector at V=0.2V, for T=80, 120, and 150 K. The devices used for this measurement was 500 μm in size. The CO_2 absorption at 0.295 eV is visible in the experimental data.

purpose, the spectral area used for the fit was primarily around the band edge, where the absorber (p-region) has the most profound effect. It should be noted that the contribution of the QE_n and QE_{SCR} was neglected in the simulation since they are most effective at the higher energy regions of the quantum efficiency spectra.

Figure 4.12 also shows the comparison of the measured and simulated spectral quantum efficiency. The simulated quantum efficiency is in good agreement with the experimental results in the region near the band edge. The difference at higher energy indicates that the carriers excited by the incoming radiation have some loss due to absorption in the top contact region. Also, other factors might be responsible such as the error in the absorption measurement used in the model.

The diffusion lengths were estimated as the best fits between experimental and calculated quantum efficiency. Moreover, the diffusion coefficient was calculated using the diffusion length and lifetime at each temperature. Having the diffusion coefficients, also the mobility at each temperature was obtained using the Einstein relation. The lifetime data were used from TMR measurement, described earlier in Section 4.2. Table 4.2 summarizes the results of different parameters for several operating temperatures.

Table 4.2: A summary of different extracted transport properties from the analytical QE model for $V_{applied} = 0.2$ V

Temperature $[K]$	Diffusion Length $[\mu m]$	Diffusion Coefficient $[cm^2 s^{-1}]$	Mobility $[cm^2 V^{-1} s^{-1}]$	Lifetime $[ns]$
80	12	60	8695.6	24
120	11	55	5314.0	22
150	9	40.5	3130.4	20

Comparing the results of QE modeling on the diffusion characteristics with EBIC, it is obvious that the diffusion length estimated using the EBIC technique for the *p*-type sample is an order of magnitude lower. Since both of these methods validity are dependent on different assumptions, it would be impossible to make any meaningful comparison between the results obtained for these techniques without further investigation of the accuracy of the assumptions. Nevertheless, one hypothesize to investigate is that the discrepancy is due to the presence of undesirable recombination caused by a surface layer in the depletion region in the EBIC measurement. This surface layer can result in a significant error in the diffusion length estimation with respect to its actual values. In Bonard's model, the only surface taken into account is the top surface where the electron beam impinges on the sample. On the other hand, in the QE modeling, the surface recombination velocity is taken to be zero in the simulation. Both of these can lead to noticeable errors in the results. Furthermore, in both the EBIC and QE modeling, the collection efficiency in the depletion region is assumed to be one, which might not be the case in the experiment due to the presence of the surface damage or defects in the material. Therefore, the results should be treated with caution and confirmation with an alternative technique or a numerical model should be obtained.

4.4 Drift Characterization

The drift characteristics of semiconductor materials can be studied either by photocurrent measurement or time-of-flight (TOF) experiment. While the peak of the photocurrent signal as a function of applied bias can be used to investigate parameters such as drift velocity and mobility, the TOF approach can be used to determine the transport of the carriers in the semiconductor. In this chapter, the photocurrent-voltage method is discussed to investigate the field- and temperature-dependence of the drift characteristics in the *nBp* T2SL sample.

4.4.1 Photocurrent-Voltage Measurement

The photocurrent-voltage technique has been applied to study carrier transport through the *nBp* photodiode. Figure 4.13 shows the schematic of this sample. In this experiment, a narrow pulse is used to excite electron-hole pairs in the sample. The generated carriers are excited near the top surface of the *nBp* device. Due to the application of an electric field in reverse bias, the electrons will diffuse and recombine with majority holes as they drift along the absorber region and be collected at the contacts. Whereas, the flow of the holes is blocked by the inclusion of the hole-barrier in the superlattice structure. Hence, the photocurrent is mainly due to the motion of the electrons. In reverse bias, no carriers are injected into the absorber layer, and the carrier density can solely be controlled by photo-excitation.

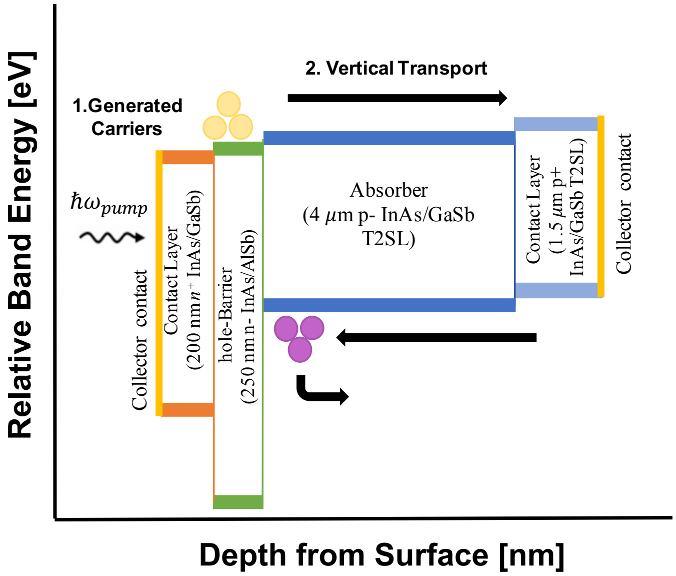

Figure 4.13: Schematic of the structure used for the photocurrent-voltage measurement.

In the experiments, a tunable pulsed optical parametric amplifier (TOPAS) is used with a pulse width of 200 fs at a repetition rate of 1000 Hz. The wavelength of the laser is fixed at 4.5 μm corresponding to a penetration depth of 4500 nm. The sample is mounted in an optical cryostat to vary the sample temperature between 77 and 300 K. A current pre-amplifier is used to amplify the signal and apply the external electric field F_{app}. The photocurrent is then detected with a Tektronix oscilloscope (TDS5204B, 500 MHz BW, 5GS/s) as a function of time and applied bias. The schematic of the experimental measurement set-up for these measurements is shown in Fig. 4.14.

The maximum of the photocurrent transient I_p is recorded as a function of the applied voltage. This allows us to obtain the drift velocity as a function of the applied

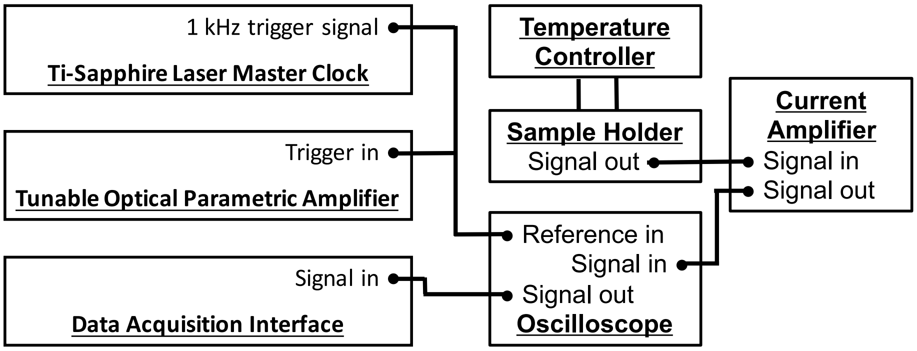

Figure 4.14: Schematic of the current-voltage measurement setup.

voltage (V_{app}) as

$$V_d(V_{app}) = \frac{L}{Q} I_p(V_{app}), \tag{4.16}$$

In which the photogenerated charge Q can be extracted as the integrated photocurrent signal, or calculated as

$$Q = \frac{qF_e\lambda}{hcL}[1 - e^{-\alpha L}], \tag{4.17}$$

where,

$$F_e = (1 - R_f)T_W \frac{P_e}{\pi w_e^2 R_r}. \tag{4.18}$$

Here, q is the electron charge, F_e is the incident fluence on the sample, λ is the wavelength of the laser, α is the absorption coefficient at the laser wavelength, R_f is the Fresnel reflection at the sample surface, T_w is the transmission of the cryostat window, P_e is the power of the laser, R_r is the repetition rate and w_e is the beam waist at sample surface.

The results of the peak of the photocurrent versus applied bias at various temperatures are shown for various laser power (Fig. 4.15). In this figure, the negative applied bias is associated with the reverse bias.

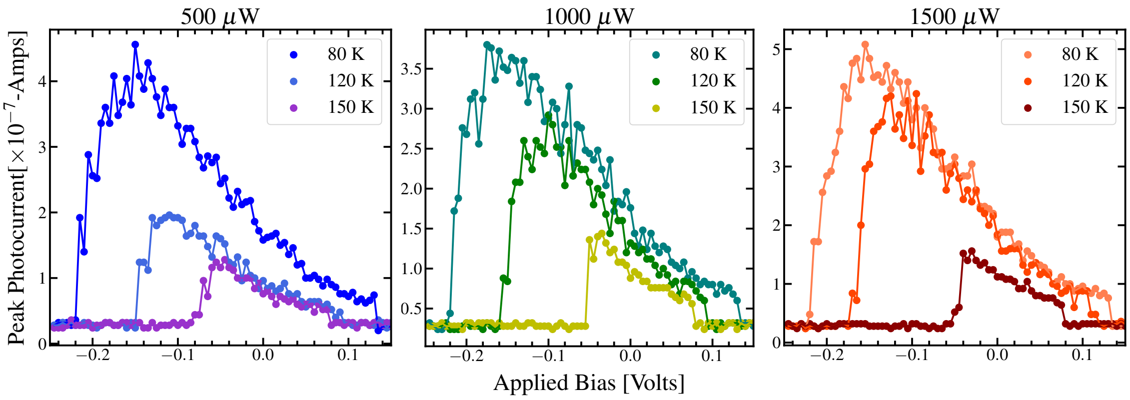

Figure 4.15: Peak photocurrent versus applied bias for various operating temperatures.

The linear regions in the plots are when the effective electric field F_{eff} is getting to zero. F_{eff} is a sum of the applied voltage V_{app} and the built-in potential of the diode V_{bi} as

$$F_{eff} = \frac{V_{app} + V_{bi}}{L}, \tag{4.19}$$

where L is the length of the diode. So, one can estimate the built-in potential by estimating V_{app} at which $F_{eff} = 0$. From this analysis, we find V_{bi} to a function of temperature.

Figure 4.17 shows the same results for various incident power at each temperature.

We hypothesize that the decrease in the photocurrent by increasing the voltage is due to the negative differential velocity (NDV) in the superlattice, i.e., the decrease of the electron mean velocity with increasing electric field beyond a critical field [23, 90]. While these results seem encouraging, further investigation is required to verify the origin of this observation.

The drift/diffusion of the electrons leads to a time-dependent photocurrent, which vanishes after the electrons reach the collectors. This transient signal is strongly dependent on the applied voltage, excitation energy, and the intensity of the light.

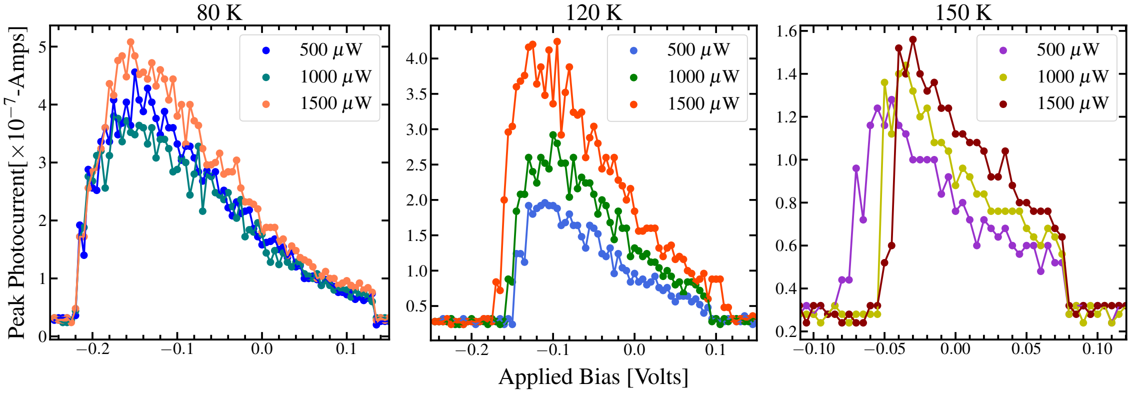

Figure 4.16: Peak photocurrent versus applied bias for various pump power.

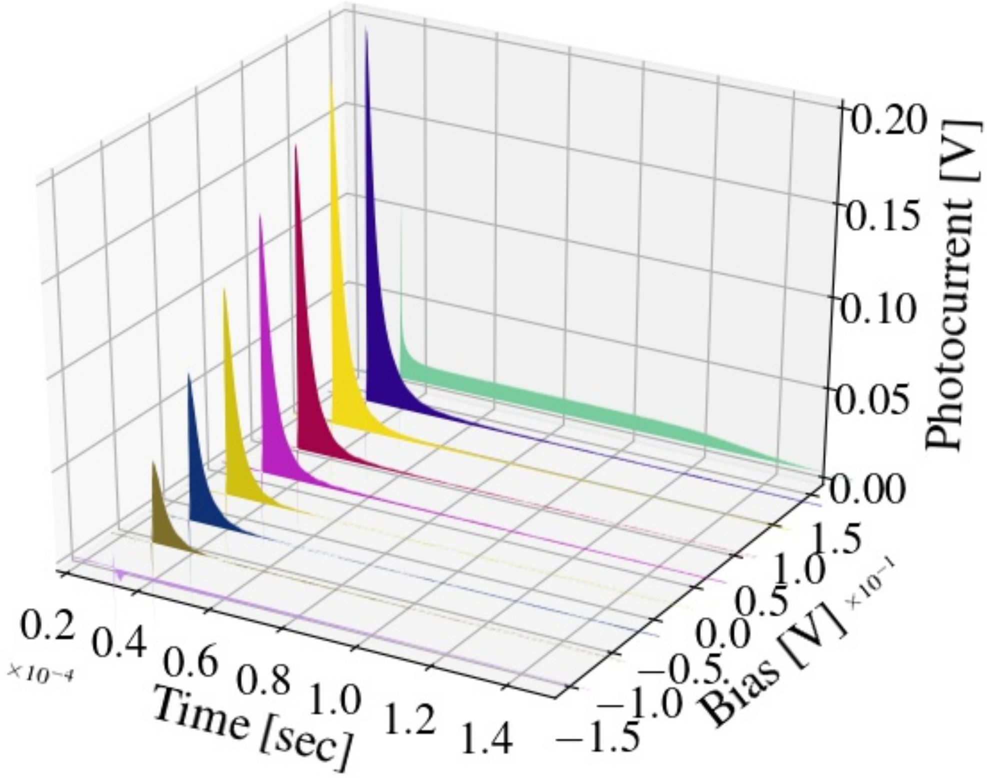

Figure 4.17: Transient photocurrent as a function of bias and time at 77 K.

As part of our experiment, we also perform the transient photocurrent measurement (Fig. 4.17). The results indicate the signal appears with a Gaussian profile under the application of the forward bias (negative voltage). With increasing the bias, the intensity rises until a shoulder appears. The width of the signal is then increasing at higher electric fields, while the signal diminishes and vanishes above the certain point.

We believe that the plateau region of the transient comes from the motion of a sheet of photo-generated electrons moving with an effective drift velocity v. At the same time, the sheet becomes spatially broadened due to the diffusion process which can be cast into an effective diffusion constant D. Therefore, the current vanishes gradually as the carriers reach the contact [91].

Generally, the time for the electron packet to drift from top surface to the collector contact at the back surface is $t_d = L/v$, where L is the spacing between contacts and $v = \mu_n E$ is the electron packet velocity. The delay time t_d is determined by measuring the output pulses versus time for varying amplitude input pulses. However, the duration of the signal is ultimately limited by the bandwidth of the measurement system. The current measurement setup utilizes a current amplifier with minimum 1 μs rise-time, which an accurate estimation of the transient time in the sample. However, the qualitative characteristics of the transient photocurrent can be still investigated through this measurement.

An alternative approach to extracting the transport time is to use the ratio of the photo-generated charge Q to the peak photocurrent, provided the signal has been quantitatively analyzed in the photocurrent measurement.

This analysis can be further extended to estimate the drift mobility as

$$\mu_d = \frac{L^2 dI_p}{Q dv_{app}}. \tag{4.20}$$

While the absolute values of the drift mobility are somewhat uncertain due to the incomplete knowledge of the drift length L, the temperature dependence of μ_d can be measured rather accurately.

Analytically, drift mobility can be calculated through Esaki-Tsu model [87], with some simplifying assumptions, or through Relaxation time approximation. Esaki-Tsu model predicts the drift velocity in the limit of $F->0$ as

$$\mu_0 = \frac{e\tau\Delta d^2}{2\hbar^2}, \tag{4.21}$$

with τ being a scattering time.

Esaki-Tsu model is oversimplified, and it is necessary to incorporate more realistic ingredients into the theory in order to have a chance of obtaining a quantitative agreement with experiment and of extracting significant information on the physical processes involved in the miniband transport. Instead, the field-dependence of the drift velocity can be reproduced by a solution of Boltzmann equation which considers the occupation of the lowest miniband at finite temperatures [23]. The Boltzmann equation provides a natural frame for the case of a homogeneous infinite medium without the magnetic field, and it accounts for the thermal broadening due to the finite lattice temperature[87].

A more complete solution of Boltzmann's equation in the nondegenerate limit leads to

$$v_d(F) = A_1 \frac{I_1(\Delta/2k_BT)}{I_0(\Delta/2k_BT)} \frac{F/A_2}{1+(F/A_2)^2} \tag{4.22}$$

where, $A_1 = d\Delta/(2\hbar)$ and $A_2 = \hbar/(e\tau d)$, I_n are the modified Bessel functions of order n. The drift mobility at low electric fields is then given by

$$\mu_d = \mu_0 \frac{I_1(\Delta/(2k_BT))}{I_0(\Delta/(2k_BT))} \tag{4.23}$$

Figure 4.18 shows the calculated drift velocity based on Eq. (4.22) for a subset of multiple different miniband width (Fig.4.18.(left)) and scattering time (Fig.4.18 right).

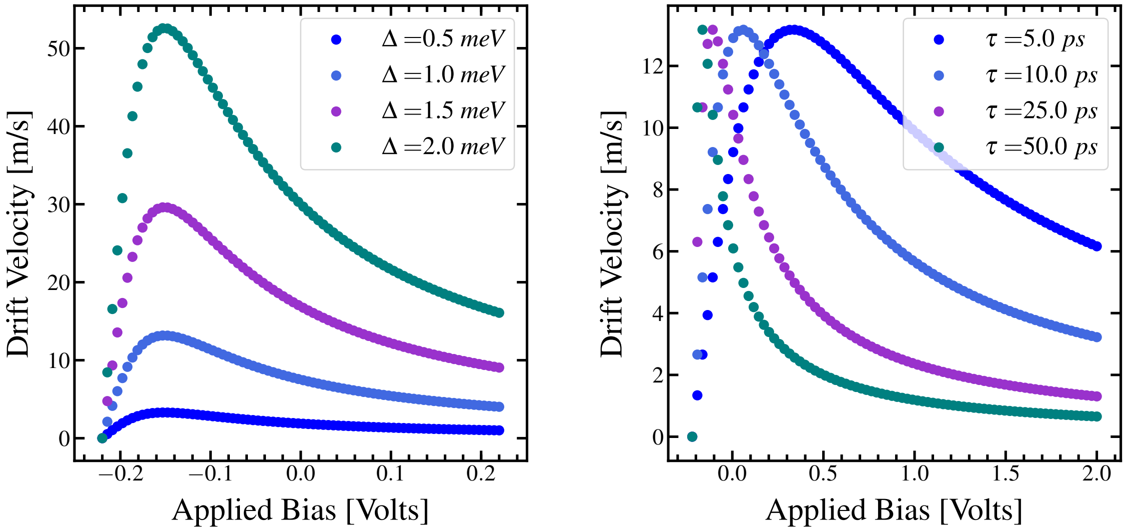

Figure 4.18: Modeled drift velocity for a 10 ML InAs / 10 ML GaSb sample with a period of 60 A for varying (left) miniband width and assuming $\tau = 40ps$, and (right) scattering time and assuming the miniband width is 1 meV.

4.5 Chapter Summary

In this chapter, the diffusion and drift characteristics of the p-type absorber in a pBn T2SL photodetector have been investigated.

For diffusion characteristics, the Electron-Beam Induced Current or EBIC technique for determining minority carrier diffusion length was investigated along with the quantum efficiency modeling technique as an alternative approach, and the results have been compared.

The time-resolved microwave reflectance method was used to obtain the minority carrier lifetime. Having the diffusion length and the minority carrier lifetime, the Einstein relation was used to obtain the minority carrier electron mobility as a function of temperature.

Lastly, the photocurrent-voltage measurement was performed to investigate the drift characteristics in the same photodiode. From the plot of the peak-photocurrent versus applied voltage, the effect of NVD is observed. For the quantitate study of the drift velocity and mobility, the measurement system with high bandwidth and minimum induced-noise needs to be chosen. Furthermore, the model based on the Boltzmann equation has been presented, which can be used to model the drift velocity. By fitting this model to the experimental measurement, one extract parameters such as miniband width, and the scattering time as fitting parameters.

Chapter 5

Many-body Perturbation Theory Study of Superlattices

T2SLs have been in the focus of the infrared technology for the last two decades, however, they have not yet achieved their predicted functionality in practice, due to their low lifetime and high level of dark current attributed to the presence of generation-recombination (G-R) centers, which is associated with native defects and residual impurities[13]. The physics behind all of these effects lies in the band structure and the band topologies of superlattices. Therefore, accurate representation of narrow band gap T2SLs is necessary to study their electronic properties and later, address the charged impurities and interfacial interactions in these systems.

There is a wide range of theoretical and numerical techniques that have been employed to studying the electronic properties of these superlattices, including Empirical Pseudopotential Model (EPM) [92], Empirical tight-binding [93], and k.p method [94, 95]. The latter has been vastly used due to its simple input requirements, and its modified version has been developed to incorporate the effect of interface interactions for superlattices with no common atom at the interfaces between the two sublattices, such as InAs/GaSb T2SLs [96, 97]. The downside of all these methods is that the fitting to experimental data largely determines the extent of their predictive capability. Also, these methods are not very well suited to address point defects and interfacial layers that are becoming increasingly important for devices such as infrared detectors and focal plane arrays based on these superlattices.

To provide a more accurate representation of the electronic properties of narrow band gap T2SLs and to study the presence of impurities and interfacial interactions, atomistic *ab-initio* calculations are inevitable. In this chapter, the results of a study on the electronic structure of long-period T2SLs are presented, using parameter-free many-body perturbation theory in the GW approximation [98, 99].

5.1 Theory

Band theory is one of the most powerful and insightful models to describe the matter with periodic boundary conditions. The periodicity of the structure implies that one needs to evaluate the energy per unit cell, instead of the total energy (in an extensive manner). The symmetry then allows one to extract this energy per cell by doing the calculations in the so-called 1^{st} Brillouin Zone(BZ) which resembles the irreducible unit cell in the reciprocal lattice [100]. The energies of free electrons in a lattice are obtained by folding the energy-momentum hyperbolic dispersion curve into the 1^{st} BZ and filling up the bands according to the Pauli exclusion principle. The problem becomes complicated soon when one wants to include the Coulomb interaction between the electrons. Tracking the problem would become impossible if it wasn't for the art of approximations! In the following, an introduction of the great ideas developed in the past 60 years to tackle this problem is presented.

In general, there are two types of band structure computation for semiconductors (which is the primary interest, here) each of which has their advantages and limitations. The first set includes parametric (empirical) models. These methods are usually simple models with the physical insight of what one expects to happen. By fitting some parameters from the experiment, these models provide information about some other quantities like electronic band gaps, effective masses of carriers, etc. These models do not always capture the correct physics in the matter, especially for complicated structures like semiconductor superlattices.

The other approach which is more adapted and developed by chemists are 'First-Principles' methods, labeled by 'ab initio'. These techniques have no fitting parameters. The only input to these models is the charge and mass of the electron. But of course, depending on the level of sophistication, they employ different approximations, which makes them computationally expensive and involved. Computationally, by minimization of the ground state energy as a function of atomic spacing, equilibrium lattice constants and atomic spacings in the unit cell can be predicted. Knowing the energy per cell, one can evaluate other properties such as the elastic constants and vibrational frequencies, and thermal properties. Extensions of these techniques to calculate excited-state properties introduce more sophisticated and involved approaches which led to predictions of optical and photoemission spectra in good agreement with experimental results.

This section reviews our adopted techniques for theoretically studying the semiconductor materials using the latter approach.

5.2 Problem Statement

the energy per cell of a crystal, for the ground state and the few excitations (called quasi-particles) is all is necessary for the calculations, including the electronic band gaps, absorption spectra, carriers effective masses and etc. In order to calculate the energy of a crystal, the following Shrodinger equation is to be solved

$$\mathcal{H}\psi = E\psi \tag{5.1}$$

with the Hamiltonian ($\mathcal{H}$) defined as

$$\mathcal{H} = \sum_i \frac{p_i^2}{2m_i} + \sum_j \frac{p_j^2}{2M_j} + \frac{1}{2}\sum_{i',j}{}^{'} \frac{Z_j Z_{j'} e^2}{|R_j - R_{j'}|} - \sum_{j,i} \frac{Z_j e^2}{|r_i - R_j|} + \frac{1}{2}\sum_{i,i'} \frac{e^2}{|r_i - r_{i'}|} \tag{5.2}$$

In this expression r_i denotes the position of the i_{th} electron, R_j is the position of the j_{th} nucleus, Z_j is the atomic number of the nucleus, p_i and P_j are the momentum operators for the electrons and nuclei, respectively, and -e is the electronic charge. $\sum'$ means that the summation is only over pairs of indices which are not identical.

The interaction among the ions is evaluated by Ewald technique[101]. The interaction between electrons and the nuclei can be replaced by pseudo-potentials or directly evaluated. The interaction among the electrons, i.e. the many-body effect in the Hamiltonian above is what makes it impossible to solve without approximations (yet physical ones). The main approximations in typical studies of this sort are the following:

(1) **Born-Oppenheimer approximation** aka adiabatic approximation: Ions are much heavier than electrons, so, one can assume that when one changes the configuration of the ions, the electronic wavefunction comes to a steady state, instantly; i.e. one can decouple the degrees of freedom of the ions from those of electrons and therefore, the Hamiltonian becomes a parametric function of ionic positions.

(2) **Mean-field approximation**: Assumes that each electron experiences the average effect of the others, not interacting with the other electrons explicitly, one-by-one. This average effect on the electrons is called the effective potential $v(r)$, thus one solves for one-body Schrodinger equation for each electron. It should be noted that the effective potential depends on the electronic states, Therefore, one needs to solve for these one-body equations self-consistently(an example of this is discussed in the

Density Functional Theory section).

(3) **Pseudo-potential approximation**: The core electrons are those that are in the fully occupied orbitals, and are localized around the nuclei. These electrons may not contribute to the chemical reactions within the solids as the valence electrons do. Hence, one bundles the nuclei + core electrons and treat them as ions in the simulations. This approach reduces the computational cost. The pseudo-potential resembles the interaction between the electrons and the ions in the crystal. For more details about how it is done see Ref. [102].

5.2.1 Density-Functional Theory

Density-functional theory(DFT) is one of the most popular and successful quantum mechanical approaches to the matter. It started by the seminal work of Hohenberg and Kohn in 1964 [103]. The formulation of Kohn-Sham in the following year [104] made a stage for the first approach to study the problem of the inhomogeneous electron gas, in practice. This theory was successful enough so that Walter Kohn won the Nobel Prize in Chemistry in 1998.

The foundations of DFT lies on two Theorems in the paper by Hohenberg and Kohn [103]. It states there is a one-to-one correspondence between the ground-state charge density n(r) of an N-interacting-electrons system and the external potential V(r) [105]. In the solid state problem, the external potential is the periodic potential of ions. This property in conjunction with the 2^{nd} Theorem (which is the same as the standard Rayleigh-Ritz variational principle of quantum mechanics) shows that a universal functional, F[n(r)], of the electron charge density exists such that the functional

$$E[n(r)] = F[n(r)] + \int n(r)V(r)dr \tag{5.3}$$

is minimized by the electron charge density of the ground state corresponding to the external potential V(r), under the constraint that the integral of n(r) equals the total number of electrons. Furthermore, the value of the minimum coincides with the ground-state energy. This is the foundation of DFT.

DFT simplifies the quantum mechanical problem of finding the ground-state properties of a system of interacting electrons by replacing the wave-function description with a much simpler description in terms of the charge density. However, the main problem in DFT is that the form of the functional F is not known. This problem has been addressed by Kohn and Sham[104] by mapping the system onto an auxiliary system of non-interacting electrons.

5.2.2 The Kohn-Sham equations

In 1965 Kohn and Sham[104] (KS) reformulated the problem in a more familiar form and opened the way to practical applications of DFT [105]. Kohn and Sham showed that by mapping the system of interacting electrons to an auxiliary system of non-interacting electrons with the same ground-state charge-density n(r), one can obtain n(r) as a sum over one-electron orbitals (the Kohn-Sham orbitals (KS)) $\psi_i(r)$ as

$$n(r) = 2\sum_i |\psi_i(r)|^2, \tag{5.4}$$

where i runs from 1 to $N/2$ if one assumes double occupancy of all states, and the KS orbitals are the solutions of the Schrodinger equation

$$(-\frac{\hbar^2}{2m}\nabla^2 + V_{KS}(r))\psi_i(r) = \epsilon_i\psi_i(r), \tag{5.5}$$

which obeys the orthonormality constraint

$$\int \psi_i^*(r)\psi_j(r)dr = \delta_{ij}. \tag{5.6}$$

Here, The existence of a unique potential $V_{KS}(r)$ having n(r) as its ground state charge density is a consequence of the Hohenberg and Kohn theorem, which holds irrespective of the form of the electron-electron interaction potential. $V_{KS}(r)$ can be written as

$$V_{KS}(r) = V(r) + e^2 \int \frac{n(r')}{|r - r'|} dr' + v_{xc}(r), \tag{5.7}$$

where $V(r)$ is the ion potential applied on electrons, the second term is the electrostatic potential between the clouds of charges, which is also known as 'Hartree' potential. And lastly, $v_{xc}(r)$ is the exchange-correlation potential, containing all the remaining unknown terms, that is not known how to be calculated. v_{xc} is usually calculated with approximations such as the Local Density Approximation (LDA), proposed by Kohn-Sham. LDA assumes that each small volume of the system (so small that the charge density can be thought to be constant therein) contributes the same exchange-correlation energy as an equal volume of a homogeneous electron gas at the same density, i.e., v_{xc} is assumed to be a function of the local charge density, only. LDA gives good results for the ground state properties such as the cohesive energies and charge density of the valence electrons. However, it gives poor results for the excitation energies. For instance, it typically underestimates the fundamental energy gap.

In general, DFT is a ground-state theory and KS eigenvalues and eigenvectors do not have a well defined physical meaning [104, 106]. The shortcoming of the DFT-LDA can be addressed by techniques which include the correlations among the electrons, more accurately. The many-body perturbation theory is one of the most successful and practical ones, nowadays.

5.2.3 Many-Body Perturbation Theory

To study the excitation properties of semiconductors like electronic band gaps and absorption spectra, one needs to consider the dynamical response of the system to the external perturbation, in this case, the introduction of an electron-hole pair because of photon absorption. Hedin introduced the GW approximation to explicitly describe this response[107], where the relaxation of the wave functions of electrons in the perturbed system due to the addition of an electron or hole gives rise to the screening of the bare Coulomb potential. Therefore, the electric potential on the added electron would be different from the scheme without screening, as in DFT. Hedin derived a set of self-consistent equations to solving for 'self-energy' which is essential to describe the low-energy excitations of the many-body system. These excitations are called 'quasiparticles.' The self-energy is approximated by the product of one-body interacting Green's function, G, and the dynamically screened interaction potential, W[108, 99], if one approximates the so-called 'vertex function' [107] to be diagonal in time and space. The vertex function is nothing but the negative variance of the inverse Green's function w.r.t. the Hartree potential, i.e. $V_H = \int \frac{\rho(\mathbf{r}')d\mathbf{r}'}{|\mathbf{r}-\mathbf{r}'|}$. Hence, the self-energy reads

$$\Sigma(\mathbf{r_1}, \mathbf{r_2}; E) = \frac{i}{2\pi} \int_{-\infty}^{\infty} G(\mathbf{r_1}, \mathbf{r_2}; E-\omega) W(\mathbf{r_1}, \mathbf{r_2}; \omega) e^{-i\omega\eta} d\omega, \tag{5.8}$$

where η is a positive infinitesimal. In the solid-state calculations with periodic boundary conditions, the single particle wavefunctions, in which the matrix elements is represented, are the DFT wavefunctions labled by $|n\mathbf{k}\rangle$. Here, n is band index, $\mathbf{k}$'s are sampled points in the 1^{st} BZ. The Fourier transform of the one-body interacting Green's function can be written as [109]

$$G_{n\mathbf{k}}(\omega) = \left[G^0_{n\mathbf{k}}(\omega)^{-1} - \Sigma_{n\mathbf{k}}(\omega) + V^{xc}_{n\mathbf{k}}\right]^{-1}, \tag{5.9}$$

where G^0 is the non-interacting Green function (corresponding to $\Sigma = 0$; However, it is custom to construct G^0 from DFT wavefunctions and energies) and V_{xc} is the exchange-correlation potential in DFT calculations. The Fourier transform of the other ingredient in self-energy, i.e., screened interaction W is [110]

$$W_{\mathbf{GG'}}(\mathbf{k}, \omega) = \epsilon^{-1}_{\mathbf{GG'}}(\mathbf{k}, \omega) v(\mathbf{k} + \mathbf{G'}). \tag{5.10}$$

Here, $\mathbf{G}$'s are reciprocal lattice vectors, and the Fourier transform of the dielectric matrix is [110, 99]

$$\epsilon_{\mathbf{GG'}}(\mathbf{k}, \omega) = \delta_{\mathbf{G},\mathbf{G'}} - v(\mathbf{k} + \mathbf{G}) P_{\mathbf{GG'}}(\mathbf{k}, \omega). \tag{5.11}$$

In the above equation, $v(\mathbf{k})$ is the Fourier transform of the bare Coulomb potential, and P are the polarization function (to see the final relations for self-energy in reciprocal lattice, see [109]). Regarding the semantics, when either screened interaction W or one-body Green's function G is constructed from the non-interacting entities (e.g. DFT energies and wavefunctions) they are denoted by W_0 and G_0; Otherwise, the subscript '0' is dropped. The dielectric function in eq. **??** can be evaluated by the Random Phase Approximation (RPA). In this case, one assumes the vertex function to be zeroth order in screened interaction potential (diagonal in time and space); The polarizability can then be obtained by the non-interacting Green's function, i.e. $P(\mathbf{r_1}, \mathbf{r_2}; \tau) = -iG^0(\mathbf{r_1}, \mathbf{r_2}; \tau) G^0(\mathbf{r_2}, \mathbf{r_1}; -\tau)$ [99, 111] (for the expression of the response function - intimately related to polarization function - in reciprocal lattice see [109]). Thus, the dielectric matrix in RPA can be evaluated by the knowledge of DFT energies and wavefunctions. But this approach is computationally expensive, in practice. An efficient way to obtain the dielectric matrix - based on observations on the imaginary part of the screened interaction - is first to obtain the static dielectric constant, i.e. $\epsilon(\mathbf{k}, \omega = 0)$ within first-principles methods, such as DFT. Then, using appropriate models (Plasmon-Pole-Approximation (PPA)) one can extend it to finite frequencies. The parameters in PPA are obtained by exact sum rules such as Kramer-Kronig relation, generalized f-sum-rule, and the static dielectric constant [110, 108, 99]. This is the approach adopted in the present study.

Having the complex, nonlocal and energy-dependent self-energy, one ends up with the one-body effective equation for the quasiparticle energies [108]

$$\begin{aligned}&\left[-\tfrac{1}{2}\nabla^2 + V_{ext}(\mathbf{r}) + V^H(\mathbf{r}) - E_{n,\mathbf{k}}\right]\psi_{n,\mathbf{k}}(\mathbf{r})\\&+\int d^3\mathbf{r}'\Sigma(\mathbf{r},\mathbf{r}',E_{n,\mathbf{k}})\psi_{n,\mathbf{k}}(\mathbf{r}') = 0,\end{aligned} \tag{5.12}$$

where, V^H is the Hartree potential, and $\psi_{n,\mathbf{k}}$, $E_{n,\mathbf{k}}$ are quasiparticles wavefunctions and energies, respectively. In practice, if one wants to do single-shot $\mathrm{G_0W_0}$, knowing that the wavefunctions of the quasiparticles are practically the same as the DFT wavefunctions, one performs the so-called 'diagonal $\mathrm{G_0W_0}$' (instead of solving a large eigenvalue problem). So, the energies of the quasiparticles are obtained in the following perturbative way

$$E_{n,\mathbf{k}} \simeq \varepsilon_{n,\mathbf{k}} + \langle\phi_{n,\mathbf{k}}|\Sigma_{G_0W_0}(E_{n,\mathbf{k}}) - V_{xc}|\phi_{n,\mathbf{k}}\rangle, \tag{5.13}$$

where $\phi_{n,\mathbf{k}}$ and $\varepsilon_{n,\mathbf{k}}$ are DFT wavefunctions and their corresponding energies for all the bands n as well as $\mathbf{k}$-points in the 1^{st} irreducible Brillouin zone. The energy-dependence of the self-energy in RHS of the eq. **??** suggests that the calculation of the energy correction is a bit more involved [109, 108]. The readers are encouraged to consult the references [111, 99] for extensive reviews on GW methodology.

5.3 Computational Details

In this work, several InAs/GaSb T2SLs were studied, including (4,7), (6,7), (8,8), (10,8), and (10,10) in (monolayers (ML) of InAs, monolayers of GaSb). These superlattices were chosen based on the availability of experimental data, and to test different structures with various electronic properties from wide-band gap (short-wavelength) to narrow-band gap (mid-wavelength). The total atoms per unit cell used in each material are 46, 54, 68, 76 and 80, respectively. Care was taken to simulate the structures as close as possible to the experimental growth condition in our laboratories and other reports in the literature [112, 113, 114, 115]. Figure 5.1 shows the unit cell of an (n, m) T2SL, along with the type-II broken-gap alignment of its constituent materials. In the experiment, the structures are grown on GaSb substrate with the InSb-type interface. An additional InSb layer is included to compensate for the strain introduced by the lattice constant mismatch of the constituent materials, and it yields higher carrier mobility and reduces the interface roughness [116]. Therefore, all the structures were simulated with the InSb-type interface, with in-plane lattice constant (LC) equal to that of the GaSb substrate. The vertical (growth axis) LC was then optimized to minimize the force and stress on the atoms and the faces of the simulated supercell in the level of DFT calculations, respectively. Both experimental LC (11.52 Bohr) and the relaxed LC (11.35 Bohr) of the bulk GaSb within the DFT-LDA have been tested.

To obtain the quasiparticle energies and consequently the electronic band structure in T2SLs, the ground state density of electrons is obtained self-consistently in DFT-LDA (local density approximation) as implemented in the Quantum Espresso (QE) package [102]. In QE, periodic boundary conditions are employed in all three spatial directions. Here, the norm-conserving pseudopotentials were used, with close-shell *d*-electrons considered as frozen-core states. The wave functions of the chemically-active electrons (so-called "valence" electrons) are expanded in terms of plane waves in the solid state calculations. A mesh of $7 \times 7 \times 1$ k-points was chosen to do the integration in the 1^{st} BZ of the supercell for ground state density evaluation. The superlattices are periodic in all three directions. The reason behind the anisotropic grid is due to the difference in period size along the growth and in-plane

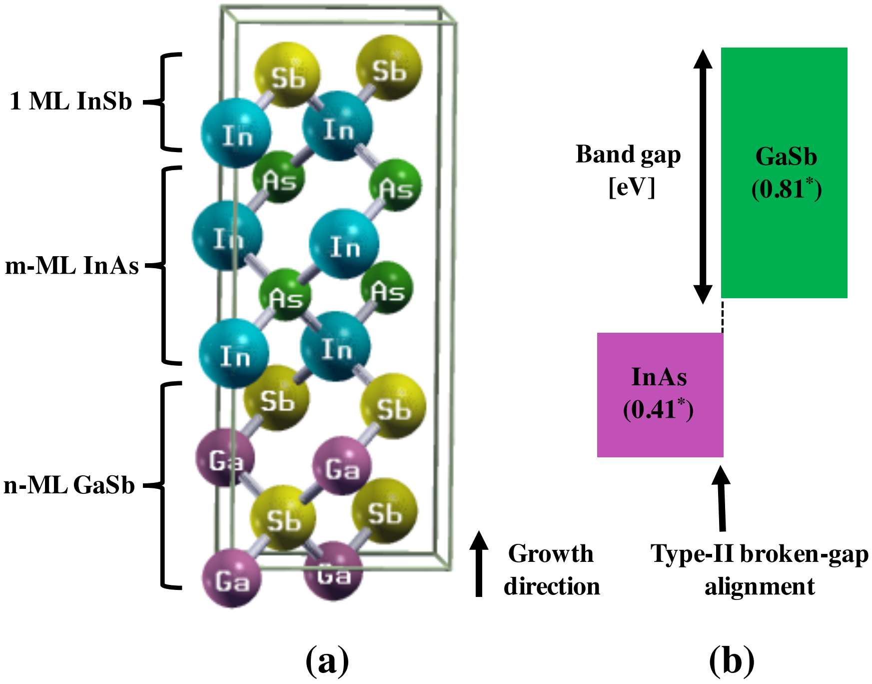

Figure 5.1: (a) Unit cell of T2SL comprises of n monolayers of InAs and m monolayers of GaSb (Shown for special case of (2,2)). Depending on the thickness of the InAs layer, a portion of strain-compensating layer of InSb is introduced in the unit cell, denoted as interfacial (IF) layer, (b) Type-II band alignment between InAs and GaSb. *Experimental band gap in eV is shown for each of InAs and GaSb. [117]

directions (Fig. 5.1). The cutoff energy which determines the number of plane waves in the expansion of wave functions was set to be 80 Ryd. Both the k-point grid and the cut-off energy were converged to achieve a change in total energy per supercell lower than 0.0001 Ryd.

The DFT energies and wave functions were then used to perform GW calculations as implemented in the Yambo code [109], employing Plasmon-Pole Approximation (PPA). The GW parameters were carefully converged so that the change in the calculated band gap in the Γ-point is less than 2 meV. These parameters are the number of plane waves in the calculation of the exchange self-energy, the dimension of reciprocal space in the dielectric constant calculation, the number of bands in the expansion of the Green's function, the total number of bands in the polarization function calculation, and the number of k-points in the 1^{st} BZ. The optimized final values of these parameters were 4500 RL, 4500 RL, 1600, 1600, and $5 \times 5 \times 1$, respectively (RL = Reciprocal Lattice unit). These parameters were converged for (10,10) superlattice and used them for all the structures.

GW calculations were performed limited in the self-consistent construction of G, only, by iterating over G in its spectral representation as in [108]

$$G^{(i+1)}(\mathbf{r}, \mathbf{r}'; E) = \sum_{n\mathbf{k}} \frac{\phi_{n,\mathbf{k}}(\mathbf{r})\phi^{\star}_{n,\mathbf{k}}(\mathbf{r}')}{E - E^{(i)}_{n,\mathbf{k}} - i\delta_{n,\mathbf{k}}}, \tag{5.14}$$

where $\phi_{n,\mathbf{k}}$ are DFT wavefunctions, and $E^{(i)}_{n,\mathbf{k}}$ are quasiparticle energies in the i^{th} iteration. The GW_0 calculations were performed until the band gap changes less than 0.01 eV.

5.4 Results and discussion

In general, one should construct appropriate pseudopotentials to study the superlattices, which are transferable enough to accommodate the unique medium the atoms experience in them. Constructing these pseudopotentials were outside the scope of the present work. GW calculations on T2SL parent compounds, bulk InAs, and bulk GaSb, were performed as a benchmark to select the appropriate pseudopotentials. The experimental LC of 11.52 Bohr and 11.44 Bohr were used for GaSb and InAs, respectively. The crystal structure for both parent compounds is face-centered cubic (fcc). In Table 5.1, the calculated band gaps is summarized, and compared to other theoretical [118] and experimental results at 0 K [117]. The Ga and Sb pseudopotentials led to a good agreement between the G_0W_0 and the experiment for the bulk GaSb. The In and As pseudopotentials led to an overestimation of the band gap of the bulk InAs in G_0W_0, which most probably is caused by treating the *d*-electrons of In as core electrons [119], or not including spin-orbit coupling (SOC) [118]. The effect of SOC should be investigated on T2SLs, independently.

Table 5.1: Simulated and experimental band gaps in eV for the bulk materials, i.e. InAs and GaSb. The results are for experimental lattice constants of 11.52 Bohr and 11.44 Bohr for GaSb and InAs, respectively. Experimental and simulated results are for 0K.

	InAs		GaSb	
	Present Work	Ref.[118]	Present Work	Ref.[118]
DFT	0.13	-0.46	0.33	-0.13
DFT+GW_0	0.76	0.55	0.86	0.94
Exp. [117]	0.41-0.45		0.811-0.813	

Since the Γ-point transition is of interest – which is the most probable transition at low temperatures – the electronic band gaps were evaluated at the Γ-point in GW approximation at 0 K. For narrow-band gap T2SLs studied in this work, i.e. (8,8), (8,10), and (10,10), DFT-LDA predicts the highest valence band at Γ to be higher than the lowest conduction band at $L = (0.5, 0.5, 0)\frac{2\pi}{a}$ point, which suggests a semi-metallic behavior. It is believed that this stems from the fact that DFT is a ground-state theory and the excitation energies are not justified in it. Thus, the $(0.5, 0.5, 0)\frac{2\pi}{a}$ point was lifted by choosing an appropriate grid such that one can have an overall semiconducting behavior ($5 \times 5 \times 1$). The same grid was then used to perform GW calculations.

Figure 5.2 shows the results of GW relative to DFT-LDA and experiment. As expected, DFT-LDA underestimates the band gaps in all the structures, and G_0W_0 opens the gaps, leading to results in good agreement with the experiment. The effect of GW_0 is to increase the gap with respect to G_0W_0, slightly.

All structures in the present study exhibited an indirect band gap (Fig. 5.3), which has been anticipated previously [96]. There was not a reference to be conclusive whether the experimental band gaps are $\Gamma \rightarrow \Gamma$ or phonon-assisted transitions.

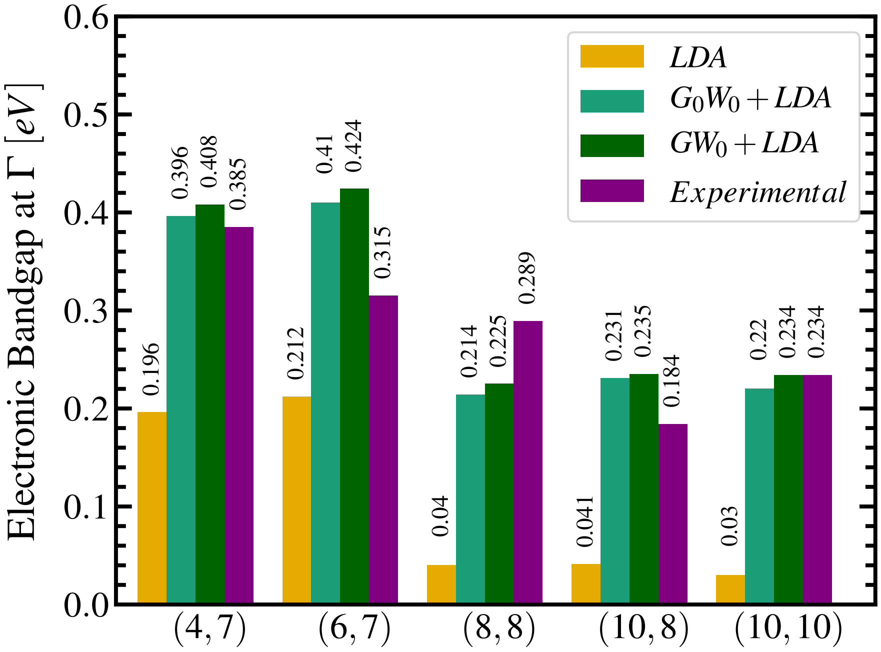

Figure 5.2: Comparison of the simulated zone center band gaps of (4,7), (6,7), (8,8), (10,8), and (10,10) superlattices within LDA, G_0W_0+LDA, and GW_0+LDA approximations, with experiment[112, 113, 114, 115]. The simulations have been performed using the experimental LC of the GaSb (11.52 Bohr). Absorption data was used as the first choice, and the photoluminescence (PL) results along with Varshni relation to extrapolate 0 K gaps from the experimental data.

So, these simulated band gaps were compared at the Γ-point with the absorption or photoluminescence data of the similar structures. It should be noted that the simulated gaps are at 0 K; Therefore, to compare with experiment, temperature shifts of the band gap was considered using Varshni relation [116].

In general, a high sensitivity of the band gaps was observed to the thickness of the IF layer used in the structures in both DFT-LDA and GW. Although the IF layer thickness in the structures was chosen as close as possible to the number of monolayers, it is expected to have in the interfacial zone during the growth process, the effect of actual layer thickness difference between the simulation and experiment

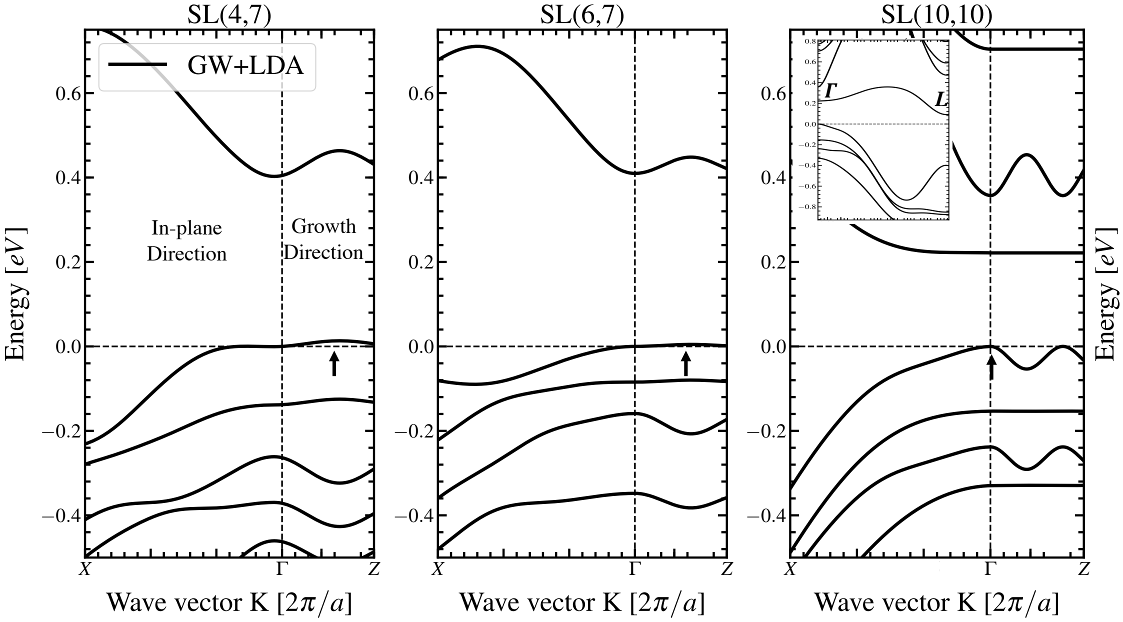

Figure 5.3: The DFT+G_0W_0 band structure of (4,7), (6,7), and (10,10) superlattices at 0K, calculated with LC=11.52 Bohr. The highest valence band is set to be zero. Arrows indicate the highest occupied levels. The inset shows the Γ-to-L direction for (10,10), in which the lowest unoccupied level happens at $L = (0.5, 0.5, 0)\frac{2\pi}{a}$.

should be considered. In (4,7) and (6,7) superlattices, half a monolayer InSb IF layer was introduced, while on the others it was a full monolayer. The IF layer in (6,7) and (8,8) superlattices were 0.27% smaller and 0.33% larger than the anticipated IF layer in the experiment, respectively. This difference can be the reason for mismatch of the band gaps compared to the experiment since structural and optical characteristics of superlattices highly depend on the IF layer thickness [120].

In T2SLs, the band gap decreases with increasing InAs layer thicknesses [123]. As can be seen in Fig. 5.2 our simulations using the experimental LC did not show

---

[1] Empirical correction

[2] absorption

[3] spectral response

Table 5.2: Summary of the simulated band gaps in eV for (8,8) and (10,10) superlattices. The structures were relaxed along the growth directions while the in-plane lattice constants were set to be equal to that of the GaSb substrate. The theoretical LC was obtained through relaxing the GaSb bulk structure in the LDA.

	(8,8)		(10,10)	
	Exp. LC	Thr. LC	Exp. LC	Thr. LC
DFT-LDA	0.04	0.09	0.03	0.047
G_0W_0+	0.214	0.358	0.220	0.286
GW_0+	0.226	-	0.234	-
Theory (others)	k.p : 0.273 [96] Hybrid DFT : 0.3 [122] EPM: 0.289 [123] DFT+Emp. : 0.292 [124]		k.p : 0.217[121] Hybrid DFT : 0.25 [122] DFT+Emp.[1] : 0.229 [124] Empirical Scissor: 0.17 [125]	
Exp.	0.283 abs.[2](77K) [123] 0.276 PL (84K) [123]		0.234 abs.(0K) [116] 0.228 SR[3] (0K) [116]	

this trend in materials with close band gaps, i.e. (8,8), (10,8), and (10,10) superlattices. The error in the present calculations might be the cause of this disorder. The dependence of the band gap on the choice of the lattice constant for (8,8) and (10,10) superlattices was studied. The experimental lattice constant is 11.52 Ryd, and the theoretical lattice constant was obtained through relaxing the GaSb bulk structure within the DFT-LDA, resulted in 11.35 Ryd. As presented in Table 5.2, it is observed that both DFT-LDA and DFT+G_0W_0 increase the band gap for the smaller lattice constant. To compare the accuracy of the simulated band gaps in the present work, the results for (8,8) and (10,10) superlattices are summarized along with the result of other studies (at different temperatures, with/without IF layer) in Table 5.2.

It should be mentioned that the interfacial effects such as interfacial diffusion and intermixing have not been considered in the present work. Regardless, GW predicts electronic band gaps in good agreement with the experiment for all the structures.

One of the main features of superlattices is their highly anisotropic nature [24].

This anisotropy results in different characteristics along the in-plane and growth-directions (z-direction). Figure 5.3 shows the band structures for (4,7), (6,7) and (10,10) superlattices with the IF layer along both directions.

DFT calculations were performed with a grid of $5 \times 5 \times 2$ k-points at the experimental lattice constant. The **k**-grid mesh was increased compared to the initial grid used for the band gap study, to better interpolate various points along the z-direction. The quasiparticle energies for this **k**-grid were obtained for the bands in the plots within G_0W_0 approximation. The simulations were performed at the lattice constant of the substrate (GaSb) which imposes a strain on the structures. This strain lifts the degeneracy at the zone-center for highest valence band in all the structures [11].

As mentioned before, all the structures exhibit indirect band gaps. In (4,7) and (6,7) the maximum of the valence band is between Γ and Z, and the minimum of conduction band happens to be at Γ. For (8,8) and (10,10), the maximum of the valence band is at Γ, and the minimum of the conduction band is at L (See the inset in Fig. 5.3 for (10,10) structure).

Band structures of (8,8) and (10,10) were found to be similar, and different from (4,7) and (6,7). It is believed this stems from the high sensitivity of the band topologies to the IF layer. In (8,8) and (10,10) the first conduction band is quite dispersionless along the growth direction, which suggests larger electron effective mass along the growth direction for these structures.

It should be noted that in T2SLs with no IF treatment, an interfacial Ga-As bond is formed from InAs-on-GaSb, whereas using the IF layer leads to having the In-Sb bond at this interface. This change in the chemical bonding at the interface alters the electronic structure and optical properties. [92, 125].

To demonstrate the effect of the IF layer, the band structures of (8,8) superlattice, with InSb-type IF layer, i.e. GaSb(8ML)/InSb(1ML)/InAs(8ML), and without InSb-type IF layer, i.e. GaSb(8ML)/InAs(8ML) are shown in Fig. 5.4. The IF layer leads to the reduction of the band gap, and the opening of the heavy-hole and the light-hole bands. With no IF layer, the conduction band shows strong dispersion along both the in-plane and growth directions, while the heavy hole band is anisotropic and has no dispersion along the growth direction.

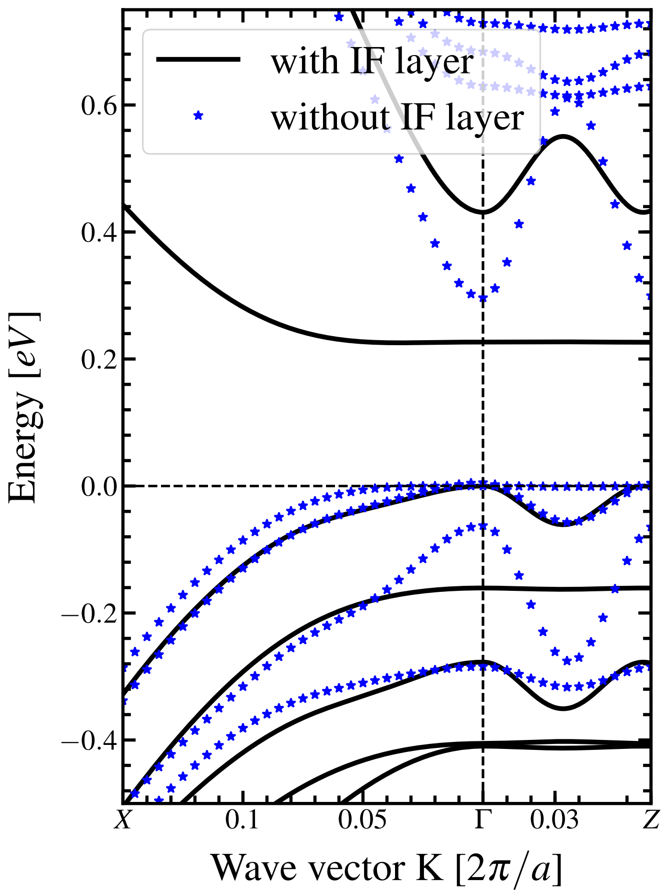

Figure 5.4: The DFT+G_0W_0 band structure of (8,8) superlattice at 0K, with and without IF layer, calculated with experimental LC (=11.52 Bohr). The highest valence band is set to be zero. (a/c) denotes the ratio of in-plane lattice constant over the dimension of the supercell along the growth direction.

It is helpful to summarize the anticipated sources of error in our simulated band structure:
(i) The validity of PPA (which has been shown to have a high dependence on the localization of the electrons in the system under study) is an issue. It has been argued that the energies of the band-edge states are sensitive to the choice of Plasmon-Pole model [126]. PPA was used to avoid the extra computational expense. However, the calculation on a test sample ((8,8) superlattice) without PPA showed an increase of 50 meV in the resultant band gap, which is not negligible for narrow band gap superlattices.
(ii) On the DFT level, better wave functions such as the ones obtained from DFT+U, and on the GW level, the vertex correction might have a significant impact.
(iii) The treatment of the open-shell d-electrons as core states, which do not contribute to the calculations, could also have substantial implications for electronic band structures. The inclusion of these electrons in the calculations for In and Ga has been reported to be influential on the structural and electronic properties [119, 118].
(iv) The fact that the simulation parameters were optimized only for one of the structures, the result of which might not be optimum for the others, might add to the error of calculations, as well.

Despite these sources of errors, GW achieves an overall good estimation of the band gaps at Γ for the structures studied in this work. However, it can not assess the GW performance unless all the above approximations are investigated separately.

5.5 Chapter Summary

In summary, GW_0 calculations were performed on a series of InAs/GaSb type-II superlattices. The calculated band gaps show a good agreement with the experimental data. However, this method was unable to predict the band gap changes with the layer thicknesses over the whole domain, which can be related to the fact that some of the materials studied in this work have close band gaps and the difference might have been within the error of the calculations. The band structures are reported for different superlattices studied in this paper and investigated the effect of the IF layer on the band structures for a test superlattice. The IF layer resulted in shrinkage of the band gap, as well as changing the band dispersion.

Chapter 6

Conclusion and Future Work

6.1 Conclusions

This dissertation focuses on the investigation of minority carrier transport in *p*-type InAs/GaSb superlattices. Specifically, the objective of this dissertation has been to determine the minority electron diffusion length using Electron-Beam Induced Current or EBIC technique. The results are then compared to the QE modeling technique. Furthermore, a comprehensive study is performed on the temperature-dependence of the carrier dynamics. The results of the electron diffusion length and the minority carrier lifetime are used to extract the electron mobility from Einstein relation.

Also, the drift characteristics are extracted using the photocurrent-voltage measurement technique. The drift velocity is also simulated based on the theoretical model obtained from the Boltzmann transport equation with varying miniband width and the scattering time.

In addition to the transport study, the density functional theory and the many-body perturbation theory are used to investigate the electronic band structure and band gap in a series of superlattices. The objectives of investigating and applying this simulation are to establish a platform for reliable calculation of the band structure and further, characterize defects in superlattices.

6.1.1 Summary of Results- Vertical Transport in MWIR InAs/GaS T2SLs

The key outcomes of the work undertaken in this dissertation on the transport study are listed below.

- **Objective-1** To determine the diffusion length of the *p*-type InAs/GaSb sample.

Results:

The electron-beam induce-current method is successfully applied to the selected *nBp* structure consisting of a *p*-type InAs/GaSb absorber. The measurements are repeated at temperatures between [80 K-150 K], and the effect of various factors such as electron-beam current and electron-beam energy in the measurement and the surface recombination at the surface of the sample are investigated.

The results indicate that increasing the electron-beam current or the electron-beam energy at a fixed temperature leads to a higher the EBIC signal. This observation has been attributed to the surface at the which the electron beam impinges on the sample, which acts as an attracting potential for the generated excess carriers due to oxide formation by exposure to oxygen in the atmosphere. So, by increasing the injection current (electron-beam current), the enhanced density of ionized centers results in the saturation of the surface states; hence, the surface-induced attractive potential for minority carriers vanishes and surface recombination diminishes, and as a result, the signal due to the diffusion of the carriers rises. Also, at higher electron-beam energies, minority carriers are generated deeper below the surface, and hence, are less likely to diffuse to the surface and recombine there. Consequently, the signal increases.

EBIC measurements are then performed for a selected electron-beam current and energies for various temperatures, and the diffusion length is extracted as a function of temperature. The resulting minority diffusion length values are found to be relatively low compared to the results obtained from the QE modeling, which was performed on the same sample. The low values of the diffusion length, in turn, led to low minority mobility values. It is hypothesized that the mobility of electrons is attenuated due to the presence of structural or growth disorders, or simply due to the presence of defects which act as trap centers and lead to localization of the carriers. The mobility is found to have a strong dependence on temperature; it shows very small change as the temperature increases from 80 K to 140 K and increases for higher temperatures. We believe this behavior stems from the fact that the localized carriers in the vicinity of the defects have set themselves free by gaining enough energy at temperatures above 140 K, which results in the enhanced-mobility.

- **Objective-2** To use the quantum efficiency modeling to determine the diffusion length of the same *p*-type InAs/GaSb sample.

Results:

An analytical study is performed based on Hovel's expression for the quantum efficiency to extract the diffusion length as the best fit between the model and the experimentally measured quantum efficiency. In this method, the surface recombination velocity is neglected and the experimental absorption coefficient data is used as the input. The results of the diffusion length are then used along with the lifetime data to calculate the diffusion coefficient and the mobility. Compared to EBIC, the QE modeling method leads to an order of magnitude higher values for the transport characteristics.

- **Objective-3** To provide comparisons for the electron diffusion length values obtained from the above techniques.

Results:

The minority diffusion length obtained via the EBIC technique for the *p*-type sample is found to be an order of magnitude lower than the values obtained from the QE modeling technique. Unfortunately, it is impossible to make any meaningful comparison between the results obtained for these techniques without an investigation of the accuracy of the models that these methods are dependent on. Nevertheless, this discrepancy can be traced back to multiple factors such as (i) the presence of undesirable recombination sites caused by a surface layer; the cleaved surface of the diode in EBIC measurement is exposed to the air and sensitive to the oxidation by air, (ii) the assumption in the EBIC and QE models in which the collection efficiency in the depletion region is equal to one; this might not be an accurate assumption in reality due to the presence of the surface damage or defects in the material, and (iii) the error in the absorption coefficient data, which has been used as an input; any error in the measurement or calculation of $\alpha(\lambda)$ can lead to noticeable error in the result of the fitting in the QE modeling.

Repeating the measurement of different samples, or using an alternative technique or a numerical model for interpretation of the data is certainly helpful to shed more light on this matter.

- **Objective-4** To compare the minority carrier mobility results with the theoretical prediction of the mobility temperature dependency.

Results:

Generally, the mobility is assumed to be limited by impurity scattering ($\sim T^{3/2}$) at lower temperatures, while at higher temperatures, it is limited by phonon scattering ($\sim T^{-3/2}$). However, none of these scattering mechanisms is found to be accountable for the observed trend in the electron mobility data.

The mobility extracted form EBIC measurements shows two distinct temperature regions of 80-140 K (region 1), and 140 K above (region 2), for 15 and 20 keV electron-beam energies. For region 1, it is believed the transport is limited by trap-assisted transport rather than miniband conduction, due to the presence of the deep-level states. In the presence of localized imperfections, the wave functions of energy states are localized in the vicinity of the impurity. The carriers tend to be localized with deteriorated mobility, which is controlled by the extent to which the carriers can be released from these bound impurity states[41]. It is found that the increase in the temperature above 140 K leads to increase mobility, which can be associated with the carriers setting free from the impurity states, with an activation energy of 115 meV.

- **Objective-5** To determine the drift characteristics using photocurrent-voltage measurement.

Results:

The photocurrent-voltage measurement is investigated, and the peak of the photocurrent is extracted as a function of bias. The results show the NDV effect in the region of reverse bias. The model based on the Boltzmann equation is used to calculate the drift velocity having the miniband width and the scattering time as varying parameters.

6.1.2 Summary of Results- Electronic Structure Characterization

The key outcomes of the work undertaken in the investigation of the electronic band structure are listed below.

- **Objective-1** To determine the band gap at gamma for a series of InAs/GaSb superlattices.

Results:

LDA+GW$_0$ calculations were performed on a series of InAs/GaSb type-II superlattices. The calculated band gaps show a good agreement with the experimental data. However, this method is found to be unable to predict the band gap changes with the layer thicknesses over the whole domain, which can be related to the fact that some of the materials studied in this work have close band gaps and the difference might have been within the error of the calculations. Possible sources of error in the calculation is also reviewed.

- **Objective-2** To calculate the electronic band structure in various superlattices.

Results:

The band structures for different superlattices are calculated and the effect of the IF layer on the band structures for a test superlattice is investigated. As expected from the experimental data, the simulation result indicates that the inclusion of the IF layer leads to the shrinkage of the band gap, as well as changing the band dispersion in superlattices.

6.2 Future Efforts

This dissertation has tried to establish a framework to extract minority transport properties. However, there still are a few essential questions needed to be addressed regarding the transport in type-II superlattices, including (i) What is the role of the effective mass in reduced transport? (ii) How one can improve the transport by type-II superlattices design, and growth technique? (iii) What effect does Sb segregation have? (iv) What effect does scattering mechanisms/interfacial roughness have?

A systematic study has to be designed in order to study the effect of each of these factors on transport.

Furthermore, the application of the superlattice to investigate the miniband transport and effects such as the NVD has been under active research for decades. However, most of the work has been focused on the type-I superlattices, and the application of type-II superlattices is quite new for this purpose. In this work, a qualitative investigation of photocurrent-voltage measurement is presented. With a high bandwidth and low noise measurement setup, one can investigate the time-of-flight and the current-voltage behaviors in this material system, and perform the quantitative study of the drift characteristics such as the drift velocity or the drift mobility.

Lastly, there are many technical challenges in performing *ab-initio* calculations on T2SLs, some of which have been addressed in this work. Nevertheless, our study serves as a candidate to further explore the underlying physics of these systems, and opens a wide variety of directions, for instance, the study of structural defects and interfacial atomic inter-diffusion, and band gap engineering for the next generation IR detectors. Also, another interesting idea is to investigate the optical spectra of T2SLs within this framework.

The high dark-current exhibited by InAs/GaSb T2SLs is attributed to short carrier lifetimes limited by Shockley-Read-Hall (SRH) centers. It has been hypothesized that native defects associated with GaSb are responsible for the SRH-limited minority carrier lifetimes observed in InAs/GaSb T2SLs [13]. The InAs/InAsSb superlattices, on the other hand, has shown to be a potential type-II alternative to the InAs/GaSb system for infrared photodetectors due to their much longer recombination lifetimes [14, 15]. As part of the future work can be a new sample design such as the LWIR Ga-free InAs/InAsSb T2SL with *n*-type and *p*-type doped absorbers. InAs/InAsSb type-II superlattices have been under active research in unipolar architecture *nBn* mostly, due to its minimized surface effect when *n*-doped. However, the minority holes are the slower carrier and hence, lead to deteriorated transport. Nevertheless, the quantum efficiency reported for the InAs/InAsSb *nBn* photodetectors are comparable to that of the photodetectors based on InAs/GaSb. It is part of our future project to investigate the transport in this material system to further optimize its electronic properties.

6.3 Concluding Remarks

Optoelectronic devices operating in the IR regions of the electromagnetic spectrum are of great interest for various applications such as academics, healthcare, industry, and military/defense. The current state-of-the-art infrared technology utilizes the HgCdTe ternary alloys, which have major drawbacks such as challenging growth and composition non-uniformity, particularly for LWIR devices. Conversely, InAs/GaSb strained-layer superlattice diodes are predicted to have a number of advantages over bulk HgCdTe, including better uniformity, an easier process of growing epitaxially, lower tunneling current, and suppressed Auger recombination rates [127]. However, superlattices have not yet achieved their theoretically predicted functionality. Therefore, there is a need to investigate the fundamental physics of T2SLs to understand the limitations and harvest the potential of devices technology based on these materials. One of the critical characters is the vertical transport in this anisotropic quantum-confined system.

Theoretical and experimental efforts, such as this dissertation, seek to investigate the fundamental physical properties of InAs/GaSb type-II superlattices. This dissertation has been a comprehensive study on the drift and diffusion characteristics, the minority carrier lifetime and its limiting mechanisms, and the electronic band structure. The results obtained in this work can be considered to be a part of an ongoing attempt to understand the fundamental characteristics of the superlattices and correlated it to the performance of the optoelectronic devices based on them.

Statement of Contribution

The author of this work has been involved in numerous projects with infrared detection technology. Contributions have been made with regards to the design and modeling, fabrication, and characterization of the superlattice material and the photodetectors. The results of these projects are presented in the following published works. The name of the author of this dissertation is emphasized in boldface.

•**Z. Taghipour** et al. ”*Temperature-dependent minority carrier mobility in p-type InAs/GaSb type-II superlattice photodetector,*” under review in the Journal of Physical Review Applied.

•**Z. Taghipour** et al. ”*Vertical Transport Study of InAs/GaSb Type-II Superlattice nBp MWIR Detectors using Electron Beam-Induced Current Measurements.*” SPIE Defense and Security, International Society for Optics and Photonics, (2018) [128]

•**Z. Taghipour** et al. ”*Many-body Perturbation Theory Study of Type-II InAs/GaSb Superlattices within GW approximation.*” Journal of Physics: Condensed Matter (2018) [129]

•A. Kazemi, S. Myers, **Z. Taghipour** et al. ”*Mid-Wavelength Infrared Unipolar nBp Superlattice Photodetector.*” Infrared Physics and Technology (2017) [12]

•**Z. Taghipour** et al. ” *Extraction of Minority Carrier Diffusion Length of MWIR Type-II Superlattice nBp detector.*” SPIE Optics and Photonics, International Society for Optics and Photonics (2017) [130]

•A. Kazemi, S. Myers, **Z. Taghipour** et al. ”*High quantum efficiency mid-wavelength infrared superlattice photodetector.*” SPIE Defense and Security, International Society for Optics and Photonics (2017) [131]

•B. Klein, C. Hains, **Z. Taghipour** et al. ”*Photo-capacitance study of GaSb: In, As for defect analysis in InAs/GaSb type-II strained-layer superlattices.*” Infrared Physics and Technology (2015) [132]

•**Z. Taghipour** et al. ”*Electronic Structure of Type-II InAs/GaSb Superlattices: a DFT+ GW Study*” Bulletin of the American Physical Society (2018) [133]

References

[1] A. Rogalski, P. Martyniuk, and M. Kopytko. Challenges of small-pixel infrared detectors: a review. *Rep. Prog. Phys.*, 79:046501, 2016.

[2] M. A. Kinch. HgCdTe: Recent Trends in the Ultimate IR Semiconductor. *Journal of Electronic Materials*, 39(7), 2010.

[3] A. Rogalski. HgCdTe infrared detectors historical prospect. *Proc. of SPIE*, 4999(July 2003), 2003.

[4] C. Smith and D. L. Mailhiot. Proposal for strained type II superlattice infrared detectors. *Journal of Applied Physics*, 62(95), 1987.

[5] B. F. Levine. Quantumwell infrared photodetectors. *Journal of Applied Physics*, 74(8):R1–R81, oct 1993.

[6] A. Rogalski. Infrared detectors status and trends 2003.pdf. *Progress in Quantum Electronics*, 27:59–210, 2003.

[7] D. Z. Ting, A. Soibel, H. Linda, J. Nguyen, C. J. Hill, A. Khoshakhlagh, and S. D. Gunapala. Type-II Superlattice Infrared Detectors. In *Semiconductors and Semimetals*, volume 84, pages 1–57. Elsevier, Inc., 2011.

[8] R. Tsu and L. Esaki. Superlattice and Negative Differential Conductivity in Semiconductors. *IBM Journal of Research and Development*, 14(1):61–65, 1970.

[9] C. Jacoboni. *Theory of Electron Transport in Semiconductors: A Pathway from Elementary Physics to Nonequilibrium Green Functions.* Springer, 2010.

[10] L. Esaki. The Global Reach of Japanese Science, 1996.

[11] D. L. Smith and C. Mailhiot. Theory of semiconductor superlattice electronic structure. *Reviews of Modern Physics*, 33(12):8345–8359, 1986.

[12] A. Kazemi, S. Myers, Z. Taghipour, S. Mathews, T. Schuler-Sandy, S. Lee, V. M. Cowan, E. Garduno, E. Steenbergen, C. Morath, G. Ariyawansa, J. Scheihing, and S. Krishna. Mid-wavelength infrared unipolar nBp superlattice photodetector. *Infrared Physics and Technology*, 88:114–118, 2018.

[13] S. P. Svensson, D. Donetsky, D. Wang, H. Hier, F. J. Crowne, and G. Belenky. Growth of type II strained layer superlattice , bulk InAs and GaSb materials for minority lifetime characterization. *Journal of Crystal Growth*, 334(1):103–107, 2011.

[14] E. H. Steenbergen, B. C. Connelly, G. D. Metcalfe, H. Shen, M. Wraback, D. Lubyshev, Y. Qiu, J. M. Fastenau, A. W K Liu, S. Elhamri, O. O. Cellek, and Y. H. Zhang. Significantly improved minority carrier lifetime observed in a long-wavelength infrared III-V type-II superlattice comprised of InAs/InAsSb. *Applied Physics Letters*, 99(25):1–4, 2011.

[15] H. S. Kim, O. O. Cellek, Z. Lin, Z. He, X. Zhao, S. Liu, H. Li, and Y. Zhang. Long-wave infrared nBn photodetectors based on InAs/InAsSb type-II superlattices. *Appl. Phys. Lett*, 101(16):161114, 2012.

[16] N. Gautam. *Unipolar Barrier Strained Layer Superlattice Infrared Photodiodes : Physics and Barrier Engineering.* PhD thesis, University of New Mexico, 2012.

[17] A. M. White. Infra red detectors, sep 1983.

[18] S. Maimon and G. W. Wicks. nBn detector, an infrared detector with reduced dark current and higher operating temperature. *Citation: Appl. Phys. Lett*, 89(15):151109, 2006.

[19] P. Klipstein. XBn Barrier Photodetectors for High Sensitivity and High Operating Temperature Infrared Sensors. *Proc. of SPIE*, 6940:69402U–1, 2008.

[20] J. F. Klem, J. K. Kim, M. J. Cich, S. D. Hawkins, T. R. Fortune, and J. L. Rienstra. Comparison of nBn and nBp mid-wave barrier infrared photodetectors. *Quantum Sensing and Nanophotonic Devices VII.*, 7608:76081P, 2010.

[21] E. O. Gobel and K. Ploog. Fabrication a N D Optical Properties of Semiconductor Q U a N T U M Wells a N D. *Progress in Quantum Electronics*, 14:289–356, 1991.

[22] S. Kasap and P. Capper. Quantum Wells, Superlattices, and Band-Gap Engineering. In *Springer Handbook of Electronic and Photonic Materials*, page 1040. Springer, Cham, 2017.

[23] H. T. Grahn, K. Von Klitzing, K. Ploog, and G. H. D??hler. Electrical transport in narrow-miniband semiconductor superlattices. *Physical Review B*, 43(14):12094–12097, 1991.

[24] Z. C. Feng. *Semiconductor Interfaces and Microstructures.* World Scientific, 1992.

[25] S. Safa, A. Asgari, and L. Faraone. A study of vertical and in-plane electron mobility due to interface roughness scattering at low temperature in InAs/GaSb type-II superlattices. *Journal of Applied Physics*, 114(5):1–7, 2013.

[26] F. Szmulowicz, S. Elhamri, H. J. Haugan, G. J. Brown, and W. C. Mitchel. Demonstration of interface-scattering-limited electron mobilities in InAs/GaSb superlattices. *Journal of Applied Physics*, 101(4):043706, 2007.

[27] F. Szmulowicz, S. Elhamri, H. J. Haugan, G. J. Brown, and W. C. Mitchel. Carrier mobility as a function of carrier density in type-II InAs/GaSb superlattices. *Journal of Applied Physics*, 105(7):1–6, 2009.

[28] J. V. Li, S. L. Chuang, E. M. Jackson, and E. Aifer. Minority carrier diffusion length and lifetime for electrons in a type-II InAs/GaSb superlattice photodiode. *Applied Physics Letters*, 85(11):1984–1986, 2004.

[29] Y. Lin, S. Suchalkin, G. Kipshidze, T. Hosoda, B. Laikhtman, D. Westerfeld, L. Shterengas, and G. Belenky. Effect of hole transport on performance of infrared type-II superlattice light emitting diodes. *Journal of Applied Physics*, 117(16):1–5, 2015.

[30] E. H. Aifer, J. G. Tischler, J. H. Warner, I. Vurgaftman, W. W. Bewley, J. R. Meyer, J. C. Kim, L. J. Whitman, C. L. Canedy, and E. M. Jackson. W-structured type-II superlattice long-wave infrared photodiodes with high quantum efficiency. *Applied Physics Letters*, 89(5):1–4, 2006.

[31] H. J. Haugan, B. Ullrich, S. Elhamri, F. Szmulowicz, G. J. Brown, L. C. Tung, and Y. J. Wang. Magneto-optics of InAs/GaSb superlattices. *Journal of Applied Physics*, 107(8):083112, 2010.

[32] X. Li, D. Jiang, Y. Zhang, G. Liu, D. Wang, Q. Yu, and L. Zhao. Investigations of quantum efficiency in type-II InAs/GaSb very long wavelength infrared superlattice detectors. *Superlattices and Microstructures*, 92:330–336, 2016.

[33] B. V. Olson, L. M. Murray, J. P. Prineas, M. E. Flatté, J. T. Olesberg, and T. F. Boggess. All-optical measurement of vertical charge carrier transport in mid-wave infrared InAs/GaSb type-II superlattices. *Applied Physics Letters*, 102(20):202101, 2013.

[34] D. Zuo, P. Qiao, D. Wasserman, and S. Lien Chuang. Direct observation of minority carrier lifetime improvement in InAs/GaSb type-II superlattice photodiodes via interfacial layer control. *Applied Physics Letters*, 102(14):141107–1, 2013.

[35] N. Yoon, C. J. Reyner, G. Ariyawansa, J. M. Duran, J. E. Scheihing, J. Mabon, and D. Wasserman. Modified electron beam induced current technique for in(Ga)As/InAsSb superlattice infrared detectors. *Journal of Applied Physics*, 122(7):074503, 2017.

[36] Y. Aytac. *Time-resolved measurements of charge carrier dynamics in Mwir to Lwir InAs / InAsSb superlattices.* PhD thesis, Iowa University, 2016.

[37] D. Zuo, R. Liu, D. Wasserman, J. Mabon, Z. He, S. Liu, Yong-hang Zhang, A Emil, Benjamin V Olson, and Eric a Shaner. Direct minority carrier transport characterization of InAs / InAsSb superlattice nBn photodetectors Direct minority carrier transport characterization of InAs / InAsSb superlattice nBn photodetectors. *Applied Physics Letters*, 106(7):071107, 2015.

[38] B. V. Olson, J. F. Klem, E. A. Kadlec, J. K. Kim, M. D. Goldflam, S. D. Hawkins, A. Tauke-Pedretti, W. T. Coon, T. R. Fortune, E. A. Shaner, and M. E. Flatté. Vertical Hole Transport and Carrier Localization in InAs/InAs1xSbx Type-II Superlattice Heterojunction Bipolar Transistors. *Physical Review Applied*, 7(2):024016, 2017.

[39] Y. Lin, D. Wang, D. Donetsky, and G. Kipshidze. Transport properties of holes in bulk InAsSb and performance of barrier long-wavelength infrared detectors. *Semicond. Sci. Technol.*, 29:112002, 2014.

[40] D. Z. Ting, A. Soibel, A. Khoshakhlagh, B. Rafol, S. A. Keo, L. Höglund, A. M. Fisher, E. M. Luong, and S. D. Gunapala. Mid-wavelength high operating temperature barrier infrared detector and focal plane array. *Citation: Appl. Phys. Lett*, 113:21101, 2018.

[41] J. Blakemore. *Semiconductor Statistics.* Dover Publications, Inc., Mineola, New York, 1962.

[42] S. L. Chuang. *Physics of Photonic Devices.* Number December. John Wiley & Sons, Incorporated, 2012.

[43] D A. Neamen. *Semiconductor Physics and Devices.* New York: McGraw-Hill, 2012.

[44] D. K. Schroder. *Semiconductor Material and Device Characterization.* John Wiley & Sons, New York, 1990.

[45] F. Capasso, K. Mohammed, and a. Cho. Resonant tunneling through double barriers, perpendicular quantum transport phenomena in superlattices, and their device applications. *IEEE Journal of Quantum Electronics*, 22(9):1853–1869, 1986.

[46] A. Wacker. Semiconductor Superlattices: A model system for nonlinear transport. *Physics Reports*, 357(1):1–111, 2002.

[47] R. N. Hall. *Recombination processes in semiconductors*, volume 106. [Institution of Electrical Engineers], 1959.

[48] L. Höglund, D. Z. Ting, A. Soibel, A. Fisher, A. Khoshakhlagh, C. J. Hill, S. Keo, and S. D. Gunapala. Minority carrier lifetime in mid-wavelength infrared InAs/InAsSb superlattices: Photon recycling and the role of radiative and Shockley-Read-Hall recombination mechanisms. *Appl. Phys. Lett*, 105(19):193510, 2014.

[49] A. R. Beattie and P. T Landsberg. Auger Effect in Semiconductor. *Proc. R. Soc. London, Ser. A*, 249(1256):16–29, 1959.

[50] V. C. Lopes, A. J. Syllaios, and M. C. Chen. Minority carrier lifetime in mercury cadmium telluride. *Semicond. Sci. Technol*, 8:824–841, 1993.

[51] T. N. Casselman. Calculation of the Auger lifetime in p-type Hg1-xCdxTe. *Journal of Applied Physics*, 52(54):848–854, 1981.

[52] S. M. Sze. *Physics of Semiconductor Devices.* John Wiley & Sons, Inc., 2007.

[53] J. Nguyen, D. Z. Ting, C. J. Hill, A. Soibel, S. A. Keo, and S. D. Gunapala. Dark current analysis of InAs/GaSb superlattices at low temperatures. *Infrared Physics and Technology*, 52(6):317–321, 2009.

[54] P. Martyniuk, J. Wróbel, E. Plis, P. Madejczyk, A. Kowalewski, W. Gawron, S. Krishna, and A. Rogalski. Performance modeling of MWIR InAs/ GaSb/ BAl(0.2) Ga(0.8)Sb type-II superlattice nBn detector. *Semiconductor Science and Technology*, 27(5):55002, 2012.

[55] H. J. Hovel. *Semiconductors and semimetals. Volume 11. Solar cells.* Academic Press, Inc., 1975.

[56] D. Wee. *Characterisation of Minority Carrier Diffusion Length Using the Photocurrent Technique in Extrinsically Doped GaN.* PhD thesis, The University of Western Australia, 2014.

[57] E. Giard, I. Ribet-Mohamed, J. Jaeck, T. Viale, R. Haïdar, R. Taalat, M. Delmas, J. B. Rodriguez, E. Steveler, N. Bardou, F. Boulard, and P. Christol. Quantum efficiency investigations of type-II InAs/GaSb midwave infrared superlattice photodetectors. *Journal of Applied Physics*, 116(4):1–7, 2014.

[58] T. E. Everhart, O. C. Wells, and R. K. Matta. Novel Method of Semiconductor Device Measurements. *Semiconductor device measurements*, 52(12):1642–1648, 1964.

[59] J. M. Bonard and J. D. Ganière. Quantitative analysis of electron beam induced current profiles across pn junctions in GaAs/Al0.4Ga0.6As heterostructures. *Journal of Applied Physics*, 79(9):6987–6994, 1996.

[60] C. Donolato. Reciprocity theorem for charge collection by a surface with finite collection velocity: Application to grain boundaries. *Journal of Applied Physics*, 76(2):959–966, 1994.

[61] K. L. Luke. The evaluation of surface recombination velocity from normal-collector geometry electron-beam-induced current line scans. *Journal of Applied Physics*, 75(3):1623–1631, 1994.

[62] H. J. Leamy. Charge collection scanning electron microscopy. *Journal of Applied Physics*, 53(6):R51–R80, 1982.

[63] W. V. Roosbroeck. Injected Current Carrier Transport in a Semi-Infinite Semiconductor and the Determination of Lifetimes and Surface Recombination Velocities. *Journal of Applied Physics*, 26(4):380, 1955.

[64] F. Berz and K. Kuikent. Theory of Life Time Measurements with the Scanning Electron Microscope: Steady State. *Solid-State Electronics*, 19:443–445, 1976.

[65] C. Donolato. Evaluation of diffusion lengths and surface recombination velocities from electron beam induced current scans. *Applied Physics Letters*, 43(1):120–122, 1983.

[66] L. K. Luke and V. O. Roos. An EBIC Equation for Solar Cells. *Solid-State Electronics*, 26(9):901–906, 1983.

[67] The Simulation Standard. Electron Beam Induced Current (EBIC) Simulation, 2007.

[68] C. M. Parish and P. E. Russell. On the use of Monte Carlo modeling in the mathematical analysis of scanning electron microscopy-electron beam induced current data. *Applied Physics Letters*, 89(19):192108–1, 2006.

[69] D. Drouin, A. R. Couture, D. Joly, X. Tastet, V. Aimez, and R. Gauvin. CASINO V2.42 - A fast and easy-to-use modeling tool for scanning electron microscopy and microanalysis users. *Scanning*, 29(3):92–101, 2007.

[70] J. I. Hanoka and R. O. Bell. Electron-beam-induced currents in semiconductors. *Ann. Rev. Mater. Sci.*, 11(4):353–380, 1981.

[71] O. Marcelot, S. I. Maximenko, and P. Magnan. Plan view and cross-sectional view EBIC measurements: Effect of e-beam injection conditions on extracted minority carrier transport properties. *IEEE Transactions on Electron Devices*, 61(7):2437–2442, 2014.

[72] S. I. Maximenko and R. J. Walters. Minority carrier diffusion length measurements in solar cells by electron beam induced current. In *2015 IEEE 42nd Photovoltaic Specialist Conference (PVSC)*, pages 1–4, 2015.

[73] M. P. Lumb, I. Vurgaftman, C. A. Affouda, J. R. Meyer, E. H. Aifer, and R. J. Walters. Quantum wells and superlattices for III-V photovoltaics and photodetectors. In Loucas Tsakalakos, editor, *Next Generation (Nano) Photonic and Cell Technologies for Solar Energy Conversion III.*, volume 8471, page 84710A. International Society for Optics and Photonics, oct 2012.

[74] L. Höglund, A. Soibel, D. Z. Ting, A. Khoshakhlagh, C. J. Hill, and S. D. Gunapala. Minority carrier lifetime and photoluminescence studies of antimony- based superlattices. In *International Society for Optics and Photonics XX. Vol. 8511*, page 851106, 2013.

[75] M. E. Flatté, C. H. Grein, T. C. Hasenberg, S. A. Anson, D. J. Jang, J. T. Olesberg, and T. F. Boggess. Carrier recombination rates in narrow-gap InAs/Ga 1x In x Sb-based superlattices. *Phys. Rev. B*, 59(8):5745–5750, 1999.

[76] B. V. Olson, E. A. Kadlec, J. K. Kim, J. F. Klem, S. D. Hawkins, E. A. Shaner, and M. E. Flatté. Intensity-and temperature-dependent carrier recombination in InAs/In(As,Sb) type-II superlattices. *Physical Review Applied*, 3(4):044010, 2015.

[77] B. V. Olson, E. A. Kadlec, J. F. Klem, S. D. Hawkins, D. Leonhardt, W. T. Coon, M. Cavaliere, E A Shaner, and Sandia National Laboratories. Minority carrier lifetime and dark current measurements in mid-wavelength. *Applied Physics Letters*, 107(18):183504, 2015.

[78] B. C. Connelly, G. D. Metcalfe, H. Shen, and M. Wraback. Direct minority carrier lifetime measurements and recombination mechanisms in long-wave infrared type II superlattices using time-resolved photoluminescence. *Citation: Appl. Phys. Lett*, 97, 2010.

[79] E. R. Youngdale, J. R. Meyer, C. A. Hoffman, F. J. Bartoli, C. H. Grein, P. M. Young, H. Ehrenreich, R. H. Miles, and D. H. Chow. Auger lifetime enhancement in InAs-Ga1-xInxSb superlattices. *Applied Physics Letters*, 64(23):3160–3162, 1994.

[80] J. R. Meyer, C. L. Felix, W. W. Bewley, I. Vurgaftman, E. H. Aifer, L. J. Olafsen, J. R. Lindle, C. A. Hoffman, M. J. Yang, B. R. Bennett, B. V. Shanabrook, H. Lee, C. H. Lin, S. S. Pei, and R. H. Miles. Auger coefficients in type-II InAs / Ga 1x In x Sb quantum wells Auger coefficients in type-II InAs / Ga 1 x In x Sb quantum wells. *Applied Physics Letters*, 2857(20):18–21, 1998.

[81] S. Krishnamurthy, M. A. Berding, Z. G. Yu, C. H. Swartz, T. H. Myers, D. D. Edwall, and R. DeWames. Model for minority carrier lifetimes in doped HgCdTe. *Journal of Electronic Materials*, 34(6):873–879, 2005.

[82] B. C. Connelly, G. D. Metcalfe, H. Shen, and M. Wraback. Direct minority carrier lifetime measurements and recombination mechanisms in long-wave infrared type II superlattices using time-resolved photoluminescence. *Citation: Appl. Phys. Lett*, 97, 2010.

[83] D. Donetsky, S. P. Svensson, L. E. Vorobjev, and G. Belenky. Carrier lifetime measurements in short-period InAs/GaSb strained-layer superlattice structures. *Appl. Phys. Lett*, 95(21):212104, 2009.

[84] S. Nigam. Carrier Lifetimes in Silicon Carbide. *IEEE TRANSACTIONS ON ELECTRON DEVICES*, 44(1):160–170, 2008.

[85] H. Demers, N. Poirier-Demers, A. R. Couture, D. Joly, M. Guilmain, N. De Jonge, and D. Drouin. Three-dimensional electron microscopy simulation with the CASINO Monte Carlo software. *Scanning*, 33(3):135–146, 2011.

[86] F. Szmulowicz, H. J. Haugan, S. Elhamri, and G. J. Brown. Calculation of vertical and horizontal mobilities in InAs / GaSb superlattices. *Physical Review B*, 84(15):1–14, 2011.

[87] H. T. Grahn. *Semiconductor Superlattices: growth and Electronic Properties*. WORLD SCIENTIFIC, apr 1995.

[88] B. V. Olson, J. F. Klem, E. A. Kadlec, J. K. Kim, M. D. Goldflam, S. D. Hawkins, A. Tauke-Pedretti, W. T. Coon, T. R. Fortune, E. A. Shaner, and M. E. Flatté. Vertical Hole Transport and Carrier Localization in InAs/InAs1xSbx Type-II Superlattice Heterojunction Bipolar Transistors. *Physical Review Applied*, 7(2):024016, 2017.

[89] G. Ariyawansa, E. H. Steenbergen, L. J. Bissell, J. M. Duran, J. E. Scheihing, and M. T. Eismann. Absorption characteristics of mid-wave infrared type-II superlattices. *Proc. of SPIE*, 9070:90701J, 2014.

[90] H. Schneider, K. Von Klitzing, and K. Ploog. Resonant Tunnelling and Miniband Conduction in GaAs/AlAs Superlattices Studied by Electrical Time-Of-Flight Techniques. *Europhysics Letters*, 8(6):575–580, 1989.

[91] H. Schneider and K. V. Klitzing. Thermionic emission and Gaussian transport of holes in a GaAs/Al " Ga, " As multiple-quantum-well structure. *Phys. Rev. B*, 38(9), 1988.

[92] R. Magri and A. Zunger. Predicting interband transition energies for InAs/GaSb superlattices using the empirical pseudopotential method. *Physical Review B*, 68(15):1–8, 2003.

[93] Y. Wei and M. Razeghi. Modeling of type-II InAs/GaSb superlattices using an empirical tight-binding method and interface engineering. *Physical Review B*, 69(8):1–7, 2004.

[94] Y. Livneh, P. C. Klipstein, O. Klin, N. Snapi, S. Grossman, A. Glozman, and E. Weiss. K.p model for the energy dispersions and absorption spectra of InAs/GaSb type-II superlattices. *Physical Review B - Condensed Matter and Materials Physics*, 86(23):1–16, 2012.

[95] L. W. Wang, S. H. Wei, T. Mattila, A. Zunger, I. Vurgaftman, and J. Meyer. Multiband coupling and electronic structure of (InAs)n/(GaSb)n superlattices. *Physical Review B*, 60(8):5590–5596, 1999.

[96] F. Szmulowicz, H. Haugan, and G. J. Brown. Effect of interfaces and the spin-orbit band on the band gaps of InAs/GaSb superlattices beyond the standard envelope-function approximation. *Physical Review B*, 69(15):155321, 2004.

[97] B. H. Hong, S. I. Rybchenko, I. E. Itskevich, S. K. Haywood, R. Intartaglia, V. Tasco, G. Rainò, and M. De Giorgi. Applicability of the k.p method to modeling of

InAs/GaSb short-period superlattices. *Physical Review B - Condensed Matter and Materials Physics*, 79(16):165323–1, 2009.

[98] M. Van Schilfgaarde, Takao Kotani, and S. Faleev. Quasiparticle self-consistent GW theory. *Physical Review Letters*, 96(22):1–4, 2006.

[99] F. Aryasetiawan and O. Gunnarsson. Reports on Progress in Physics Related content The GW method. *Rep. Prog. Phys. Rep. Prog. Phys*, 61(6198):237–312, 1998.

[100] A. W. Ashcroft and N. D. Mermin. *Solid State Physics.* Harcourt College, 1976.

[101] M C Payne, M P Teter, D C Allan, T A Arias, and J D Joannopoulos. {I}terative {M}inimization {T}echniques {F}or {A}binitio {T}otal-energy {C}alculations - {M}olecular-dynamics and {C}onjugate {G}radients. *Reviews of Modern Physics*, 64(4):1045–1097, 1992.

[102] P. Giannozzi, S. Baroni, N. Bonini, M. Calandra, R. Car, C. Cavazzoni, D. Ceresoli, G L Chiarotti, M. Cococcioni, I. Dabo, A. Dal Corso, S. Fabris, G. Fratesi, S. De Gironcoli, R. Gebauer, U. Gerstmann, C. Gougoussis, A. Kokalj, M. Lazzeri, L. Martin-Samos, N. Marzari, F. Mauri, R. Mazzarello, S. Paolini, A. Pasquarello, L. Paulatto, C. Sbraccia, S. Scandolo, G. Sclauzero, A. P. Seitsonen, A. Smogunov, P. Umari, and R. M. Wentzcovitch. QUANTUM ESPRESSO: a modular and open-source software project for quantum simulations of materials. *Journal of physics. Condensed matter*, 21(39):395502, 2009.

[103] P. Hohenberg and W. Kohn. PHYSICAL REVIEW. *Phys. Rev. B*, 136(3B), 1964.

[104] W. Kohn and L. J. Sham. Self-Consistent Equations Including Exchange and Correlation Effects. *Phys. Rev. B*, 140(4A), 1965.

[105] P. Giannozzi, S. N. Superiore, and P. Cavalieri. DENSITY FUNCTIONAL THEORY FOR ELECTRONIC STRUCTURE CALCULATIONS. Technical report, University of Udine, 2005.

[106] S. Baroni, S. de Gironcoli, a. D. Corso, and P. Giannozzi. Phonons and related properties of extended systems from density-functional perturbation theory. *Reviews of Modern Physics*, 73(2):52, 2000.

[107] L. Hedin. New Method for Calculating the One-Particle Green's Function with Application to the Electron-Gas Problem. *Physical Review*, 139(3A):A767–A823, 1965.

[108] M. S. Hybertsen and S. G. Louie. First-principles theory of quasiparticles: Calculation of band gaps in semiconductors and insulators. *Physical Review Letters*, 55(13):1418–1421, 1985.

[109] A. Marini, C. Hogan, M. Grüning, and D. Varsano. yambo: An ab initio tool for excited state calculations. *Computer Physics Communications*, 180(8):1392–1403, 2009.

[110] M. S. Hybertsen and S. G. Louise. Electron correlation in semiconductors and insulators: Band gaps and quasiparticle energies. *Phys. Rev. B*, 34(8):5390, 1986.

[111] G. Onida, L. Reining, and A. Rubio. Electronic excitations: Density-functional versus many-body Green's-function approaches. *Reviews of Modern Physics*, 74(2):601, 2002.

[112] E. Plis, B. Klein, S. Myers, N. Gautam, T. J. Rotter, R. L. Dawson, S. Krishna, S. J. Lee, and Y. H. Kim. Type-II InAs/GaSb strained layer superlattices grown on GaSb (111)B substrate. *Journal of Vacuum Science & Technology B*, 31(103):3–123, 2013.

[113] B. Klein, N. Gautam, E. Plis, T. Schuler-Sandy, T. J. Rotter, S. Krishna, B. C. Connelly, G. D. Metcalfe, P. Shen, and M. Wraback. Carrier lifetime studies in midwave infrared type-II InAs/GaSb strained layer superlattice. *Journal of Vacuum Science & Technology B: Microelectronics and Nanometer Structures*, 32(2):02C101, mar 2014.

[114] Z. B. Tian, E.a. Plis, R.T. Hinkey, and S. Krishna. Influence of composition in InAs/GaSb type-II superlattices on their optical properties. *Electronics Letters*, 50(23):1733–1734, 2014.

[115] J. Huang, W. Ma, Y. Wei, Y. Zhang, K. Cui, and J. Shao. Interface effect on structural and optical properties of type II InAs/GaSb superlattices. *Journal of Crystal Growth*, 407:37–41, 2014.

[116] B. Klein, E. Plis, M. N. Kutty, N. Gautam, A. Albrecht, S. Myers, and S. Krishna. Varshni parameters for InAs/GaSb strained layer superlattice infrared photodetectors. *J. Phys. D: Appl. Phys. J. Phys. D: Appl. Phys*, 44(44):75102–5, 2011.

[117] I. Vurgaftman, J. R. Meyer, and L. R. Ram-Mohan. Band parameters for IIIV compound semiconductors and their alloys. *Applied physics review*, 89(11):5815, 2001.

[118] B. D. Malone and M. L. Cohen. Quasiparticle semiconductor band structures including spin-orbit interactions. *Journal of physics. Condensed matter*, 25(10):105503, 2013.

[119] S. Massidda, A. Continenza, A. J. Freeman, T. M. De Pascale, F. Meloni, and M. Serra. Structural and electronic properties of narrow-band-gap semiconductors: Inp, InAs, and InSb. *Physical Review B*, 41(17):12079, 1990.

[120] J. B. Rodriguez, P. Christol, L. Cerutti, F. Chevrier, and A. Joullieentre. MBE growth and characterization of type-II InAs/GaSb superlattices for mid-infrared detection. *Journal of Crystal Growth*, 274:6–13, 2005.

[121] X. Lang and J. Xia. Interface effect on the electronic structure and optical properties of InAs/GaSb superlattices. *Journal of Physics D: Applied Physics*, 44(42):425103, 2011.

[122] T. Garwood, N. A. Modine, and S. Krishna. Electronic structure modeling of InAs / GaSb superlattices with hybrid density functional theory. *Infrared Physics & Technology*, 81:27–31, 2017.

[123] A. P. Ongstad, R. Kaspi, C. E. Moeller, M. L. Tilton, D. M. Gianardi, J. R. Chavez, and G. C. Dente. Spectral blueshift and improved luminescent properties with in-

creasing GaSb layer thickness in InAsGaSb type-II superlattices. *Journal of Applied Physics Applied Physics Letters*, 89(87):2185–151113, 2001.

[124] J. Wang and Y. Zhang. Band-gap corrected density functional theory calculations for InAs/GaSb type II superlattices. *Journal of Applied Physics*, 116(21):214301–1, 2014.

[125] W. F. Sun, M. C. Li, and L. C. Zhao. First-principles study of interface relaxation effect on interface and electronic structures of InAs/GaSb superlattices with different interface types. *Superlattices and Microstructures*, 49(1):81–90, 2011.

[126] P. Larson, M. Dvorak, and Z. Wu. Role of the plasmon-pole model in the GW approximation. *Physical Review B*, 88(12):125205, 2013.

[127] A. Rogalski, P. Martyniuk, and M. Kopytko. InAs/GaSb type-II superlattice infrared detectors: Future prospect. *Applied Physics Reviews*, 4(3):031304, 2017.

[128] Z. Taghipour, E. H. Steenbergen, S. I. Maximenko, C. P. Morath, V. M. Cowan, S. Mathews, H. Aifer, G. Balakrishnan, and S. Krishna. Vertical transport study of InAs/GaSb type-II superlattice nBp MWIR detectors using Electron-Beam-Induced Current measurement. *Proc. of SPIE, Infrared Technology and Applications XLIV*, 10624:106240N, 2018.

[129] Z. Taghipour, E. Shojaee, and S. Krishna. Many-body perturbation theory study of type-II InAs / GaSb superlattices within the GW approximation. *Journal of physics. Condensed matter*, 30:0–7, 2018.

[130] Z. Taghipour, A. Kazemi, S. Myers, P. S. Wijewarnasuriya, S. Mathews, E. Steenbergen, C. P. Morath, V. M. Cowan, G. Ariyawansa, J. Scheihing, and S. Krishna. Extraction of minority carrier diffusion length of MWIR Type-II superlattice nBp detector. *Infrared Sensors, Devices, and Applications VII*, 10404:6, 2017.

[131] A. Kazemi, S. Myers, Z. Taghipour, S. Mathews, T. Schuler-sandy, S. H. Lee, V. M. Cowan, E. Gardunod, E. H. Steenbergen, C. P. Morath, G. Ariyawansa, J. E. Schei-

hing, and S. Krishna. High Quantum Efficiency MWIR Superlattice Photodetector. *SPIE Optical Engineering+ Applications*, 10177, 2017.

[132] B. Klein, C. Hains, Z. Taghipour, E. Plis, and S. Krishna. Photocapacitance study of GaSb: In, As for defect analysis in InAs/GaSb type-II strained layer superlattices. *Infrared Physics and Technology*, 70:40–43, 2015.

[133] Z. Taghipour, E. Shojaee, and S. Krishna. Electronic Structure of Type-II InAs/GaSb Superlattices: a DFT+GW Study. *Bulletin of the American Physical Society (APS)*, 2018.